Green Chemistry

ROYAL SOCIETY OF CHEMISTRY

CRITICAL REVIEW

View Article Online
View Journal | View Issue

Cite this: *Green Chem.*, 2020, **22**, 4747

Recent advances in hydrothermal carbonisation: from tailored carbon materials and biochemicals to applications and bioenergy

Sabina A. Nicolae,*[a] Heather Au,[b] Pierpaolo Modugno,[a] Hui Luo,[b] Anthony E. Szego,[c] Mo Qiao,[b] Liang Li,[d] Wang Yin,[e] Hero J. Heeres,[e] Nicole Berge[d] and Maria-Magdalena Titirici *[a,b]

Received 20th March 2020,
Accepted 27th June 2020

DOI: 10.1039/d0gc00998a

rsc.li/greenchem

Introduced in the literature in 1913 by Bergius, who at the time was studying biomass coalification, hydrothermal carbonisation, as many other technologies based on renewables, was forgotten during the "industrial revolution". It was rediscovered back in 2005, on the one hand, to follow the trend set by Bergius of biomass to coal conversion for decentralised energy generation, and on the other hand as a novel green method to prepare advanced carbon materials and chemicals from biomass in water, at mild temperature, for energy storage and conversion and environmental protection. In this review, we will present an overview on the latest trends in hydrothermal carbonisation including biomass to bioenergy conversion, upgrading of hydrothermal carbons to fuels over heterogeneous catalysts, advanced carbon materials and their applications in batteries, electrocatalysis and heterogeneous catalysis and finally an analysis of the chemicals in the liquid phase as well as a new family of fluorescent nanomaterials formed at the interface between the liquid and solid phases, known as hydrothermal carbon nanodots.

1. Introduction

Our world is facing hard and unprecedented challenges due to the constant increase of population and technology development which implies a growing demand for energy and advanced materials that can no longer rely on fossil fuel exploitation. There is a strong need for a new productive system where clean energy generation and storage go hand in hand with sustainable materials production and studies on Hydrothermal Carbonisation (HTC) of biomass are aimed at developing a clever technology to balance them both. The term hydrothermal carbonisation describes a thermal treatment that takes place in aqueous medium heated at subcritical temperatures (180–250 °C), under self-generated pressure. HTC has been known to scientists over a century ago and it has been used as a way to mimic the natural process of coal formation,[1–5] in times when there was only little concern about the temporary shortage of fossil fuel supplies. The last two decades have seen renewed interest in this topic.[6–13] The main advantage of HTC is that, as the process takes place in water, biomass does not require a preliminary drying step, thus saving great amounts of energy and time, and furthermore allowing processing of wet mixtures, including aqueous waste and sewage sludge.[14]

Fig. 1 illustrates a schematic of the HTC process and possible products, which will also be covered in this review. In

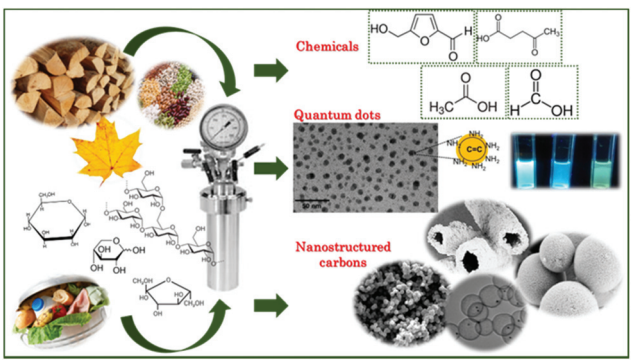

Fig. 1 Schematic representation of the HTC process with the main topics represented here.

[a]*School of Engineering and Materials Science, Queen Mary University of London, Mile End Road, London E1 4NS, UK*
[b]*Department of Chemical Engineering, Imperial College London, South Kensington Campus, London, SW7 2AZ, UK. E-mail: m.titirici@imperial.ac.uk*
[c]*Materials and Environmental Chemistry Department, Stockholm University, SE-106 91 Stockholm, Sweden*
[d]*Civil and Environmental Engineering, University of South Carolina, Columbia, SC 29201, USA*
[e]*Chemical Engineering Department, ENTEG, University of Groningen, Nijenborgh 4, 9747 AG Gronigen, Netherlands*

aqueous media, at subcritical temperatures and pressures, lignocellulosic materials undergo a vast series of transformations such as hydrolysis, dehydration, bond cleavage, formation of new bonds, and condensation. The ultimate products of these reactions can be grouped into liquid species (or water-soluble compounds), solid species (primary and secondary chars and carbon dots) and gases (water vapour, CO, CO_2, and CH_4).[15] Water-soluble compounds include furan derivatives (furfural and 5-hydroxymethylfurfural) and carboxylic acids. Many of the soluble chemicals found in the liquid phase after HTC are commercially valuable, and a few of them have been recognized as platform chemicals for a transition to a greener chemistry.[16] In some cases, the liquid phase derived from HTC treatment of biowaste feedstocks can also be used in agriculture for irrigation or recycled for a new batch of biomass conversion. Primary chars are the direct product of hydrothermal dehydration and pyrolysis of biomass. They are referred to as biochars or hydrochars to highlight their biological origin, their charred appearance (that corresponds at a physical level to a higher energy density value in terms of the higher heating value compared to that of the original biomass[17,18]) and the hydrothermal process employed to prepare them. The higher energy density value makes them fit for combustion to generate decentralised energy with lower CO_2 emissions when compared with coal power plants, since they are produced from biomass which can, in principle, be regrown to adsorb back the generated CO_2. Secondary chars are the result of further dehydration, condensation and polymerization of water dissolved compounds. The resulting particles present a spherical shape and small sizes in the domain of microns. They have long been known to form during HTC of sugars or lignocellulosic biomass. They are also often, confusingly, called humins or hydrochars. The former name has a long documented history of misuse[19] and originally referred to the alkali-insoluble fraction of humus. Throughout the times its meaning has shifted to denote the dark-brownish, amorphous products obtained by acid hydrolysis of proteins or sugars. As for the word hydrochars, we already saw that it describes hydrothermally charred biomass. Therefore, in order to avoid any further confusion, we will use the expression hydrothermal carbon (HT carbon) to denote the carbonaceous microspheres obtained *via* hydrothermal carbonization of cellulosic biomass. Their porosity can be changed using natural templates or activation procedures; their chemical and physical properties can be easily modified by their combination with different components, such as inorganic compounds, and they can be easily functionalized leading to a large number of oxygenated groups present on the surface. Carbon dots are quasi-spherical fluorescent carbon nanoparticles,[20,21] with diameters around or below 10 nm,[22] an amorphous or nanocrystalline structure with sp^2 carbon clusters[23] and a high amount of oxygen atoms and carboxylic groups on their surface.[24] Although their mechanism of formation is still not very well understood, these nanoparticles have been successfully employed as probes for the detection of metal ions[25–28] (due to the quenching effect of these species on the fluorescence of the CDs) and other chemicals,[29–31] as catalysts[29] or for imaging of cells.[32]

The first section of this review will be dedicated to the production of advanced carbon materials from biomass or biomass derivatives with focus on applications in energy storage and conversion and environmental production. Following this, we will discuss the composition of the liquid phase depending on the precursors used and the various HTC conditions as well as methods for the separation of these components from the liquid phase and their transformation in other viable chemicals using heterogeneous catalysis. Next, we will address the production of fluorescent nanometre-sized carbons. We will then focus on HTC as a viable route to convert various raw biowaste materials into hydrothermal carbons and provide a thorough characterisation of each product depending on the raw precursors and hydrothermal conditions. Finally, we will present the possibility of upgrading some of the hydrothermal carbons to fuels *via* reforming over heterogeneous catalysts. For each section we will provide an overview based on recently published papers in the literature and our own perspectives on where scientific knowledge and understanding the fundamentals are still needed for HTC to become a viable technique for both the production of advanced materials and chemicals as well as decentralised bioenergy using biowaste.

2. Advanced hydrothermal carbon materials

2.1. Fundamentals and gaps in hydrothermal carbonisation for advanced carbon production

The three main components of lignocellulosic biomass are cellulose, hemicellulose and lignin. Cellulose is a linear polysaccharide of glucose units bonded together by β-(1,4)-glucosidic bonds. Hemicellulose is a polysaccharide too, but it differs from cellulose in that it is made of a number of different sugar monomers, such as xylose, glucose, mannose and galactose. This variety of monomers makes the overall structure of hemicellulose less stronger than that of cellulose, with shorter branched chains. Lignin is a highly randomly cross-branched polymer of phenylpropane derivatives. Among the three aforementioned biopolymers, lignin is the most stable and least prone[33] to hydrolysis under hydrothermal conditions, requiring temperatures as high as 250 °C to start decomposing.[34] Therefore, polysaccharides, their monomers and their decomposition products will only be taken into account in the following description of HTC reaction pathways. However, it is important to stress that real biomass always contains lignin to some extent, and its presence is known to hinder the hydrolysis of long saccharide chains under hydrothermal conditions, lowering conversion yields of both soluble and insoluble products.[35] On the other hand, some experiments on a mixture of components including saccharides, proteins, lipids and lignin, although performed in a range of temperatures beyond those considered in this review, showed a clear syner-

gistic effect of the different components, with an increased yield of biocrude in the case of the mixture, compared to the average yield obtained by treatment of single precursors.[36] Decomposition of cellulosic materials under hydrothermal conditions can be summarized in a few basic steps: hydrolysis of cellulose and hemicellulose chains into their constituting monomers (mainly glucose and other hexose and pentose sugars); dehydration of C6 sugars to 5-hydroxymethylfurfural (5-HMF) and C5 sugars to furfural; decomposition to lower molecular weight compounds or, alternatively, condensation and aromatization reaction, to produce hydrothermal carbon.[37] A quite exhaustive scheme of the complex network of reaction pathways of decomposition of cellulose under hydrothermal conditions has recently been proposed by Buendia-Kandia *et al.*[38] (Fig. 2). The scheme was elaborated by studying the decomposition of microcrystalline cellulose under hydrothermal conditions, testing three temperatures (180 °C–220 °C–260 °C), sampling the liquid phase every 20 minutes for an overall reaction time of 120 minutes. Their results confirmed the pathway proposed by Matsumura:[39] long chains of cellulose are firstly hydrolysed to smaller oligomers or monomers of glucose. Glucose can undergo isomerization to fructose *via* the Lobry de Bruyn–Alberda–van Ekenstein transformation or epimerization to mannose.

As said before, furfural and 5-HMF derive from dehydration of pentoses (Fig. 3) and hexoses (Fig. 4), respectively. Levulinic acid (LA), also named 4-oxopentanoic acid, is derived from 5-HMF, which, under hydrothermal conditions, is rehydrated to form LA along with formic acid (Fig. 5). Glucose oligomers can undergo dehydration before complete hydrolysis, producing cellobiosan and subsequently levoglucosan. Retro-aldol condensation of glucose produces erythrose and glycolaldehyde from which lactic acid and acetic acid are derived. The presence of lactic acid (LacA) in the hydrothermal conversion of sugars was explained with a mechanism involving an initial retro-aldol condensation of fructose, yielding glyceraldehyde and dihydroxyacetone. Both of these compounds can be dehydrated to pyruvaldehyde, which in turn is converted to LacA with a benzylic acid rearrangement (Fig. 6). The benzylic acid rearrangement requires basic catalysis, and this explains why lactic acid is found in relevant amounts when basic conditions are employed for hydrothermal conversion of cellulosic biomass.[40,41] However, it was demonstrated that water under subcritical conditions could provide sufficient hydroxide ions to catalyse the reaction in the absence of any other sources of OH^-. In fact, lactic acid can also be found among the HTC products of sugars when an acid is added as a catalyst.[42]

Decarbonylation and decarboxylation reactions account for the production of CO and CO_2. Finally, due to limited access of water molecules on the inner cellulose fibres, pyrolysis of cellulose occurs, leading to the direct formation of the primary hydrothermal carbon. As for hydrothermal carbon, this material is structured as spherical microspheres[6] whose chemical structure consists of condensed furan rings linked either *via* the α-carbon or *via* sp^2- or sp^3-type carbon.[45] This suggests that 5-HMF and furfural are the main building blocks of hydrothermal carbon. 5-HMF is a rather unstable and reactive molecule under hydrothermal conditions. A closer look at its chemical structure is useful in understanding its reactivity and thus to propose hypotheses about its role in the formation of HTC spheres. 5-HMF possesses one aldehyde group and one hydroxymethyl group at positions 2 and 5, respectively, on the furan ring.

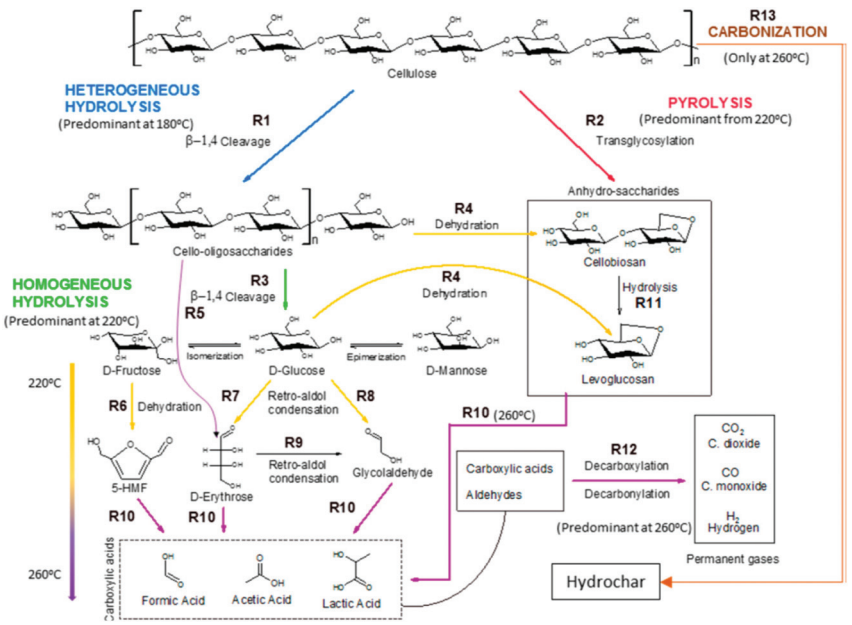

Fig. 2 Scheme of the reaction pathways of cellulose decomposition as proposed by Buendia-Kandia *et al.*; reproduced with permission from ref. 38.

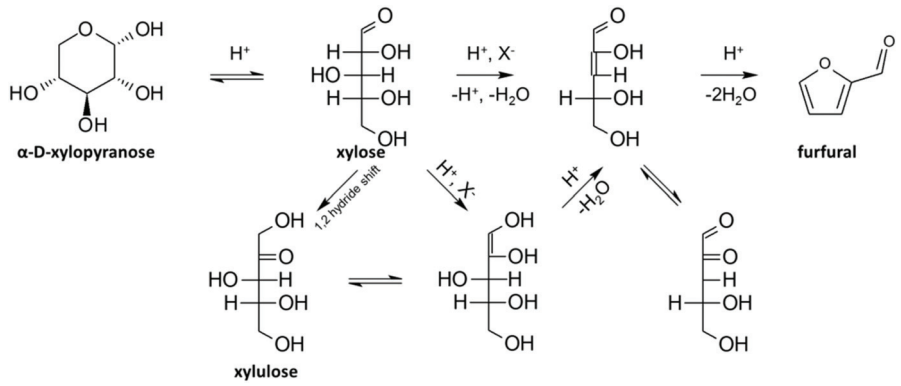

Fig. 3 Mechanism of dehydration of xylose to furfural *via* an acyclic pathway; adapted from ref. 43.

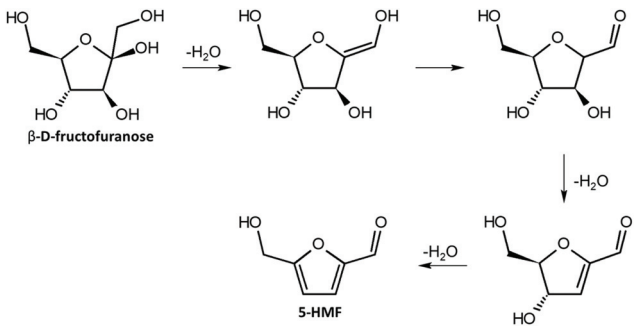

Fig. 4 Mechanism of dehydration of fructose to 5-HMF; adapted from ref. 44.

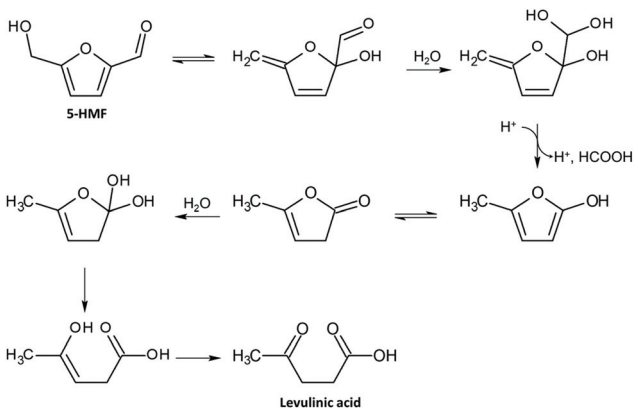

Fig. 5 Mechanism of rehydration of 5-HMF to levulinic acid with loss of a carbon atom in the form of formic acid; adapted from ref. 46.

The aldehyde group can undergo aldol condensation with α-ketones or aldehydes (Fig. 7) or react with alcohols or diols to give (hemi)acetals. The acetalisation of the aldehyde group activates the furan ring towards electrophilic aromatic substitution. The hydroxymethyl group, on the other hand, can be subject to nucleophilic substitution, as the mildly acidic conditions can protonate the hydroxyl group making it a better leaving group. Finally, the whole furan ring, due to its lower aromaticity when compared to benzene, can behave as a diene, undergoing nucleophilic addition, ring-opening reaction or Diels–Alder cycloaddition.

A recent investigation by van Zandvoort *et al.*[48] has provided very important insights into the chemical structure of hydrothermal carbon. In fact, by means of 1D and 2D solid-state Nuclear Magnetic Resonance (NMR) spectra of ^{13}C-labeled hydrothermal carbon, various different linkages have been identified in the 2D NMR spectra, ranging from the most abundant C_α–$C_{aliphatic}$ and C_α–C_α linkages to minor ones such as C_β–C_β and C_β–$C_{aliphatic}$ cross-links. Furan rings have been found to be linked by short aliphatic chains; levulinic acid is also included in the structure through covalent bonds. A chemical structure (Fig. 8) was proposed.[48]

Brown *et al.*[49] have simulated Raman spectra of model constituents of hydrothermal carbon by means of Density Functional Theory (DFT). By fitting the experimental Raman hydrothermal carbon spectrum with a 12-peak fit, they have found that two model structures could reproduce the main features of the hydrothermal carbon: its Raman spectrum and its elemental analysis: (1) a structure consisting of arene domains comprising 6–8 rings connected *via* aliphatic chains; and (2) a furan/arene structure consisting primarily of single furans and 2 or 3 ring arenes. However, subsequent NMR and infrared (IR) analyses suggested that the latter model is more consistent with the experimental observations. A nucleation pathway was proposed by Sevilla and Fuertes[50] which derived observations from the dissolution behaviour of cellulose under hydrothermal conditions, hence known as "the soluble pathway". This pathway includes: (i) hydrolysis of cellulose chains, (ii) dehydration and fragmentation into soluble products of the monomers that come from the hydrolysis of cellulose, (iii) polymerization or condensation of the soluble products, (iv) aromatization of the polymers thus formed, (v) appearance of a short burst of nucleation and (vi) growth of the nuclei so formed by diffusion and linkage of species from the solution to the surface of the nuclei.[50] More recently, Tsilomelekis *et al.*[51] have studied acid catalysed degradation of 5-HMF by means of ATR-FTIR spectroscopy, Scanning Electron Microscopy (SEM) and Dynamic Light Scattering (DLS) to

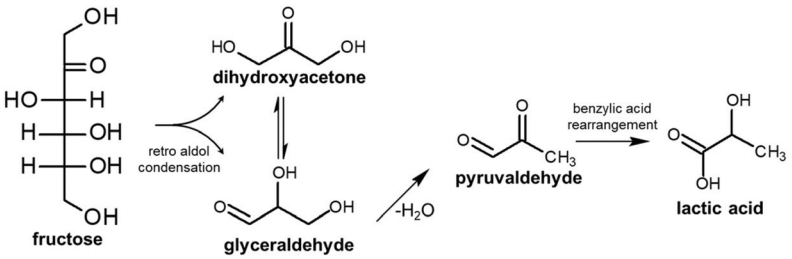

Fig. 6 Mechanism of formation of lactic acid through retro aldol condensation and a benzylic rearrangement; adapted from ref. 42.

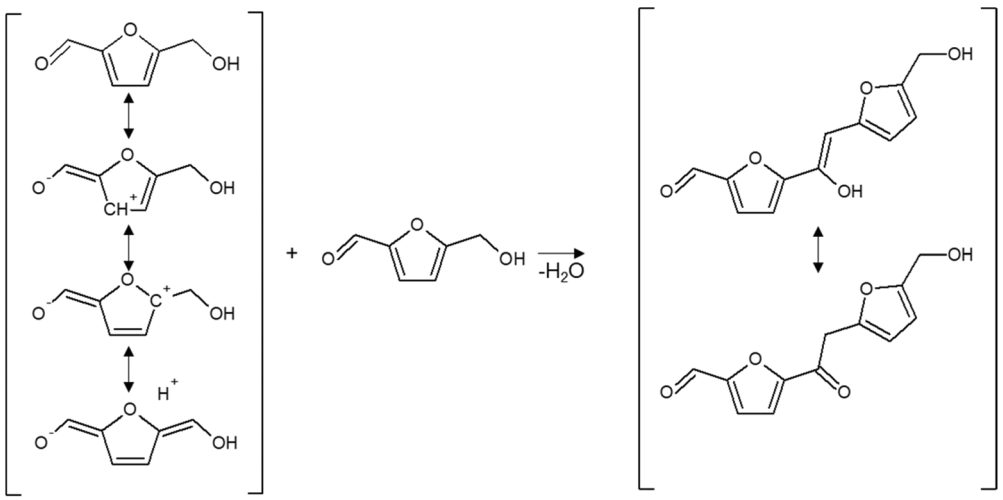

Fig. 7 Tautomeric forms of HMF and the reaction to a dimer *via* aldol condensation; adapted from ref. 47.

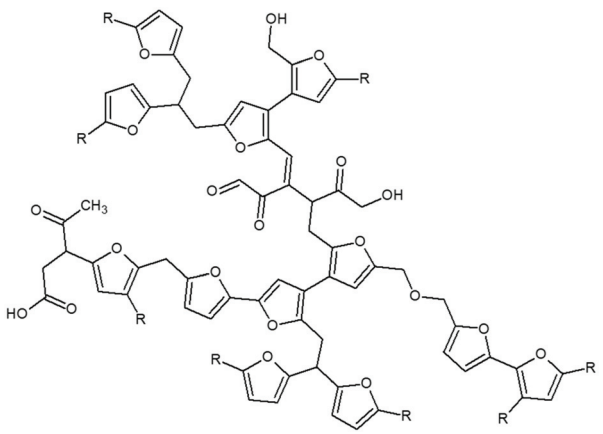

Fig. 8 Chemical structure of hydrothermal carbon proposed by van Zandvoort; adapted from ref. 48.

understand the growth mechanism of 5-HMF derived hydrothermal carbon. They have proposed a mechanism based on an initial nucleophilic attack of a 5-HMF carbonyl group to the α- or β-position of the furanic ring, along with aldolic condensation and etherification. Small, soluble oligomers grow heavier until they form small solid nuclei through phase separation. Small particle aggregation and continuous 5-HMF addition lead to the formation of bigger hydrothermal carbon particles. However, Cheng *et al.*[53] have noted that hydrothermal carbon can be partially dissolved by multistage dissolution in an organic solvent to oligomers that have mass numbers ranging from 200 to 600 Da, as detected by liquid chromatography coupled with mass spectrometry (LC-MS). Although this observation has led the authors to speculate that hydrothermal carbon is actually an aggregate of oligomeric species rather than a disordered polymer,[53] there might be a different interpretation. In fact, a very recent paper by Higgins *et al.* reported striking evidence of a core/shell structure in glucose-derived hydrothermal carbon. This evidence, obtained by combined STXM and NEXAFS observations, points to a "harder", more condensed and hydrophobic core, surrounded by a "softer" shell, rich in aldehydic/carboxylic groups. These reactive functionalities serve as binding sites for the growth of the carbon particles.[54] Formic acid and levulinic acid play a key role in this scenario: the former, due to its rather high pK_a, significantly increases the rate of conversion of C6 sugar to 5-HMF in an autocatalytic fashion, therefore speeding up the growth of spherical particles. Levulinic acid, on the other hand, has a lower pK_a and therefore does not have a strong catalytic effect, but it does affect the growth of the spherical particles taking part in the process as building units and slowing the growth by reducing the surface density.[52]

Moreover, Jung *et al.* have stated that significant growth of carbon particles occurs when the 5-HMF concentration has already dramatically declined. This points to an alternative model for growth of particles based on coalescence, which is also supported by the further observation that addition of electrolytes in the reaction medium increases particle sizes by reducing repulsive forces between particles.[47] This debate is a proof that a thorough comprehension of the mechanisms underlying HTC has not been achieved yet and there is considerable space for further research.

2.1.1. Influence of feedstock, reaction time and temperature on the material morphology

2.1.1.1. Feedstock. As highlighted in the previous section, furfural and 5-HMF, originating from the dehydration of pentoses and hexoses, respectively, play a key role in the formation of hydrothermal carbon spheres, due to their reactivity. Consequently, it is reasonable to expect chars with a similar morphology and structure, regardless of the carbon precursor, as long as any of the aforementioned compounds are present in the reaction medium. Titirici *et al.*[55] have demonstrated that all hexose (and 5-HMF)-derived carbon spheres have the same morphology. Similarly, carbon spheres obtained from the HTC of xylose and furfural are indistinguishable in shape. Further confirmations come from Falco *et al.*,[8] who have compared the morphology of the HTC secondary char derived from glucose, cellulose and rye straw. While glucose and cellulose-derived carbon spheres appear similar in shape, it is argued that long cellulose fibers are disrupted under hydrothermal conditions, leading to the formation of shorter chains that adopt a spherical shape to minimize contact with water. Rye straw behaviour is similar to that of cellulose, with microspheres appearing on the surfaces of the fibers that suffer only minor disruption.

2.1.1.2. Reaction time and temperature. Reaction time and temperature have been shown to influence the hydrothermal carbon morphology. Sevilla *et al.*,[13] studying hydrothermal carbon yields from the HTC of glucose, sucrose and starch, noted that in any case, a rise of the precursor concentration, reaction time or reaction temperature resulted in an increased yield of hydrothermal carbon and in the diameter of the microspheres. Romero-Anaya[56] have substantially confirmed the observation, noting also that carbon sphere growth reaches a maximum (at fixed reaction time and precursor concentration) at 200 °C. Temperature has a big impact on hydrothermal decomposition of cellulose. Depolymerization of microcrystalline cellulose in water-soluble compounds is known to start at 180 °C.[57] However, it has been shown that depolymerisation of cellulose to sugar oligomers becomes predominant at 220 °C, while temperatures as high as 260 °C cause a decline of sugar oligomers in favour of decomposition products such as 5-HMF or carboxylic acids.[38] Reaction time seems to have an impact on the morphology and size of carbon spheres only up to a certain point. In fact, it has been noted that, over treatment times of 12, 24 and 48 h, sugar derived carbon spheres achieve bigger and more uniform sizes from 12 h to 24 h, but longer reaction times do not produce any change in the size or morphology.[56] Moreover, it has been demonstrated that a second subsequent HTC of the carbon spheres results in the uniform growth of the pre-existing particles without any relevant formation of new ones.[58] Simsir *et al.*[59] have studied the effects of different reaction times on HTC of different kinds of feedstocks (glucose, cellulose, chitin, chitosan, and wood chips) at a fixed temperature of 200 °C. In this study, glucose-derived carbon spheres are not observed before a 12 hour long treatment, with an average diameter of around 800 nm for a residence time between 12 h and 36 h, and a slightly lower average diameter of 500–600 nm with the increase in residence time to 48 h. This has been explained with the plausible existence of an equilibrium between the growth and decomposition of spherical carbon particles for longer residence times. Chitin is insensitive to HTC, while cellulose and wood chips produce hard carbon spheres, too. Finally, chitosan derived hydrothermal carbon appears in the form of densely aggregated structures.

2.1.2. Influence of feedstock, reaction time and temperature on hydrothermal carbon yields and chemical characteristics. Process conditions (*e.g.*, reaction time and reaction temperature) and feedstock properties have been shown to influence hydrothermal carbon yields and chemical composition.[60–63] Reaction temperature has been reported to be quite influential on these gross hydrothermal carbon properties. The influence of reaction time, however, varies and appears to be somewhat dependent on carbonisation kinetics. The combined influence of reaction time and temperature is often modelled by using a severity factor approach,[37,64,65] which provides a means for comparing results from experiments conducted at different times and temperatures.[65,66] Severity factor (f) is defined as:[37]

$$f = 50t^{0.2} \times e^{(-3500/T)}$$

where t is time (s), and T is the final reaction temperature (K). Increases in reaction severity correlate with an increase of reaction temperature and/or reaction time and provide a relative measure of reaction severity among carbonisation studies facilitating the comparison of multiple studies. To understand how hydrothermal carbon yields and chemical compositions differ for different feedstocks, the yields and chemical characteristics of hydrochars reported in the literature following the carbonisation of different organic feedstocks were collected and compared. Results from this comparison are presented in Fig. 9–12. These box plots illustrate the distribution of the collected data, as well as median and average values. These collected data represent the carbonisation of a variety of feedstocks over a large range of process conditions. To facilitate comparison between these studies, severity factors associated with each set of experimental data collected were calculated. In each figure, the feedstocks are listed in order of the lowest average severity factor to the greatest average severity factor and a plot of the average severity factors is included above each box plot.

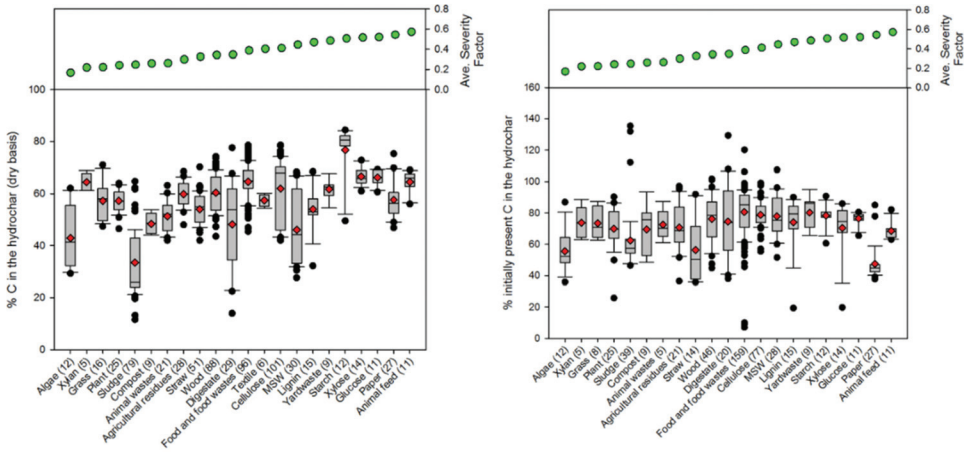

Fig. 9 Distributions associated with the hydrothermal carbon yields of different feedstocks based on literature-collected data. The line in each box represents the median value. The ends of each box represent the 25th and 75th percentiles associated with the data. The red diamonds represent the average values. The lines and data points represent the scatter of data beyond the 10^{th} and 90^{th} percentiles. The numbers in parentheses following each feedstock category represent the number of data points represented on the plot.

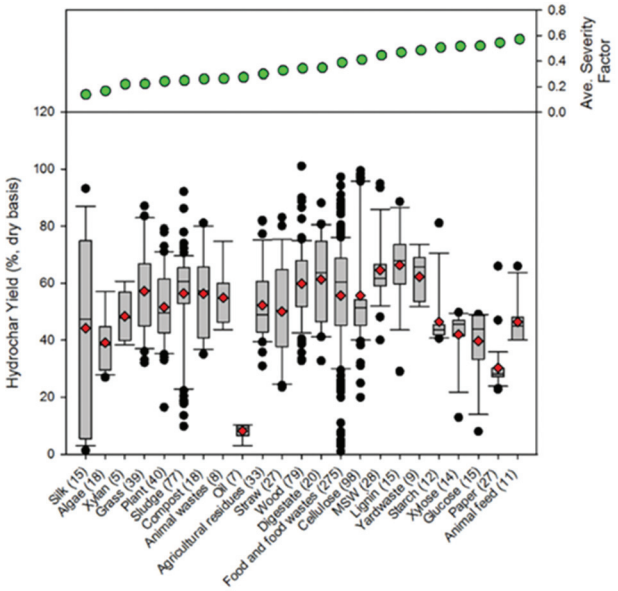

Fig. 10 Distributions associated with the (left) percentage of carbon in the hydrothermal carbon and (right) the percentage of initially present carbon that remains in the hydrothermal carbon following carbonisation. The line in each box represents the median value. The ends of each box represent the 25th and 75th percentiles associated with the data. The red diamonds represent the average values. The lines and data points represent the scatter of data beyond the 10th and 90th percentiles. The numbers in parentheses following each feedstock category represent the number of data points represented on the plot.

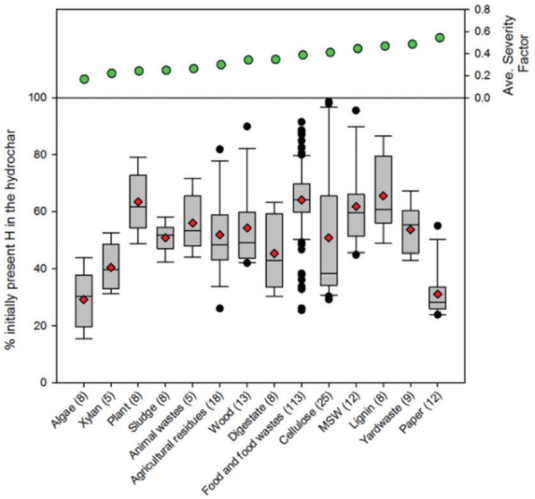

Fig. 11 Distributions associated with the percentage of hydrogen in the hydrothermal carbon. The line in each box represents the median value. The ends of each box represent the 25th and 75th percentiles associated with the data. The red diamonds represent the average values. The lines and data points represent the scatter of data beyond the 10th and 90th percentiles. The numbers in parentheses following each feedstock category represent the number of data points represented on the plot.

Fig. 9 presents a comparison of hydrothermal carbon yields associated with literature-collected data. Results from this analysis indicate that the average and median yields obtained when carbonizing the majority of feedstocks range from 40 to 60%. The carbonisation of lignin results in the greatest average and median yields (average: 66% and median: 68%). This observation is not surprising, as lignin has been shown to be only mildly influenced when exposed to HTC.[8,35] The carbonisation of municipal solid waste (MSW), digestate, wood, and yard waste also results in average and median yields greater than 60%. Carbonisation of oils (*e.g.*, bio-oil and pyrolysis oil)[67,68] results in significantly lower hydrothermal carbon yields. Similarly, the HTC of paper and algae also results in relatively lower yields than those associated with the majority of other feedstocks. In general, as the reaction severity increases, compound volatilisation and solubilisation increase, resulting in decreased solid yields.[8,69–71] This general trend is

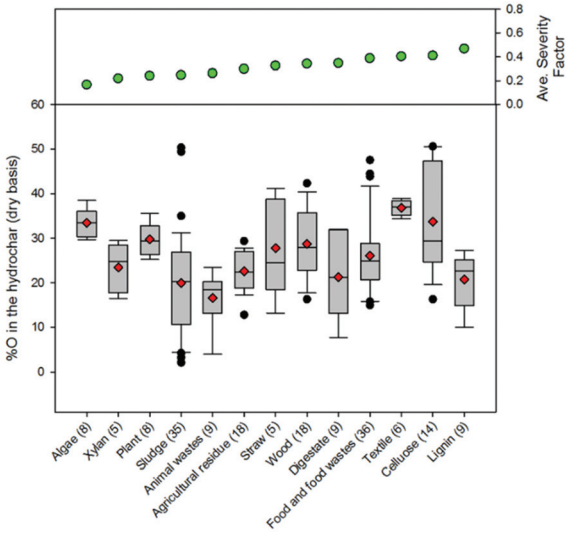

Fig. 12 Distributions associated with the percentage of oxygen in the hydrothermal carbon. The line in each box represents the median value. The ends of each box represent the 25th and 75th percentiles associated with the data. The red diamonds represent the average values. The lines and data points represent the scatter of data beyond the 10th and 90th percentiles. The numbers in parentheses following each feedstock category represent the number of data points presented on the plot.

observed for individual feedstocks. However, when collectively investigating trends of all feedstocks, no trend with an increasing severity factor (from left to right on the figure) is observed, suggesting that the feedstock properties significantly influence hydrothermal carbon yields (more than the reaction conditions), consistent with that which has been previously reported.[72–75] Lu and Berge[72] reported that changes in feedstock properties/complexity influence hydrothermal carbon yield.

Fig. 9–12 illustrate how changes in feedstock and process conditions influence the chemical properties of hydrothermal carbon. Based on the compiled data, the majority of the carbon content of the hydrothermal carbon generated from the carbonisation of different organics generally ranges from 40 to 65%, with the hydrothermal carbon generated from starch, xylose, and glucose containing the largest average hydrochar carbon content (Fig. 10 left). Generally, as the reaction severity increases, the carbon content of the hydrothermal carbon increases.[8,71,76,77] However, trends in the average hydrothermal carbon content are not observed with increasing severity factor (from left to right on the figure), suggesting that, like that associated with hydrothermal carbon yield, feedstock properties significantly influence the hydrothermal carbon content. Fig. 10 right provides a summary of the fraction of initially present carbon that remains integrated within the hydrothermal carbon following carbonisation. The greatest, on average, loss of carbon from the feedstock to the gas and/or liquid-phases occurs when carbonising paper, straw, and algae. The greatest retention of initially present carbon in the hydrothermal carbon occurs when carbonising food and yard waste (Fig. 10 right), two biomass materials that are ideal candidates for conversion *via* HTC because of their high initial moisture contents.

The majority of the generated hydrothermal carbon, regardless of feedstock, contains hydrogen concentrations ranging from approximately 4 to 6% (Fig. 11). An exception to this is the hydrothermal carbon generated when carbonising food waste, which contains an average hydrogen percentage of 7.2%. The feedstocks that result in the greatest average loss of hydrogen to either the gas or liquid-phase are algae and paper, while greater than 60% of the initially present hydrogen remains in the hydrothermal carbon when carbonising food waste, lignin, MSW, and plant materials. At relatively low and high severity factors, slight trends exist, suggesting that at these reaction severities, process conditions are potentially more influential than feedstock properties on the fraction of initially present hydrogen that remains within the hydrothermal carbon. Not surprisingly, a small amount of the oxygen present in the initial feedstocks remains integrated within the hydrothermal carbon following carbonisation (Fig. 12), which is beneficial when considering the use of hydrothermal carbon in different applications, such as an energy source. This observation is consistent with that reported in the literature; the decrease in the solid-phase oxygen content has been reported as being the most influential factor contributing to the decrease in solid recoveries.[76] Food waste, lignin, and plant materials, on average, retain the largest fraction of oxygen embedded within the initial feedstocks, when compared to other carbonised feedstocks. Generally, as the reaction severity increases, the hydrothermal carbon oxygen content decreases.[76,78,79] Interestingly, trends in the average hydrothermal carbon oxygen content are not observed with increasing severity factors (from left to right on the figure), suggesting that feedstock properties also influence the hydrothermal carbon oxygen content.

2.2. Synthesis of porous carbon materials

Hydrothermal carbon materials have been of great interest, over the years, due to their wide range of applications. Used in many ways, such as for cleaning the dyes present in water and sugar, or for the removal of unpleasant odours,[80] present-day applications mention them in industry as adsorbents for gas purification[81–83] and water treatment[84,85] or a catalyst and catalyst-supports.[86,87] They are, also, often used in the fields of energy storage, fuel cells and chromatography technologies.[88,89] In order to improve their features, a great number of studies are focused on developing new synthetic approaches for creating porous structures and enhancing the surface area, along with gaining a fundamental understanding of their properties.[90,91] As mentioned before, the pristine hydrothermal carbons are nonporous and sometimes not applicable for further usage.[92–95] To overcome this, different strategies, including templating methods (soft and hard templating),[93,94,96] or chemical activation, using alkaline compounds, KOH,[95,97] NaOH,[85] and $ZnCl_2$[98] or acids, such as H_3PO_4,[99] in combination with HTC, have been proposed.

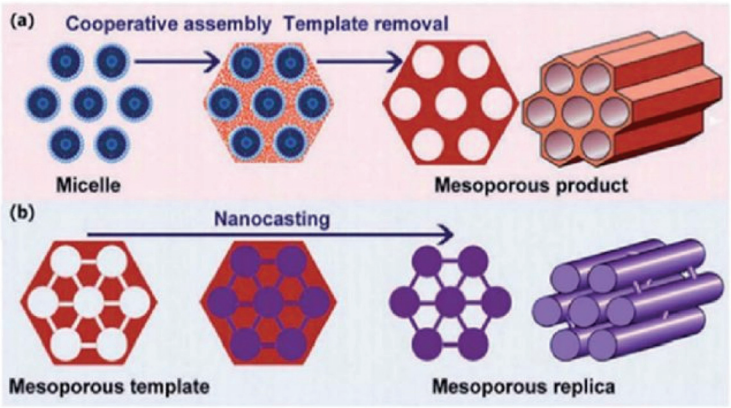

Fig. 13 Graphical representation of the templating methods: a – soft templating and b – hard templating; reproduced with permission from ref. 104.

2.2.1. Templating methods. One of the first attempts at using templating methods for the development of porous carbon materials has been made by Gilbert *et al.*[100] in 1982. They synthesised porous glassy carbons by impregnating a silica template with a phenol-formaldehyde resin mixture. This methodology reflects the "hard (*exo*) templating" approach and is based on a mixture of a carbon precursor (usually phenolic resins) with a hard template. In this way, the carbon precursor will infiltrate into the structure of the template and it will be carbonized within the pores (at high temperatures, >700 °C). The template is ultimately removed, leaving behind a well-defined structure (see Fig. 13b).[101,102] Later on, Liang *et al.*[103] developed a new strategy based on the self-assembly properties of block copolymers and aromatic resins, such as phloroglucinol, or resorcinol/formaldehyde. This method known as "soft (*endo*) templating" is a classical way to produce inorganic porous materials (see Fig. 13a). As HTC is a versatile process, it can be easily combined with the above-mentioned methods, in order to synthesise porous carbons derived from sustainable resources.

2.2.1.1. Soft templating in HTC. Nanostructured HTC–derived materials can be synthesised using polymeric templates of defined size and shape. In soft-templating, an amphiphilic molecule such as a surfactant or block-copolymer self-assembles with a carbon precursor into an organized mesophase, which is stabilised by thermal treatment. The process is controlled by several parameters, such as the concentration, temperature, hydrophilic or hydrophobic reaction, pH, *etc*. Generally, the templates are polymers such as poly(ethylene oxide)-*b*-poly(propylene oxide)-*b*-poly(ethylene oxide)triblock-coplymers (PEO-*b*-PPO-*b*-PEO) from the Pluronic family,[96,105,106] polystyrene-*b*-poly(ethylene oxide) (PS-*b*-PEO)[107] or polystyrene-*b*-poly(4-vinlpiridine)(PS-*b*-P4VP),[108] trioctylamine@ferrocene.[93] Usually, the carbon precursors consist of small clusters of phenol-formaldehyde, "resol" or phloroglucinol-formaldehyde resins, but many researchers adopted it by using different carbon precursors, including carbohydrates,[90,94] nitrogen and carbon-rich compounds,[94,96] organic acids,[93] and natural polymers (lignin, chitin, and cellulose).[109,110] For example, Liang *et al.*[111] synthesised porous carbon spheres *via* soft templating assisted HTC, using Pluronic F108 as a template and phenol-formaldehyde as a precursor. The mixture was subjected to HTC at 170 °C for 6 h, followed by carbonisation at 600 °C under a N_2 atmosphere. Further characterization revealed the formation of spherical carbon particles with a microporous structure. As a result of the high number of micropores, the carbon spheres possessed high specific surface area and high pore volume, with values of about 1481 $m^2\ g^{-1}$ and 0.9 $cm^3\ g^{-1}$ respectively. Pluronic F127, in combination with xylose, has been reported by Liu *et al.*[112] for the production of carbonaceous long-range ordered mesostructures. The same approach has been used by Xie *et al.*[113] for the synthesis of hierarchically porous materials with tunable properties. In both cases, the obtained materials have been characterized as a mesoporous structure with a surface area of around 450 $m^2\ g^{-1}$. Zhou *et al.*[105] reported the synthesis of core-mesoporous shelled carbon spheres *via* HTC and soft templating. Starting from 2,4-dihydroxybenzoic acid, hexamethylenetetramine and Pluronic P123, they produced uniform carbon spheres with an average diameter of ~141 nm and shell thicknesses of ~30 nm (see Fig. 14a and b). Characterisation techniques revealed the porous structure with a surface area of up to 648 $m^2\ g^{-1}$ and a large pore volume (1.06 $cm^3\ g^{-1}$). In a similar way, Xiao *et al.*[96] reported the synthesis of porous carbon materials starting from glucosamine. During the study, they investigated the influence of pH and the amount of template. By moving from neutral to acidic conditions, the specific surface area significantly increased, from 550 $m^2\ g^{-1}$ up to 980 $m^2\ g^{-1}$, as a result of P123 micelle formation being favoured at pH 2. Also, an improvement in textural properties was observed on increasing the amount of polymer. SEM micrographs show the formation of agglomerated small particles, confirming the transformation of glucosamine in carbon spheres (Fig. 14c), and TEM reveals the worm-like structure of the sample, related to the formation of micro- or mesopores (Fig. 14d). P123 together with sodium

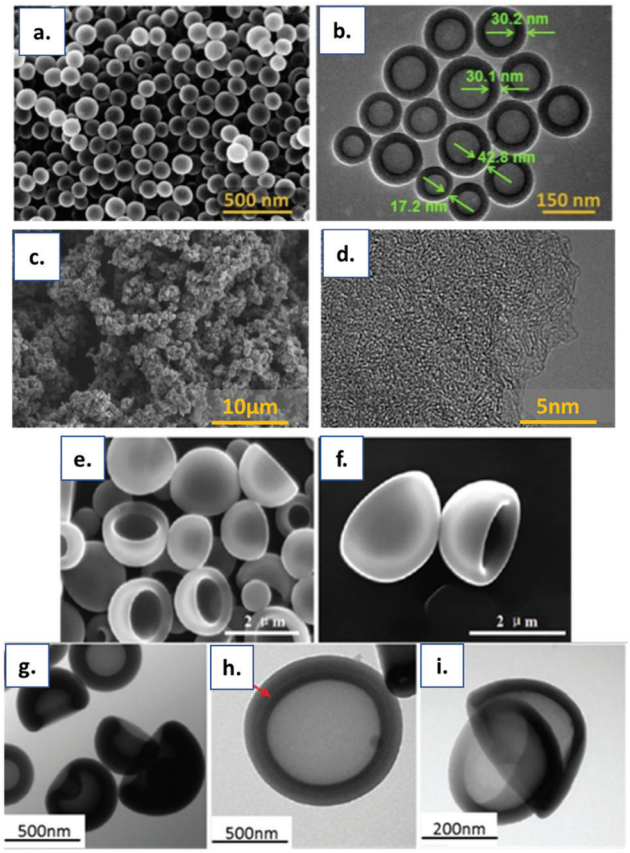

Fig. 14 Typical (a) SEM and (b) TEM images of hollow core-mesoporous shelled carbon spheres; reproduced with permission from ref. 105. (c) SEM and (d) TEM images of hydrothermal porous carbons (reproduced with permission from ref. 96). (e) and (f) SEM images with different magnifications of BHCS. (g–i) TEM images of BHCS under different magnifications (reproduced with permission from ref. 93).

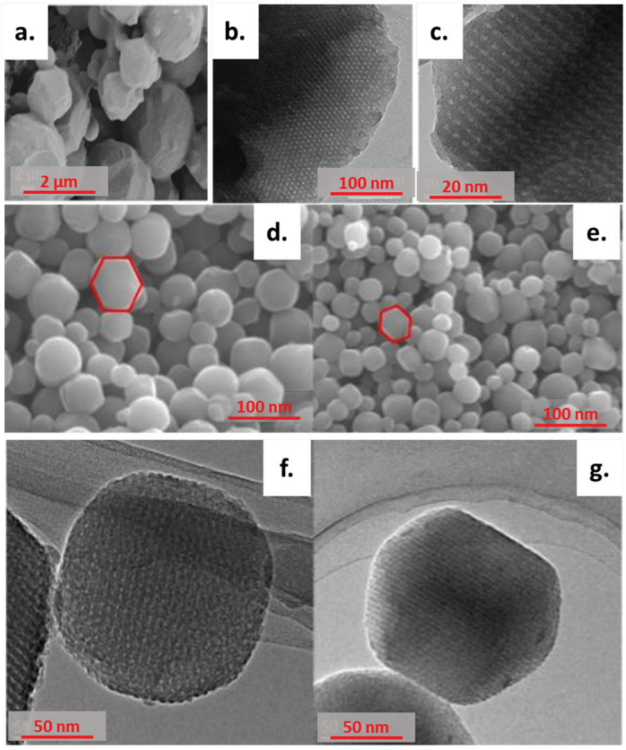

Fig. 15 (a) SEM, (b) TEM, and (c) HRTEM micrographs of ordered mesoporous carbons derived from fructose (reproduced with permission from ref. 90). (d and e) SEM images of ordered mesoporous carbons and (f and g) TEM images of the same samples with an *Im3m* mesoporous structure; reproduced with permission from ref. 115.

oleate (SO) have been reported by Chen *et al.*[114] in the synthesis of asymmetric flask-like hollow carbon materials. Zhang *et al.*[93] reported the synthesis of hollow carbon spheres starting from ascorbic acid and trioctylamine @ferrocene-in-water. The authors obtained bowl-like hollow carbon spheres (BHCS – see Fig. 14e–i) with a microporous structure, a diameter of approximately 0.53 nm and a specific surface area of about 200 $m^2 g^{-1}$.

The synthesis of ordered porous carbon materials derived from D-fructose has been reported by Kubo *et al.*[90] In this way, the HTC of D-fructose was performed at 130 °C for a long time, in order to ensure the stability of the template. The final composite was characterised by ordered porosity with pore diameters being around 10 nm and wall thicknesses of 6 nm, indicating that the self-assembly of the polymer with fructose was successful (Fig. 15a–c). The material was characterised by a 257 $m^2 g^{-1}$ surface area and a 0.14 $cm^3 g^{-1}$ pore volume. Chen *et al.*[115] synthesised carbon nanospheres starting from a urea-phenol-formaldehyde (UPF) resin and Pluronic F127. The resulting materials had a well-ordered cubic *Im3m* mesostructure in large domains with spherical shapes with a mean diameter of 240 nm and high surface area, in the range of 446–566 $m^2 g^{-1}$. SEM and TEM results are illustrated in Fig. 15d–g.

2.2.1.2. Hard templating in HTC. The hard-templating method is based on the structure replication approach using sacrificial templates. The advantage of hard templating combined with HTC is that polar functionalities are directly present on the surface of the synthesised material. Different templates can and have been employed, such as silica,[116] zeolite,[117,118] and metal organic frameworks.[119] An advantage of hard templating over soft templating is a better control of the carbon structure, and a higher possibility of obtaining hierarchical structures.[120] Xiao *et al.*[94] reported the synthesis of mesoporous carbon materials by combining soft and hard templating strategies. In this way, they used different saccharides (D-glucose_1, D-fructose_2, D-glucosamine hydrochloride_3, D-maltose_4, sucrose_5, and β-cyclodextrin_6), triblock copolymers and tetraethyl orthosilicate (TEOS). During HTC, Pluronic P123 forms micelles that are covered by a silica layer, coming from the hydrolysis of TEOS and the subsequent condensation reaction of orthosilicic acid. The silica interacts with the micelles *via* hydrogen bonds and acts as a protector for the micelles during the HTC. The carbon precursor reacts on the silica surface, and forms hydrothermal carbon, without harming the micelles. In this way, after the template removal,

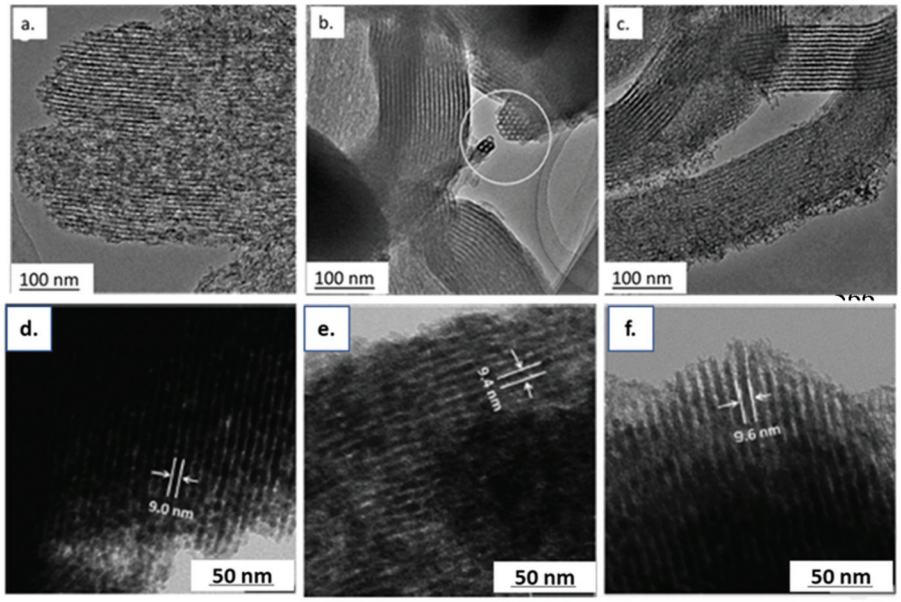

Fig. 16 TEM images of (a) OHTC_1, (b) OHTSiC_1 (before etching the silica template) and (c) OHTSi_1 (after burning the carbon at 600 °C), reproduced with permission from ref. 94; TEM pictures of (d) SBA-15/C composites after calcination at 900 °C, (e) pristine carbon materials after template removal and (f) S-doped carbon materials after template removal (reproduced with permission from ref. 121).

the carbon presents an ordered structure. The obtained materials were denoted as OHTC-X (where X refers to the carbon source) and were characterised by type IV isotherms, specific for mesoporous structures, with a H2 hysteresis loop, indicating a multilayer adsorption of nitrogen. The surface areas (pore volume) are in between 300 $m^2\ g^{-1}$ (0.55 $cm^3\ g^{-1}$) and 520 $m^2\ g^{-1}$ (0.40 $cm^3\ g^{-1}$). TEM images illustrate the ordered structure of the materials (Fig. 16). To assess the ordered character of the pores the authors viewed the samples with and without a silica template (Fig. 16a and b). It was observed that the carbonaceous powders preserve the ordered orientation after template removal. To confirm that the silica formed *in situ* during the HTC is the structure directing agent, the carbon was burned by calcination, leaving behind ordered silica (Fig. 16c). Hard templated carbons have been prepared by Wang *et al.*[121] using SBA-15 as a sacrificial template for the synthesis of ordered mesoporous doped carbons. Starting from glucose and using HTC, the mixtures are connected through carbon bridges and cover the template uniformly. The final material is highly populated with oxygenated groups, coming from the dehydration compounds of glucose during the HTC. Part of these are removed during further carbonisation, at 900 °C, and the template is removed by NH_4HF_2 leaching. TEM pictures of the obtained materials show the presence of a well-ordered structure of the composites C/SBA-15 (Fig. 16d) which is stable also after the template removal (Fig. 16e and f). The porosity was confirmed also by N_2 sorption isotherms, both doped and undoped carbons showing type IV isotherms characteristic of mesoporous materials with pores ranging from 2 to 8 nm and surface areas of 253 $m^2\ g^{-1}$ and 341 $m^2\ g^{-1}$, respectively.

2.2.2. Activation methods. Aside from the templating methods, activation strategies have been highly implemented in the generation of porosity in the carbon structure.[97,99,122–124] Generally, there are two types of activations that could be applied on hydrothermal carbons: physical and chemical. In the case of physical activation, the hydrothermal carbon is treated at temperatures in the range of 600–900 °C, under an inert atmosphere (carbonisation) or in an oxygen or steam flow (activation/oxidation). For the chemical activation, the hydrothermal carbon is mixed with an acid, a strong base or a salt before carbonisation.[122] The most common chemical activators are KOH,[97,125] NaOH,[85] $Li_2C_2O_4$, $Na_2C_2O_4$, $K_2C_2O_4$,[126] $ZnCl_2$ [98] and H_3PO_4.[99] Zhu *et al.*[126] synthesised porous carbon materials *via* the HTC of pineapple waste and chemical activation. In this way, the biomass was washed, pulverized, and sieved, followed by mixing with alkali metal oxalate ($Li_2C_2O_4$, $Na_2C_2O_4$ and $K_2C_2O_4$) in a mass ratio of 1 : 2 (biomass : alkali metal) and HTC for 10 h at 210 °C. Porosity measurements revealed the formation of nonporous and macroporous structures for the $Li_2C_2O_4$ and $Na_2C_2O_4$ activated carbons (ACs) and microporous structures for the ACs derived from the activation with $K_2C_2O_4$. When comparing the porosity data such as the pore volume (V_0) and narrow micropore volume (V_n), V_n is bigger for the $K_2C_2O_4$ ACs, and the $Li_2C_2O_4$ and $Na_2C_2O_4$ ACs present opposite results. The authors explained these textural differences among the AC series with $Li_2C_2O_4$, $Na_2C_2O_4$ and $K_2C_2O_4$ by the different reaction pathways of the oxalates during the activation process. In this way, when $K_2C_2O_4$ at high temperature is used, a larger amount of CO is released in the third stage, which causes the micropore formation. Sevilla *et al.*[127] reported the synthesis of

microporous carbon *via* the HTC of microalga and glucose mixtures. To ensure the microporosity, the hydrothermal carbon was chemically activated using KOH at elevated temperatures, 650–750 °C, in a mass ratio of 2 KOH/hydrothermal carbon. The obtained materials were characterised by their microporous structure with an apparent surface area of 1800 $m^2 g^{-1}$ to 2200 $m^2 g^{-1}$ at the maximum activation temperature (750 °C). Li *et al.*[128] synthesised a composite structure of a graphene-like nanosheet (GN)/porous carbon framework using waste-peanut skin as a biomass precursor. The procedure was based on a H_2SO_4 assisted HTC followed by KOH activation, and during the study the concentration of H_2SO_4 was varied. TEM and SEM results showed that the graphitisation level was very much influenced by the acid concentration. In this way, the sample without H_2SO_4 presented a typical amorphous carbon structure while the one with the highest H_2SO_4 concentration possessed three-layer structures with a clear interlayer spacing of 0.38 nm, indicating the graphene-like morphology. The samples were characterized by a micro–mesoporous structure, with a high number of micropores. Shi *et al.*[129] prepared ACs starting from glucose and glucosamine, in parallel, and activation with KOH. During the synthesis, they produced the hydrothermal carbon *via* HTC followed by chemical activation, as a subsequent step. The resulting materials possessed a porous structure, regardless of the carbon precursor, and the microporosity was observed only after KOH activation. The ACs were characterized by large surface areas, between 778 $m^2 g^{-1}$ and 1513 $m^2 g^{-1}$, depending on the activation parameters. ACs with micro–mesoporous structures have been prepared by Fuertes *et al.*,[95] starting from potato starch and eucalyptus sawdust, *via* HTC at 250 °C, and activation with KOH and melamine. The powders had a micro–mesoporous bimodal structure. It was observed that melamine has the ability to extend the pore size distribution range of the activated carbons, generating mesopores.[95] Again, independent of the biomass source, the surface areas were improved by the melamine incorporation, reaching a maximum of 3420 $m^2 g^{-1}$, and 2.37 $cm^3 g^{-1}$ for pore volume. Boyjoo *et al.*[98] reported the synthesis of ACs starting from Coca-Cola *via* HTC, followed by chemical activation with $ZnCl_2$, denoted as CMC_1 and CMC_2 (mass ratio of $ZnCl_2$/HTC carbon = 1 and 3, respectively), and with KOH, denoted as CMC_3 (KOH/HTC carbon = 4). Surface area measurements revealed the formation of microporous structures. The nonactivated sample presents a moderate surface area, 405 $m^2 g^{-1}$, and pore sizes in the micropore domain, maybe due to H_3PO_4 present in the biomass. The samples activated with $ZnCl_2$ achieve surface areas of about 1082 $m^2 g^{-1}$ and 80% of the pore volume consists of micropores. On increasing the amount of activator, the surface area almost doubles, but the pore size distribution shifts towards mesopores, with the percentage of narrow micropores (<0.8 nm) decreasing down to 29%. Plata *et al.*[130] reported the synthesis of ACs prepared through H_3PO_4-assisted HTC, from different biomass sources (sawdust, almond shells, hemp residues and coconut shells) and H_3PO_4 for pore development. In a typical synthesis the biomass was dispersed in a certain amount of H_3PO_4 and deionized water, and HTC was performed at 200 °C for 24 h. Also, in the presence of an activation agent, the carbon yield was higher, probably because H_3PO_4 acts as a catalyst for the hydrothermal carbon formation.

2.2.3. Summary. To date, HTC has been intensively reported as one of the best strategies to produce carbon materials with tunable physical and chemical properties. By combining the HTC with templating approaches, the HTC carbon structure can be highly improved in terms of surface area and pore volume. Also, chemical and physical activation helps to enhance the specific surface area and create porosity. Table 1 summarises a few examples of materials prepared *via* HTC in combination with templating strategies or activation processes as well as their main porosity features (surface area and total pore volume).

3. Heteroatom doped carbon materials

As described in the previous section, HTC can be successfully used in the production of porous carbon materials using renewable resources. Furthermore, due to the versatile character of this technique, different strategies can be used in tandem in order to boost the properties of the final materials, as presented in section 2.2. Although the textural properties promote this type of material as a good candidate for application in gas storage fields or water treatment experiments, sometimes its chemical and physical properties are limited, making it a second option candidate for applications such as electrocatalysis or energy storage. A very common method to overcome this consists of functionalization of the carbon structure with various heteroatoms, such as nitrogen,[105,136] boron,[137,138] sulphur[121,139] and phosphorus.[140] This brings some advantages including improved catalytic performance and better selectivity for different reactions, such as the oxygen reduction reaction, and higher adsorption capacity when it comes to gas storage and water treatment.

3.1. Nitrogen-doped carbon materials

Nitrogen-doped carbon materials (NCs) have received recognition since the earlier studies, due to their remarkable chemical and physical properties. The hydrothermal carbon is highly improved by N incorporation due to the following reasons: the nitrogen atoms are more electronegative than carbon, due to the two lone pair electrons, and this provides a higher electrochemical activity for the NCs, which makes them potential catalysts for the oxygen reduction reaction and CO_2 reduction;[87] N-doping effectively increases the electrical conductivity and creates defects that can provide enough space for ion, electrolyte or gas diffusion that make them viable for gas storage,[141] fuel cells and energy storage.[139,142] NCs can have different structures, such as 1-D N-doped carbon nanotubes (NCNTs),[143] N-doped nanofibers (NCNFs),[144] 2-D N-doped graphene (NG)[145] or 3-D hierarchical nanostructures with different dimensions.[146] Depending on the N-bonding, four

Table 1 Surface area and pore volume of various carbonaceous materials prepared *via* HTC coupled with soft/hard templating or chemical/physical activation

Sample name	Carbon precursor	Synthesis method	Template/activating agent	S_{BET} ($m^2\ g^{-1}$)	PV ($cm^3\ g^{-1}$)	Ref.
NPCSs	Phenol-formaldehyde	Soft templating-HTC	Pluronic F108	1480	0.9	111
BHCSs	Ascorbic acid		Trioctylamine@ferrocene-in-water emulsion	199	NA	93
OHTC-1	Glucose	Soft and hard templating-HTC	Pluronic P123, TEOS	520	0.40	94
HPNC-1	Glucosamine hydrochloride	Soft templating-HTC	Pluronic P123, 0.5 mmol, pH = 7	550	0.43	96
HPNC-2			Pluronic P123, 0.25 mmol, pH = 2	650	0.54	96
HPNC-3			Pluronic P123, 0.75 mmol, pH = 2	710	0.54	96
HPNC-4			Pluronic P123, 1 mmol, pH = 2	980	0.78	96
HPC-3	Glucose		Pluronic P123, 0.75 mmol, pH = 2	490	0.29	96
Assai-MW-CO_2	Assai stone	Microwave-assisted HTC and physical activation	CO_2 (80 ml min^{-1})	1100	0.45	131
CNSA_6	Peanut skins	H_2SO_4 assisted HTC and chemical activation	KOH (1 : 1 mass ratio)	1886	1.02	128
HPCS_1.2	Starch	HTC-chemical activation	$(NH_4)_2Fe(SO_4)_2$	973	0.27	132
AC hydrochar – dry impregnated KOH	Giant bamboo		KOH (4 : 1 mass ratio)	2117	1.14	133
Hydrochar – wet impregnated KOH				2262	1.30	133
BCF	Bamboo sticks		KOH (6 : 1 mass ratio)	12	—	134
CMC-1	Coca Cola waste		$ZnCl_2$ (1 : 1 mass ratio)	1082	0.43	98
CMC-2			$ZnCl_2$ (3 : 1 mass ratio)	1994	0.87	98
CMC-3			KOH (4 : 1 mass ratio)	1405	0.80	98
COSHTC_3	Coconut shell		NaOH (3 : 1 mass ratio)	876	0.44	85
AA-0	Potato starch		KOH (4 : 1 mass ratio)	3000	1.41	135
AA-2M			KOH (4 : 1 mass ratio) and melamine (2 : 1 mass ratio)	3280	2.37	135
AA-3M	Potato starch		KOH (4 : 1 mass ratio) and melamine (3 : 1 mass ratio)	3220	2.27	135
AC-0	Cellulose		KOH (4 : 1 mass ratio)	3100	1.46	135
AC-2M			KOH (4 : 1 mass ratio) and melamine (2 : 1 mass ratio)	3540	2.22	135
AS-0	Sawdust		KOH (4 : 1 mass ratio)	2690	1.28	135
AS-2M			KOH (4 : 1 mass ratio) and melamine (2 : 1 mass ratio)	3420	2.30	135
AS-3M			KOH (4 : 1 mass ratio) and melamine (3 : 1 mass ratio)	2990	2.35	135

main types of N can be distinguished: pyrrolic N, pyridinic N, quaternary N/graphitic N and N oxides of pyridinic N (illustrated in Fig. 17).

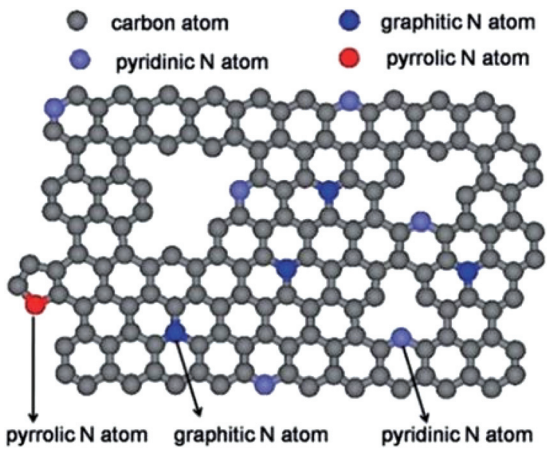

Fig. 17 Schematic structure of N doped carbons; reproduced with permission from ref. 147.

Usually, the carbon is functionalized during HTC followed by high-temperature annealing.[148] A wide range of nitrogen precursors can be used, including ammonia,[149] urea,[148,150] melamine,[151] nitric acid[152] *etc*. The chemical and physical properties, pore structure, content and types of nitrogen functionalities are all influenced by the nitrogen precursors and heat treatment conditions. Liu *et al.*[153] reported the synthesis of NCs using natural biowaste as a carbon precursor and melamine as a N source, succeeding in incorporating about 1.75 at% N, according to XPS data. Starting from chitosan and gaseous NH_3, Wu *et al.*[154] proposed the synthesis of NCs *via* HTC for energy storage applications and CO_2 capture. In this way, they synthesised two sets of materials: NCs derived from chitosan and NCs derived from glucose and gaseous NH_3. The nitrogen incorporation was much more successful for the carbons obtained *via* the HTC of chitosan, about 4.61 wt% N was incorporated, and half of it was attached in the pyrrolic form. When NH_3 was used as a N donor, more pyridinic functionalities were reported, with a N content of about 3.58 wt%. Using aqueous NH_3, Schipper *et al.*[155] reported the synthesis of NCs *via* the HTC of glucose, containing about 9 wt%

N. Zhang *et al.*[156] synthesised NCs with 5.5 at% N, starting from the HTC of glucose, followed by dry impregnation of the resulting hydrothermal carbon with melamine. Ren *et al.*[157] reported the HTC of NCs derived from microalgae, containing up to 2.89 at% N, coming exclusively from the biomass source. Preuss *et al.*[136] reported the usage of lyophilised ovalbumin from chicken egg white as a N source for the synthesis of NCs, starting from glucose and using HTC. The highest N content obtained in this study was 3.3 at%, which reduces to 2.9 at% after further activation is applied. Qiao *et al.*[158] reported that the NCs improve the electrocatalytic activity of multiwall carbon nanotubes towards oxygen reduction reactions. The N was incorporated mostly as graphitic N (57.16%) and pyridinic N (18.26%), the rest being coordinated with Fe or in an oxidized form. Alatalo *et al.*[159] performed the synthesis of NCs starting from glucose and cellulose in the presence of a soy bean additive as a structure directing agent and a nitrogen precursor. The resulting materials showed good nitrogen incorporation: between 1.0 and 3.7 wt% for pristine materials and 0.2–1.9 wt% for calcined carbons. Table 2 shows a few more examples of NCs synthesised in the literature.

The examples mentioned above are proof that incorporation of nitrogen atoms within the carbon structure using HTC is possible, but how nitrogen incorporates into the carbon structure is still under debate. So far, the Maillard mechanism[164] has been accepted as playing an important role in the process. The mechanism consists of a group of reactions between reducing sugars and amino acids. It is impossible to provide a clear pathway for the formation of NC materials during HTC because throughout these reactions, hundreds of compounds can be formed and react again themselves. The main steps of the Maillard mechanism are described in short in Fig. 18.[89]

The first products formed during the Maillard reaction are glucosamines *via* a nucleophilic attack of an amine on the aldehyde of the sugar (Fig. 18, I). The glucosamines are further transformed to a Schiff base, by dehydration (Fig. 18, II) which can, in turn, suffer rearrangements to aminoketones (Fig. 18, III and IV). Compound III can form an α-dicarbonyl species (Fig. 18, V), which after successive dehydration can form 5-HMF, the main intermediate compound formed during HTC.[89]

Table 2 Example of NCs synthesised in the literature

Sample name	Carbon precursor	Nitrogen source	Nitrogen content (at%)	Ref.
AG650	Glucose and microalgal mixtures	Microalgae	2.65	127
AG700			1.43	
AG750			0.68	
N-GCS-2	Peach extract	NH_4OH	9.33	160
AMBC-600	Bamboo shoot	Melamine	12.9	161
AMBC-700			6.2	
AMBC-800			2.7	
HPCS-1.2	Starch	$(NH_4)_2Fe(SO_4)_2$	2.3	132
H-N400	Sucrose	$(NH_4)_2SO_4$	6.57	162
H-N600			7.33	
H-N800			6.54	
GN-700-4	Glucose	Urea	6.20	163

3.2. Sulphur doped carbon materials

Together with N, sulphur has gained a lot of attention as a dopant for the carbon structure. Sulphur-doped carbons (SCs) are widely used as cathodes for Li–S batteries, due to the high theoretical capacity of S (around 1675 mA h g^{-1}).[165] Other applications of SCs include electrodes for supercapacitors,[166] energy storage as hydrogen storage media,[166] photoactive materials for light-harvesting and electrocatalysis. SCs can be usually prepared using two strategies: (i) incorporation of S into the structure of synthetic or commercial carbon using a sulphur precursor by sulphurisation,[167] and (ii) heating of mixtures of carbon and sulphur precursors.[168,169] Generally, the sulphur donor can be any sulphur-containing compound, including elemental sulphur, H_2S, SO_2, CS_2, sulphur-containing organic compounds and polymers.[121,139,166,170] Emran *et al.*[171] proposed the synthesis of sulphur-doped carbon microspheres (S-MCMS) *via* a one-pot HTC for the motorisation of ascorbic acid and lemon juice in food and pharmaceuticals. S-MCMS were prepared from D-glucose and thiourea as the S source, followed by annealing at different temperatures (700 °C, 800 °C, and 900 °C). The obtained materials had an average size of 0.5–5 μM and a highly microporous structure. The annealing temperature had a high influence on the structure, and S-MCMS-900 possessed the highest surface area, with the smallest sphere size and more sp^2 carbon chain distortion. Roldán *et al.*[172] synthesised SCs *via* the HTC of D-glucose activated with $ZnCl_2$ and thiophenecarboxaldehyde as the S source. For comparison, NCs and N, S-doped carbon materials have been prepared using the same approach. The SCs possess C–S–C bonding derived from the thiophenic group and a small amount of S was linked to Zn, forming ZnS sphalerite, inhibiting, in this way, the complete removal of the activating agent. In terms of textural properties, the SCs exhibited surface areas around 550 m^2 g^{-1} with a 0.9 cm^3 g^{-1} pore volume, and according to XPS results 6.7 wt% of the sulphur was incorporated. In an earlier study, the same author prepared SCs for water treatment applications.[168] Using the same approach, they prepared mesoporous SCs. For comparison, NCs were also prepared. SCs possessed a mesoporous structure, with 89% mesoporosity and a pore size of approximately 34 nm, containing a high amount of S atoms incorporated onto the carbon structure, 8.3 wt%, which is double that of the N atoms incorporated, 3.9 wt%.

3.3. Boron doped carbon materials

Besides nitrogen and sulphur, boron represents a promising dopant for carbon materials. The advantage of boron incorporation lies in the fact that it creates defects, by introducing an uneven charge distribution which enhances the electrochemical performance by improving the charge transfer between neighbouring carbon atoms.[173] Also, the incorporation of boron could improve the conductivity of carbon materials by increasing the density of hole-type charge car-

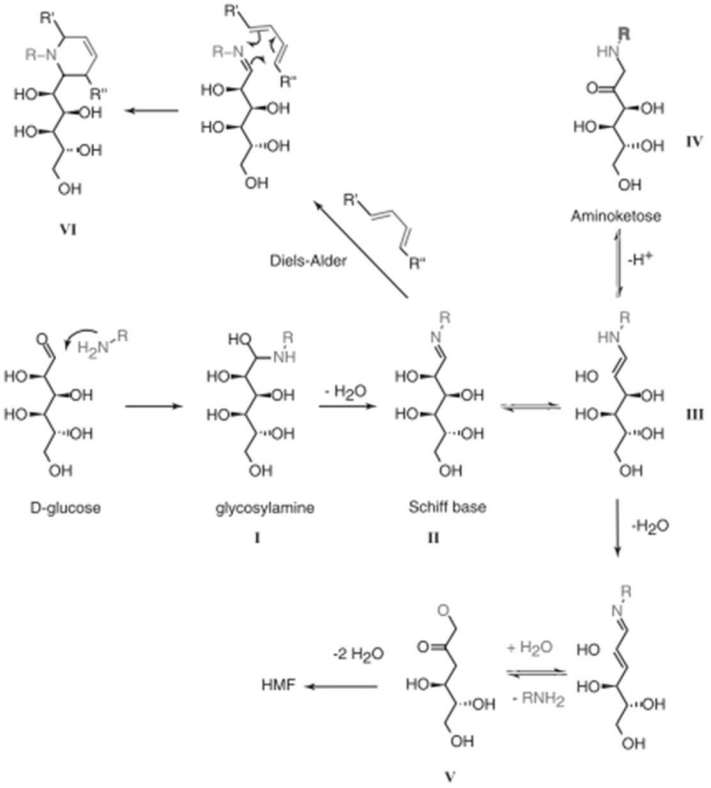

Fig. 18 Some examples of the Maillard reaction; reproduced with permission from ref. 89.

riers.[174] All these improvements make them good candidates for different applications, such as energy storage[175] and electrocatalysis.[144,173,174] Sun *et al.*[176] reported the synthesis of boron-doped porous graphitic carbon materials (BCs) derived from chitosan (BNGC-2-900). The resulting hydrothermal carbon was chemically activated using $ZnCl_2$ followed by carbonisation at elevated temperatures (900 °C). The produced BCs had high surface areas, up to 1567 $m^2\ g^{-1}$, and a pore volume of about 0.48 $cm^3\ g^{-1}$. XPS results revealed the presence of carbon, nitrogen (4.99%), boron (3.47%) and oxygen atoms. The successful doping of the materials with boron was confirmed by the presence of peaks from the C 1s spectrum corresponding to C–B (283.4 eV), C–C (284.7 eV), C–N (285.6 eV), C–O (286.1 eV), C═O (286.4 eV), and C–O–B (288.7 eV). Incorporation of boron atoms in the hydrothermal carbon can affect both the morphology and particle size, according to a study conducted by Kalijadis *et al.*[138] For their synthesis, different concentrations of boric acid (0.1, 0.2, 0.6 and 1 wt%) were mixed with D-glucose and HTC was performed at 180 °C for 24 h. For the undoped sample, the particles present a uniform diameter of about 3 μm and a few particles were about 7 μm. By incorporation of boron atoms, the particle size is increased, up to 20 μm, and the degree of homogeneity is decreased. This enlargement phenomenon is attributed to the catalytic effect that boric acid could have during the HTC, by effective conversion of D-glucose to produce 5-HMF. Based on textural characterisation, BCs consist of a microporous structure, with surface areas between 73 $m^2\ g^{-1}$ and 362 $m^2\ g^{-1}$ and boron content between 0.05 and 0.19 wt%.

3.4. Phosphorus doped carbon materials

Phosphorus (P) is another important heteroatom that gained its place on the list of dopants for the carbon structure. P doping can bring a lot of advantages to the carbon structure, such as improving electrochemical stability by suppressing the formation of electrophilic oxygen species and inhibiting the combustion of the oxygen species, which consequently also contributes to enhancing the cycling stability, capacity retention ratio and operating voltage window for capacitors.[140] Regarding their synthesis, P doped carbon materials (PCs) can be prepared either in a two-step synthesis of mesoporous carbon followed by P incorporation,[177] or through a one-pot HTC.[178] Li *et al.*[177] reported the synthesis of P and N co-doped carbon microspheres following a two-step strategy using D-glucose and $(NH_4)HPO_4$. Both doped and undoped materials present a spherical morphology with a smooth surface, as shown by SEM (see Fig. 19a and b). The heteroatom incorporation was confirmed by XPS measurements, with P–O, P–C and C–N bonds being identified. Quantitative XPS analysis revealed that P was incorporated at ~1.19 at% and N at 1.00 at% in NPCM.

Wu *et al.*[178] synthesised PCs starting from glucose and tetraphenylphosphonium bromide ($C_{24}H_{20}P(Br)$) *via* HTC combined with a soft templating method. The mixture was treated

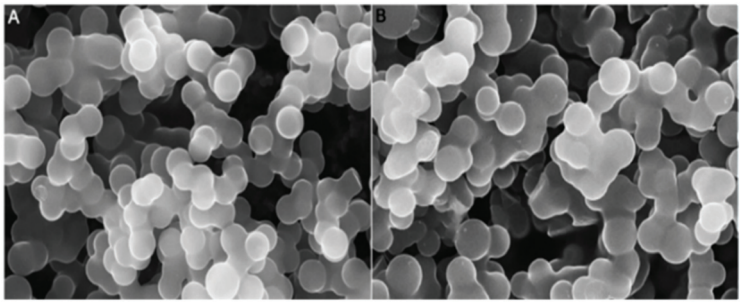

Fig. 19 SEM images of (A) CM and (B) NPCM; reproduced with permission from ref. 177.

at 180 °C for 4 h during HTC, followed by template removal at 800 °C for 2 h, under an inert atmosphere. During the synthesis, the amount of P donor was varied, and the resulting samples were denoted as P-CHS-1, 2 and 3, with the increasing number referring the increment of the P donor. For comparison, undoped samples were also prepared. P incorporation was examined by FTIR: when comparing CHS and P-CHS-2, similar peaks are identified, at 3060 cm^{-1} for aromatic C–H stretching vibrations and aromatic C–H out of plane deformation vibrations below 900 cm^{-1}, aliphatic C–H stretching vibrations at 2857 and 2924 cm^{-1} and C–H scissoring vibrations at 1453 cm^{-1}. This is clear evidence that the HTC of D-glucose is not influenced by P doping. The C=C band is present in both samples, with vibrations at 1588 cm^{-1}, and both contain O–H (3440 cm^{-1}), C=O (1705 cm^{-1}) and C–O (1278 and 1026 cm^{-1}) bands. Among all these peaks, P-CHS-2 shows a few more, at 1109 cm^{-1} assigned to P–O combination, at 1085 cm^{-1} assigned to the ionized linkage P^{+}–O^{-} or P–O–C, and two vibration bands at 725 and 682 cm^{-1}, due to P–C, which confirms the doping of P in the carbon. Guo *et al.*[179] prepared phosphorus-doped carbon nanotubes (PCNTs). For this, the mixture was heated at 170 °C for 12 h. Compared to raw CNTs, PCNTs show a lower surface area and a smaller pore volume of pores, due to the removal of highly disordered amorphous carbon regions. The functional groups on the surface of PCNTs were investigated by XPS. The amount of P was about 1.66 at% and O was about 6.98 at%. Overall, the –P–O groups were dominant, and they formed *via* the acid reaction with the –OH groups from the edge of the sp^2 nanotube layer. The main P containing groups were –P=O and –P–C.

3.5. Summary

Heteroatom doped carbon materials showed their potential in a wide range of applications, but they seem a "go to" option in fields such as electrocatalysis for the ORR or CO_2 reduction and supercapacitors. As presented above, HTC represents a useful method for the synthesis of NCs, SCs, BCs or PCs either in one pot or two step reactions. The advantage of HTC over other synthesis methods lies in the possibility of being able to use sustainable carbon precursors and any source to dope the heteroatom. Also, HTC implies a small energy consumption and the process itself is easy and eco-friendly.

4. Applications

Porous carbon materials have been used in multiple applications since long ago. There is clear evidence of the usage of ACs along the years, for example in ancient times charcoal was used to adsorb unpleasant odours or to clean water. Later, in 1773, AC was mentioned as an adsorptive material in a gas experiment by Scheele. In 1862, Frederick Lipscombe rinsed activated carbon for commercial applications, by using the material to purify potable water, and in 1881 Heinrich Kayser mentioned the ability of charcoal to take up gases. ACs were implemented at the industrial scale at the beginning of the twentieth century, by Chemische Werke, and during the First World War it was used in gas masks by American soldiers to protect them from poison gas.[180–183] Due to a series of advantages, such as the low cost of the raw materials, the high degree of microporosity,[127] high surface areas (1000 m^2 g^{-1}),[184] and their good chemical and thermal stability, porous carbon materials are used in a wide range of applications, as described below.

4.1. Energy storage

Hydrothermal carbons represent a useful and sustainable class of materials for use in energy storage. They have been extensively explored as graphite replacements in lithium-ion batteries and have enabled the development of sodium-ion technologies which have been previously inaccessible, as well as further the development of supercapacitor electrodes and fuel cells.

4.1.1. Batteries. Li-ion batteries are a well-established and widely available commercial technology, used extensively as power sources for portable devices such as mobile phones and laptops, power tools, electric vehicles, and many other consumer products, since they are lightweight and have a high energy density. Carbon is the most commonly used anode material, traditionally in the form of graphite, which is naturally occurring, abundant and inexpensive. However, recent developments have been made in the use of hard carbons for electrode materials, which are able to achieve significantly higher capacities, and show an improved rate capability, cyclability and efficiency. Furthermore, the field of sodium-ion batteries is growing rapidly and suitable anodes are also

necessary, since graphite cannot be used in an analogous way. Hard carbons have also been found to be effective anodes for sodium-ion batteries, with a rapidly growing body of literature.

HTC is an appealing route for obtaining useful carbon materials from cheap and abundant biomass; for example, holly[185] and ginkgo leaves,[186] sugarcane,[187] sweet potato,[188] pollen,[189] peanut skin[128,190] apricot shell,[191] and corn stalks[192] have all been converted hydrothermally for use in energy storage applications. Several studies have compared hydrothermally treated precursors against directly pyrolysed biomass and found that those materials which have first undergone HTC function significantly better as electrodes in lithium- or sodium-ion batteries. Wang *et al.*[190] attributed the larger initial capacity achieved in their hydrothermally treated peanut skin to the presence of significant micropores and mesopores, and showed that a higher fraction of mesopores was desirable for fast ion diffusion channels. In contrast, two reports by Zheng *et al.* comparing HTC and direct pyrolysis of holly leaves[185] and sweet potato[188] found that the greater microporosity introduced by HTC played an important role in the improved electrochemical performances. The discrepancies between these studies likely arise from the intrinsic differences in the nanostructure of the starting biomass. The storage mechanism of sodium in hard carbons is still poorly understood, and hydrothermally treated biomass was used as the precursor for tailored structures in these fundamental studies. Hard carbons derived from reed straw and carbonised at 900–1500 °C exhibited variations in graphitic domains and microporosity, resulting in different contributions to both the sloping and plateau capacity regions.[193] Sodium storage in the sloping region was attributed to adsorption in the micropores and defect sites, and Na^+ intercalation into the graphite-like layers in the plateau region (Fig. 20 and Table 3).

Hydrothermally prepared shaddock peel was used to investigate the relationship between capacity and disordered turbostratic nanodomains, with the resulting carbons exhibiting mainly sloping capacity.[199] The main mechanism of sodium-ion storage was attributed to the balance of charge conductivity, the sodium-ion diffusion rate, and the number of adsorption sites. Well-defined precursors, such as glucose[194] or phenolic resin,[200] are also often used for systematic studies. For phenolic resin carbonised at 800–1500 °C, it was found that increasing carbonisation temperatures decreased the *d*-spacing between graphitic layers, and promoted the shift from microporosity to mesoporosity in the materials, resulting in a decrease in surface area and total pore volume.[200] The material carbonised at intermediate temperature (1250 °C) showed the best reversible capacity which was attributed to the balance between optimised *d*-spacing and the pore structure. Interestingly, the material carbonised at 1500 °C had the highest first cycle coulombic efficiency (62.5%), due to the lower surface area resulting in less significant SEI formation (Fig. 21a), whilst the material carbonised at a lower temperature (1000 °C), despite being less electrically conductive, exhibited a better rate capability at higher C rates, arising from the wider *d*-spacing (Fig. 21b).

Hard carbons exhibit good capacity retention, but often poor rate capability; conversely, pure soft carbons have superior rate capability, but suffer rapid capacity fade. Combining the two can result in a composite anode with improved electrochemical properties. Hard–soft composites prepared for K-ion batteries exhibited a higher rate capability than the pure hard carbon (81 mA h g^{-1} *vs.* 45 mA h g^{-1} at 10 C) and superior cycling stability compared to pure soft carbon (93% *vs.* 55% after 200 cycles at 1 C).[196] The hard carbon provided a porous and robust structure to accommodate the intercalation of potassium ions, whilst the conductivity offered by the soft carbon regions facilitated fast ion transport to maintain performance at high current rates. Similarly, hard carbon spheres with a soft carbon coating displayed improved initial coulombic efficiency (54% to 83%) and a capacity retention of 93% after 100 cycles, when tested as anodes in Na-ion batteries.[197] In addition, they found that increasing the carbonisation temperature from 1000 °C to 1600 °C could significantly increase the plateau capacity, hypothesising that this effect was due to the larger number of nanopores at higher temperature. The direct addition of graphene derivatives is another common approach for synthesising hard/soft composites; often graphene/graphite oxide is combined with the hard carbon precursor prior to HTC, which serves to reduce the graphene sheets *in situ*.[187,198] In these studies, the enhanced sodium storage capacity and cycling stability of the composite were ascribed to the complementary effect of the different morphological characteristics of the carbons which provided ample sodium storage in the micropores and large interlayer spaces, minimised volume variation during cycling and ensured sufficient contact area with the electrolyte for efficient diffusion and charge transport.[198] Aside from pure carbon materials, various carbon/inorganic composites have been explored as electrode materials.[195,202,203] For Li-ion batteries, elements such as Si and Sn are promising since lithium can form alloys with either in a ratio of 4.4 : 1, resulting in a significantly higher theoretical capacity (*e.g.* $Li_{4.4}Si$ 4200 mA h g^{-1} *vs.* 372 mA h g^{-1} for LiC_6 in graphite). Unfortunately, formation of these alloys is generally accompanied by severe volume changes, leading to rapid capacity fade with cycling. Furthermore, some of the alloy species are soluble in the electrolyte solution and thus the anode gradually decomposes. In addition, such materials on their own have low intrinsic conductivity which can result in overall poor performance. In several studies, the combination of these inorganic particles with hard or soft carbons serves to stabilise volume changes and improve conductivity, resulting in superior cycling performance. A comparison between hard carbon-coated SnO_2 and a mechanically mixed composite demonstrated that the carbon coating could significantly stabilise capacity fading.[191] Jeong *et al.*[201] produced silicon coated hard carbon attached to a graphite scaffold; the overall reduced contact area with the electrolyte served to suppress SEI formation, whilst the graphite facilitated electron transport. The report further showed that the electrode thickness and amount of binder strongly affected the lithiation capacity; particularly in the case of alloy

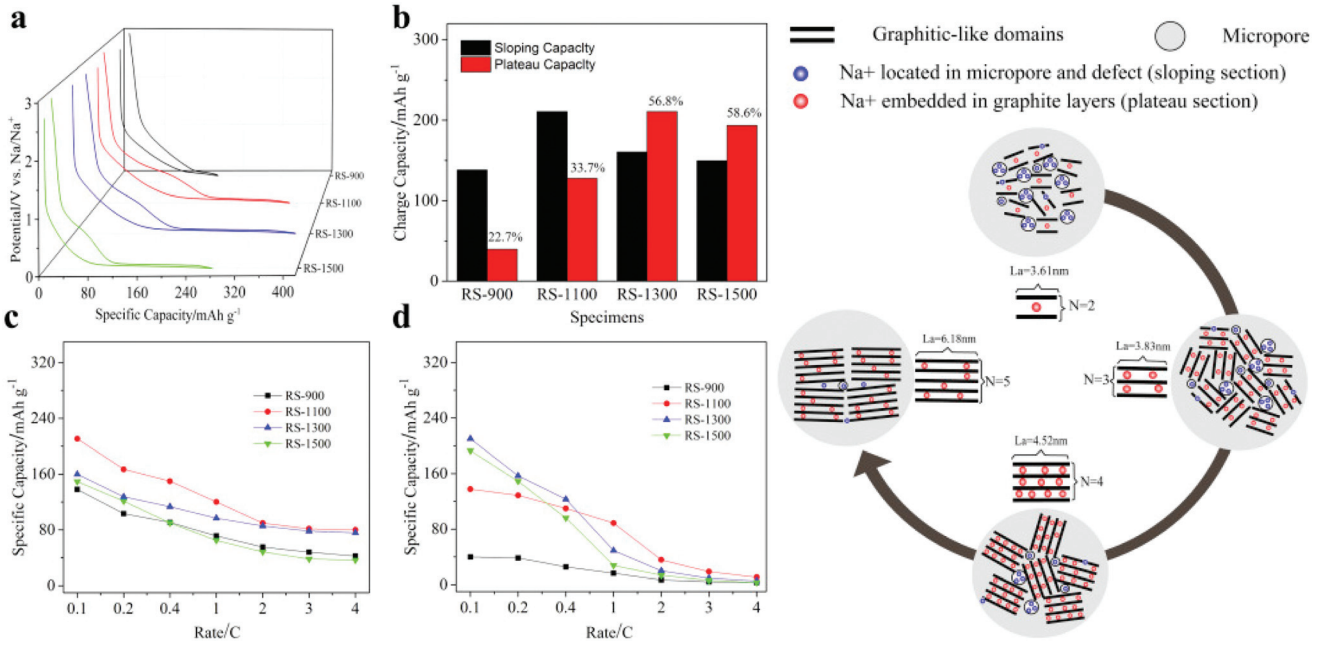

Fig. 20 LHS: (a) Plateau and sloping curves of RS-x electrodes. (b) Amount and contribution rate of capacity from the plateau and sloping region in RS-x electrodes; capacity contributed at 0.1–4 C by (c) sloping regions and (d) plateau regions. RHS: Schematic illustration of the sodium storage mechanism of RS-x electrodes. Reproduced with permission from ref. 193.

materials, the binder content can additionally stabilise volume expansion and contraction on cycling, an important factor which is not often discussed in the literature. Similarly, Zhang *et al.*[204] supported SnO_2 particles on rGO and used the growth of hard carbon on the surface to limit the particle size, resulting in a uniform size distribution. Good contact between SnO_2 particles and the hard carbon-rGO scaffold was achieved by C–O–Sn covalent bonds which enhanced conductivity, whilst the rGO/hard carbon matrix prevented agglomeration of SnO_2 and limited the volume expansion to improve cycling stability. Carbon/transition metal oxide and dichalcogenide electrodes are also being developed for energy storage.[207,209] An electrode material derived from avocado and MnO, coated with alumina for stability, was tested in a Li-ion cell, and the high capacity and good rate capability (Table 2) were explained by the structure inherited from the avocado precursor which provided a good buffer for volume expansion, and the Al_2O_3 coating with greater ionic conductivity.[210] In another study with MnO-graphene nanopeapods, structural stability was introduced with a graphene scaffold, which also enhanced electrical conductivity, resulting in high Li storage capacity.[211] For Na-ion batteries, analogous carbon-supported MoS_2 materials showed promising performance, in which MoS_2 nanosheets were vertically grown on cotton-derived carbon fibres which act as a robust conductive support and result in greatly enhanced cycling stability. Even at high current densities, much higher capacities could be maintained, compared to the capacity retention of bare MoS_2 nanosheets. In a similar approach, MoS_2 nanosheets were grown on the surface of carbonised corn stalks, whereby the intrinsic structure of the biomass precursor served to stabilise the electrode during long cycles and at high current densities.[192] Hydrothermally prepared MoS_2 was combined with PVP and SnO_2 and it also showed excellent cycling stability at high current densities for both Na and K storage[206] attributed to the sandwich structure formed by the MoS_2 and carbon coating. Well-aligned nanosheets of SnS_2 have been grown hydrothermally on a carbon cloth (Fig. 22), and when tested as an anode for sodium-ion batteries they exhibited enhanced electrochemical properties in comparison with pure SnS_2.[205] The enhanced behaviour was attributed to the introduction of the carbon cloth substrate, which provided the contact area for both the electrolyte and active material and enabled rapid Na-ion transport, improved electrical conductivity, and relieved aggregation and pulverisation of the SnS_2 nanosheets.

Cathode materials have also been developed using similar methodology, for example, the hydrothermally assisted synthesis of $Na_7V_4(P_2O_7)_4(PO_4)$/C nanorods, which are formed by simultaneous crystallisation of $Na_7V_4(P_2O_7)_4(PO_4)$ and *in situ* carbonisation of surfactants on the surface.[212] The carbon formed as a thin layer around the nanorods, and limited particle growth, resulting in a uniform particle size. With an aqueous electrolyte, a capacity of 51.2 mA h g^{-1} was achieved at a current density of 80 mA g^{-1}, and 72% of the initial capacity was maintained even at 1000 mA h g^{-1}. The hydrothermal production of a $Na_3V_2O_{2x}(PO_4)_2F_{3-2x}$/carbon composite further demonstrated the importance of the conductive carbon for overall cell performance.[213] In a Li–S system, a composite electrode of nickel, sulfur and carbon derived from bamboo exhibited a high initial capacity (1198 mA h g^{-1} at 0.2

Table 3 Electrochemical performance of carbon and composite battery anodes obtained by HTC. FCCE: first cycle coulombic efficiency

Precursor	Hydrothermal conditions	Carbonisation temperature	Activation	Template	Reversible capacity (mA h g^{-1})	FCCE (%)	Application	Ref.
Glucose	180 °C, 24 h	1100 °C (Ar), 800 °C (H_2)	—	—	160 at 50 mA g^{-1}	—	Na-ion	194
Glucose	180 °C, 6 h	800 °C (N_2), 300 °C (air)	—	Na_2MoO_4 template	250 at 50 mA g^{-1}	50	Na-ion	195
Sugar/ perylenetetracarboxylic dianhydride (PTCDA)	195 °C, 5 h	1100 °C (HTC glucose), 900 °C (HTC glucose + PTCDA)	—	—	261 at 28 mA g^{-1}	67	K-ion	196
Sucrose, toluene	190 °C, 5 h (sucrose)	1600 °C (HTC sucrose + toluene)	—	—	312 at 30 mA g^{-1}	83	Na-ion	197
Sucrose, graphite oxide	190 °C, 12 h	700 °C	—	—	296 at 50 mA g^{-1}	44	Na ion	198
Sugarcane bagasse, graphene oxide	150 °C, 4 h	750 °C (treatment and activation of sugarcane)	KOH	—	617 at 200 mA g^{-1}	56	Li-ion	187
Holly leaf	180 °C, 10 h	800 °C	—	—	318 at 20 mA g^{-1}	50	Na-ion	185
Ginkgo leaf	250 °C, 12 h	700 °C	KOH	—	200 at 200 mA g^{-1}	31	Na-ion	186
Sweet potato	160 °C, 10 h	800 °C	—	—	320 at 100 mA g^{-1}	33	Li-ion	188
Rape pollen grains	180 °C, 24 h	600 °C	—	—	145 at 100 mA g^{-1}	—	Na-ion	189
Peanut skin	180 °C, 12 h	900 °C	KOH	—	681 at 1000 mA g^{-1} (Li), 302 at 100 mA g^{-1} (Na)	45 (Li), 27 (Na)	Li-ion, Na-ion	128
Peanut skin	180 °C, 24 h	800 °C	KOH	—	431 at 100 mA g^{-1}	34	Na-ion	190
Apricot shell	200 °C, 40 h	1000 °C	—	—	184 at 0.1 C	72	Na-ion	191
Reed straw	200 °C, 24 h	1300 °C	—	—	372 at 25 mA g^{-1}	77	Na-ion	193
Shaddock peel	180 °C, 24 h	600 °C	—	—	287 at 50 mA g^{-1}	57	Na-ion	199
Phenolic resin	500 °C, 12 h	1250 °C	—	—	311 at 20 mA g^{-1}	60	Na-ion	200
Nano-Si, sucrose, graphite	190 °C, 6 h	1000 °C	—	—	879 at 30 mA g^{-1}	81	Li-ion	201
Sn, glucose	180 °C, 5 h	500 °C	—	—	452 at 0.5 C (Li), 487 at 0.5 C (Na)	—	Li-ion, Na-ion	202
Polyethylene glycol (PEG), $SnCl_2$	100 °C, 6 h	600 °C (carbon template calcination, H_2/Ar)	—	Crab-shell template	298 at 100 mA g^{-1}	40	Li-ion	203
Graphite oxide, glucose, $SnCl_4$	180 °C, 12 h	—	—	—	1468 at 80 mA g^{-1}	64	Li-ion	204
Carbon cloth, $SnCl_4$, thioacetamide	160 °C, 16 h	—	—	—	1040 at 200 mA g^{-1}	33	Na-ion	205
$SnCl_4$, apricot shell	180 °C, 20 h (SnO_2 synthesis), 200 °C, 20 h (SnO_2-hydrocarbon)	500 °C	—	—	288 at 0.1 C	50	Na-ion	191
Na_2MoO_4, CH_3CSNH_2, polyvinylpyrrolidone (PVP), $SnCl_4$	180 °C, 12 h (MoS_2), 120 °C, 10 h (MoS_2 + SnO_2 + carbon)	500 °C (MoS_2 + SnO_2 + carbon)	—	—	396 at 100 mA g^{-1} (Na), 312 at 50 mA g^{-1} (K)	68 (Na), 73 (K)	Na-ion, K-ion	206
Corn stalks, Na_2MoO_4, thiourea	180 °C, 24 h (MoS_2 – carbon)	600 °C (corn stalks), 650 °C (carbon + MoS_2)	—	—	1231 at 100 mA g^{-1}	72	Li-ion	192
Loofah sponges, graphene oxide, $(NH_4)_6Mo_7O_{24}$, thiourea	160 °C, 6 h (loofah), 200 °C, 24 h (HTC loofah + GO + MoS_2)	400 °C (HTC loofah + GO), 600 °C 2 h (HTC loofah + GO + MoS_2)	—	—	838 at 200 mA g^{-1}	55	Li-ion	207
Cotton, $(NH_4)_6Mo_7O_{24}$, thiourea	220 °C, 24 h	80 °C (H_2/Ar)	—	—	444 at 100 mA g^{-1}	82	Na-ion	208
Cotton, $(NH_4)_6Mo_7O_{24}$, thiourea	220 °C, 24 h	80 °C (H_2/Ar)	—	—	444 at 100 mA g^{-1}	82	Na-ion	208
Citric acid, $(NH_4)_6Mo_7O_{24}$, ascorbic acid	180 °C, 5 h (MoO_2 + carbon)	600 °C (carbon template, H_2/Ar), 400 °C (MoO_2 + carbon)	—	NaCl	367 at 100 mA g^{-1} (Na), 213 at 50 mA g^{-1} (K)	47 (Na), 45 (K)	Na-ion, K-ion	209
Avocado, $KMnO_4$, trimethylaluminium	180 °C, 24 h (avocado)	600 °C (carbon + MnO)	—	—	1165 at 150 mA g^{-1}	67	Li-ion	210
$KMnO_4$, benzoic acid	160 °C, 10 h	1200 °C	—	—	1168 at 50 mA g^{-1}	86	Li-ion	211

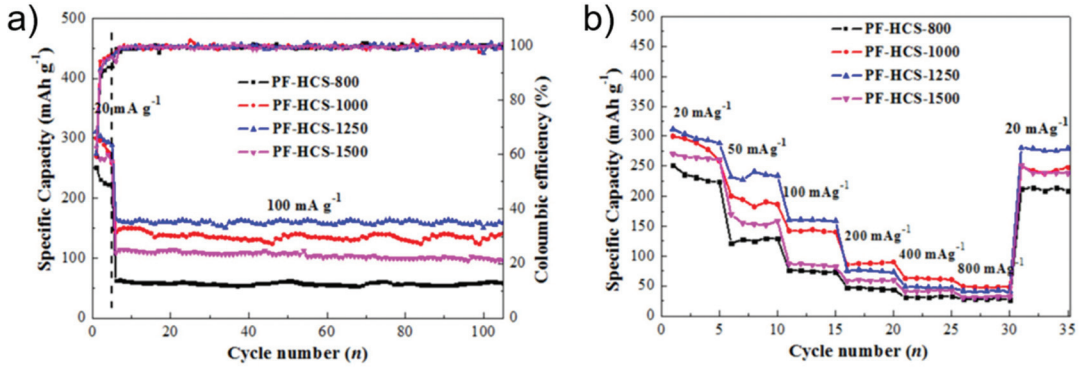

Fig. 21 (a) Cycle performances of phenolic resin-based hard carbon sphere electrodes at 100 mA g^{-1}. (b) Rate performances of phenolic resin-based hard carbon sphere electrodes. Reproduced with permission from ref. 200.

C), good cycling stability (1030 mA h g^{-1} after 200 cycles) and an improved rate capability.[134] These improvements were attributed to the structural stability and high conductivity arising from the Ni particles embedded in the carbon framework. Lastly, peanut shell has been used as both a cathode and anode for a Na-ion hybrid capacitor;[214] hydrothermal treatment of the peanut shell for the cathode resulted in a hierarchically porous material with a sheet-like morphology and a surface area comparable to that of graphene materials (2396 m^2 g^{-1}) and high levels of oxygen doping (~13 wt%). The assembled Na-ion capacitor yielded specific energies of 201, 76 and 50 W h kg^{-1} at specific powers of 285, 8500 and 16 500 W kg^{-1}, respectively, and achieved 88% capacity retention after 100 000 cycles at 51.2 A g^{-1}.

4.1.2. Supercapacitors. While batteries can deliver high specific energy, supercapacitors are a high-power density means of electrochemical energy storage with a long cycle life and a wide operational temperature range, currently unattainable with Li-ion batteries. However, their comparatively low energy density (<10 W h kg^{-1})[215] restricts their use to a few seconds of charge/discharge, thus limiting their more widespread use for energy harvesting applications. There are two main classes of supercapacitors: electric double layer capacitors (EDLCs) and pseudocapacitors. EDLCs store charge *via* electrostatic adsorption of electrolyte ions on the surface of conductive porous electrodes, whereas pseudocapacitors store energy through redox reactions at the interface between the electrode and electrolyte. In general, pseudocapacitors exhibit a higher energy density than EDLCs, but carbon-based materials for EDLCs have superior cycling stability and rate capability, and so can be operated at higher charge and discharge rates and have much longer lifetimes.[215] Hierarchical pore structures enable ion mass transport, and therefore porous carbon materials are an important material for supercapacitor electrodes. HTC materials generally show low porosity and require further activation after treatment. To increase the surface area, KOH activation was applied to HTC carbons from many different biomass sources,[216–221] as well as basic biomass building blocks such as glucose and glucosamine where specific surface areas up to 3000 m^2 g^{-1} were achieved[222] (Table 4). Typical capacitances for these materials are in the range 200 to 350 F g^{-1}, at moderate current densities of 0.1–1 A g^{-1}. The introduction of mesoporosity using $ZnCl_2$ is also beneficial for ion diffusion with an activated hydrothermally carbonised granulated sugar achieving a capacity of 140 F g^{-1}.[223] Another study found that templated starch, using ammonium ferrous sulfate as the porogen,[132] outperformed its unmodified counterparts because the hierarchically porous structure and large SSA contribute a large part to the capacitance mechanism. Yeast cells have also been used as a biological template to synthesise nitrogen-doped porous hollow carbon spheres, followed by *in situ* deposition of MnO_2.[224] The resulting composite exhibited an ultrahigh specific capacitance (Table 4) and when assembled in an asymmetric capacitor the maximum energy density operating at a 2.0 V voltage window was 41.4 W h kg^{-1} at a power density of 500 W kg^{-1} and still maintained 23.0 W h kg^{-1} at a power density of 7901 W kg^{-1} (Fig. 23). Porosity may also be influenced by the solvent; a comparison of ionothermal (ICT) and hydrothermal carbonisation on jujun grass[218] showed that the material derived from ITC exhibited a hierarchical pore structure of micro- and mesopores, not found in the HTC product. Accordingly, the ITC carbon had a high specific capacitance of 336 F g^{-1} at 1 A g^{-1}, whilst the HTC product only reached 220 F g^{-1}.

In addition, the introduction of inorganic nanoparticles to carbon[225,226] or doping with heteroatoms can introduce complementary pseudocapacitive storage mechanisms, thereby improving the overall performance of the material. Nitrogen,[216,218,222,227] oxygen,[219,227] sulfur,[186] and iron[222] have all been incorporated into HTC materials, with the aim of improving capacitance (Table 4). Nitrogen is a common dopant, often arising as a natural component of the precursor.

Interestingly, a comparison of hydrothermally carbonised glucose and glucosamine[216] showed that after activation with KOH, the surface area of HTC glucose was higher than that of HTC glucosamine (1766 *vs.* 1238 m^2 g^{-1}), but that there was no significant difference in their capacitances (280 and 287 F g^{-1},

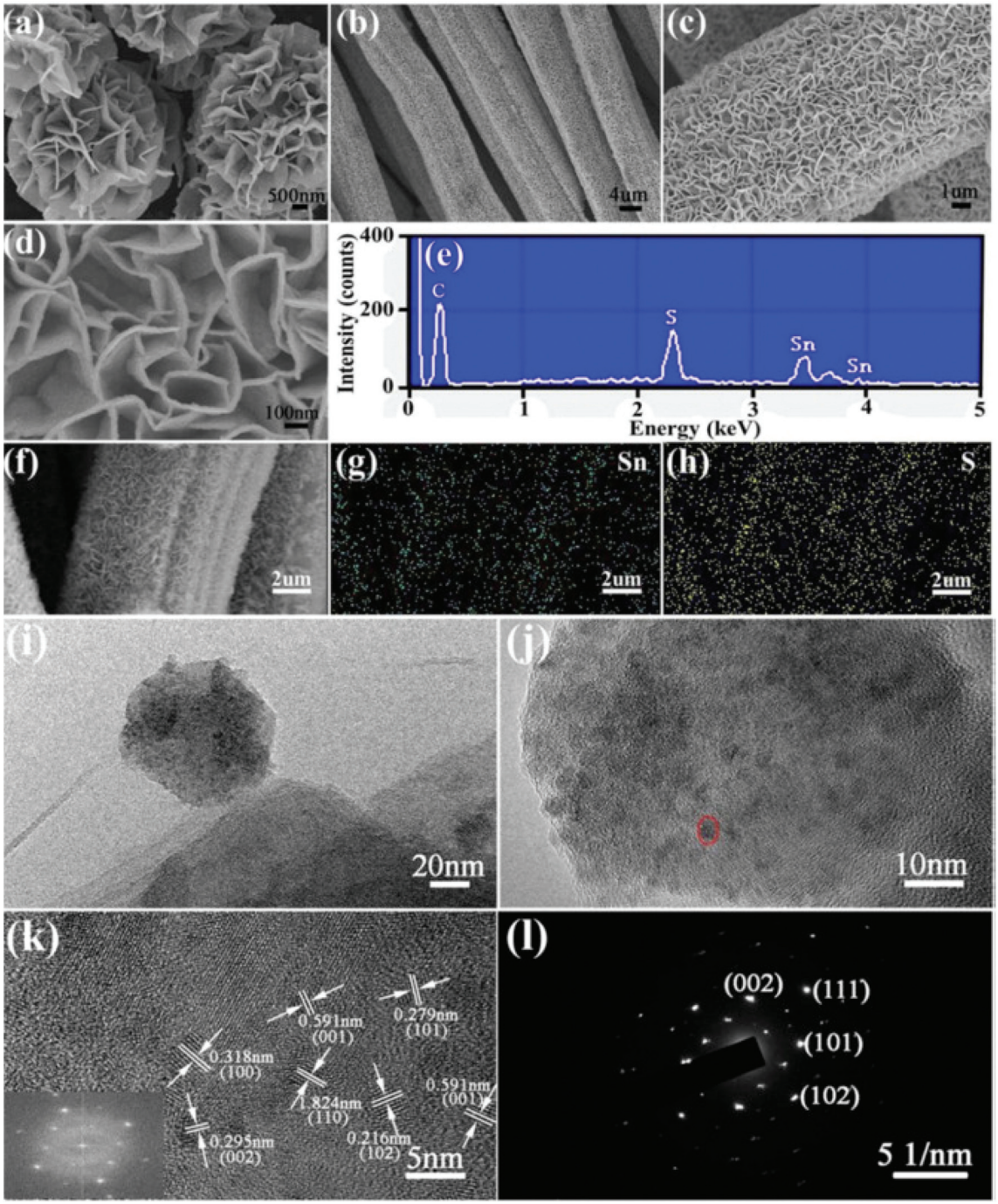

Fig. 22 (a) Larger-magnification SEM images of SnS_2 with a flower-like feature. (b) Typical low-magnification SEM image of SnS_2/CC. (c) and (d) Larger-magnification SEM images of SnS_2 on CC showing the well-aligned nanosheet architecture. (e) EDS exploration of SnS_2/CC. (f) SEM image of the marked region of SnS_2/CC and relevant to EDS plots of (g) Sn and (h) S. (i) TEM and (j and k) HRTEM images, with inset showing the FFT pattern, and (l) the corresponding SAED pattern of the SnS_2 sample. Reproduced with permission from ref. 205.

respectively, at 0.2 A g^{-1}). The discrepancy was ascribed to the presence of pyridone and pyridine groups which contribute pseudocapacitance, and of pyrrole groups which improve electron mobility and electron transfer reactions in the carbon matrix. Nitrogen- and oxygen-doped hydrothermally carbonised tobacco rods showed a high capacitance of 286 F g^{-1} at 0.5 A g^{-1}, and excellent cycling stability.[227] The enhanced performance compared to that of commercial activated carbons was attributed to the presence of heteroatoms which provide additional pseudocapacitance, as well as improving electrical conductivity and wettability, enhancing electron and ion transportation. Similarly, N-doping in hydrothermal lignin

Table 4 Electrochemical performance of carbon and composite supercapacitor electrodes obtained by HTC

Precursor	Hydrothermal conditions	Carbonisation temperature	Activation/ template	Capacitance ($F\ g^{-1}$)	Capacitance retention	Ref.
Ginkgo leaf	250 °C, 12 h	700 °C (activation)	KOH	350 at 1 A g^{-1}	98% after 30 000 cycles at 5 A g^{-1}	186
Rye straw	240 °C, 24 h	750 °C	KOH	229 at 1 A g^{-1}	—	216
Hemp stems	160 °C, 12 h	600 °C (pre-activation), 800 °C (activation)	KOH	318 at 0.1 A g^{-1}	96% after 10 000 cycles at 4 A g^{-1}	217
Jujun grass	180 °C, 10 h (ionothermal)	900 °C (activation)	KOH	336 at 1 A g^{-1}	87% after 2000 cycles at 1 A g^{-1}	218
Stem bark	130 °C, 2 h, KOH	700 °C	KOH	320 at 0.5 A g^{-1}	94% after 10 000 cycles at 2 A g^{-1}	219
Rice husk	180 °C, 10 h, NaOH	500 °C (pre-activation), 800 °C (activation)	KOH	302 at 1 A g^{-1}	89% after 5000 cycles at 10 A g^{-1}	221
Tobacco rods	200 °C, 12 h	800 °C	KOH	287 at 0.5 A g^{-1}	96% after 10 000 cycles at 5 A g^{-1}	227
Starch	200 °C, 8 h	800 °C	Ammonium ferrous sulfate $(NH_4)_2Fe(SO_4)_2$	248 at 0.5 A g^{-1}	93% after 10 000 cycles at 2 A g^{-1}	132
Lignin	200 °C, 24 h	800 °C	KOH	312 at 1 A g^{-1}	98% after 20 000 cycles at 10 A g^{-1}	220
Glucose	200 °C, 24 h	700 °C	KOH	247 at 0.2 A g^{-1}	—	222
Glucosamine	200 °C, 24 h	700 °C	KOH	250 at 0.2 A g^{-1}	—	222
Granulated sugar	200 °C, 24 h	700 °C (activation), 800 °C (H_2 reduction)	$ZnCl_2$	136 at 0.1 A g^{-1}	—	223
Lignin, graphene oxide	240 °C, 16 h	—	—	190 at 0.5 A g^{-1}	87% after 10 000 cycles at 10 A g^{-1}	228
Glucose, graphene oxide	200 °C, 16 h	800 °C	KOH	223 at 0.1 A g^{-1}	87% after 10 000 cycles at 1 A g^{-1}	229
Graphene foam, polyvinyl alcohol (PVA), polyvinylpyrrolidone (PVP)	190 °C, 12 h	800 °C	KOH	188 at 0.5 A g^{-1}	100% after 10 000 cycles at 2 A g^{-1}	230
Distillers dried grains with solubles, graphene oxide	200 °C, 18 h	600 °C (activation), then microwave for 30 s at 1200 W	KOH	102 at 1 A g^{-1}	92% after 5000 cycles at 5 A g^{-1}	231
Glutaraldehyde, $KMnO_4$	180 °C, 5 h (yeast + glutaraldehyde), 160 °C, 3 h (hollow carbon + MnO_2)	850 °C (hollow carbon)	Yeast cells	255 at 1 A g^{-1}	89% after 5000 cycles at 10 A g^{-1}	224
Carbon cloth, $Co(NO_3)_2$, Na_2MoO_2, $Ni(NO_3)_2$, $C_6H_{12}N_4$	150 °C, 6 h ($CoMoO_4$ + carbon cloth), 90 °C, 12 h (NiCo-LDH)	350 °C ($CoMoO_4$ + carbon cloth)	—	2024 at 1 A g^{-1}	91% after 5000 cycles at 1 A g^{-1}	225
$NiCl_2$, Se, graphene oxide, hydrazine	120 °C, 12 h	—	—	1280 at 1 A g^{-1}	98% after 2500 cycles at 5 A g^{-1}	226

improved conductivity and surface wettability with electrolyte ions, whilst the hierarchical bowl-like pore structure and large specific surface area (2218 $m^2\ g^{-1}$) resulted in a high specific capacitance of 312 F g^{-1} at 1 A g^{-1} and excellent cycling stability (98% after 20 000 cycles at 10 A g^{-1}, Fig. 24).[220] Even at 80 A g^{-1}, 81% capacitance was retained, likely due to the high conductivity and efficient ion transport pathways in the hierarchical pore structure.

Ginkgo leaves have been used as a precursor to sulphur-doped carbons, and highly porous carbons.[186] Following sulfuric acid-assisted HTC, and KOH activation, a carbon material with a S-content up to ~8 wt% was obtained, with a hierarchical porosity, and a specific surface area of 1132 $m^2\ g^{-1}$, higher than those of materials produced without activation or treatment with sulfuric acid. Further heating of the sample in air to remove sulphur resulted in an even higher surface area of 1757 $m^2\ g^{-1}$. In spite of the lower surface area, the S-doped material showed the best performance, achieving a specific capacitance of 364 F g^{-1} at 0.5 A g^{-1}, with an aqueous electrolyte. At a high rate of 50 A g^{-1}, the specific capacitance was

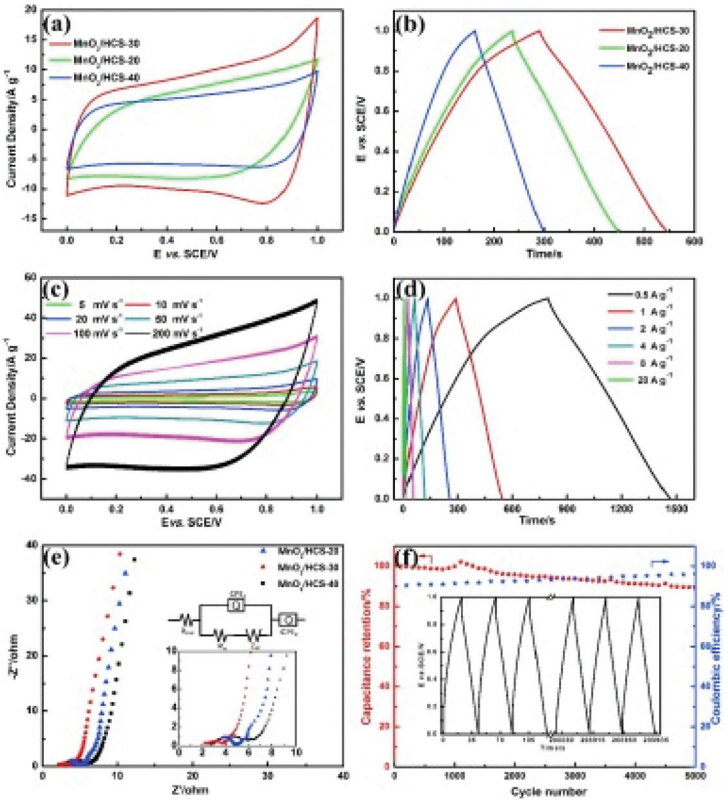

Fig. 23 The electrochemical performances of samples in a 1 M Na_2SO_4 electrolyte. (a) CV curves at a scan rate of 50 mV s^{-1}. (b) GCD curves at a current density of 1 A g^{-1}. (c) CV curves at different scan rates. (d) GCD curves at different current densities of MnO_2/HCS-30. (e) Nyquist plots of samples. (f) Cycle life and coulombic efficiency of MnO_2/HCS-30 at a current density of 10 A g^{-1}. Reproduced with permission from ref. 224.

still 230 F g^{-1} suggesting that sulphur-doping can increase the pseudocapacitance in the presence of sulfone and sulfoxide moieties and creates a more polarised surface which facilitates charge transfer. The addition of graphene derivatives to biomass precursors results in hybrid xerogel structures with varied morphologies and porosities, depending on the precursor, component ratios, and HTC or activation conditions. In one study, the addition of GO to lignin during HTC was found to modify the pore structure and increase the specific surface area, whilst lignin could effectively reduce the GO sheets under hydrothermal conditions, and prevent aggregation of rGO sheets by interrupting the π–π stacking.[228] rGO improved electrical conductivity, and provided structural stability, enabling long cycling. Similarly, xerogels of hydrothermally carbonised glucose-GO followed by KOH activation resulted in cellular structures exhibiting well-connected, continuous and very thin carbon walls (~5–15 nm) which favoured ionic diffusion and electronic conduction.[229] The thickness and connectivity of the walls could be altered by varying the amount of KOH, and it was found that the carbon xerogel with very thin, connected walls and a relatively high graphitic character (from a lower amount of KOH) delivered a much higher specific capacitance than that of a commercial activated carbon (223 *vs.* 153 F g^{-1} at 0.1 A g^{-1}) and retained 87% capacity after 10 000 cycles at 1 A g^{-1}. The performance was attributed to good conductivity and the hybrid cellular structure. In another work, graphene foam produced by CVD was used as a support for a hybrid hydrogel of polyvinyl alcohol (PVA) and polyvinylpyrrolidone (PVP).[230] KOH activation increased the surface area to 2994 m^2 g^{-1}, and a gravimetric capacitance of 188 F g^{-1} at a current density of 0.5 A g^{-1} was achieved. The hybrid also showed excellent long-term stability at a current density of 2 A g^{-1}, with no capacitance loss after 10 000 cycles. The performance can be attributed to the highly porous structure and large accessible surface area, which are stabilised by the graphene foam, and enable rapid and reversible ion transport. The presence of GO in the HTC of distillers dried grains with water-soluble chemicals changed the morphology of the particles from spheres to flakes.[231] Additional KOH activation increased the surface area, although it remained low compared to those of other activated carbons (479 m^2 g^{-1}). Short microwave irradiation reduced the GO sheets to increase the degree of carbonisation and graphitisation. The symmetric cell showed a specific capacitance of 102 F g^{-1} at 1 A g^{-1}, whilst 92% capacitance was retained after 5000 cycles at 5 A g^{-1}. The presence of GO is thought to

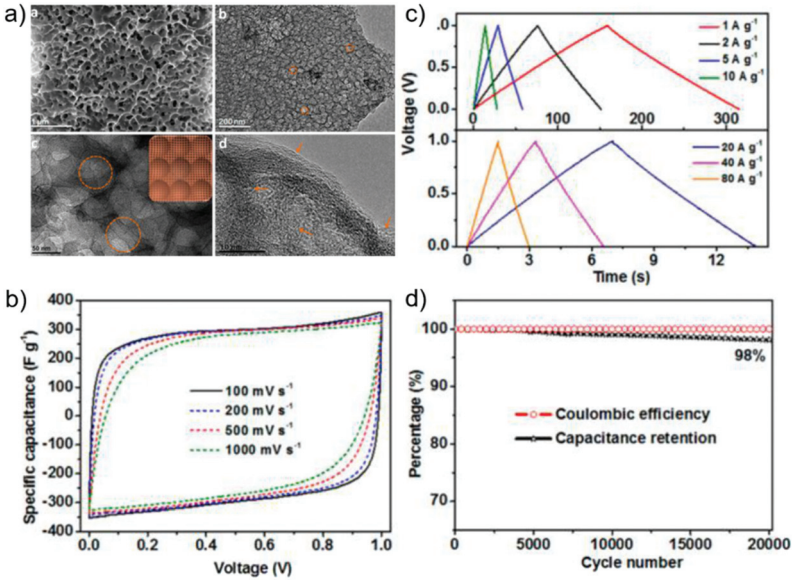

Fig. 24 (a) SEM, TEM and HR-TEM images of hierarchical porous nitrogen-doped carbon showing bowl-like pore structures. (b) CV curves, (c) charge/discharge profiles, and (d) cycling stability and coulombic efficiency at 10 A g^{-1} in a 6 M KOH electrolyte. Reproduced with permission from ref. 220.

promote biomass carbonisation and graphitisation, as well as increasing electrical conductivity.

4.2. Electrocatalysis

Electrocatalysis plays a crucial role in clean energy conversion to increase the rate, efficiency and selectivity of the chemical transformation.[232] This process involves the electrochemical conversion of water, CO_2, and N_2 into added-value products such as hydrogen, oxygenates and ammonia. Besides, the oxygen reduction reaction (ORR) plays an important role in energy conversion devices such as fuel cells and metal–air batteries. Its sluggish kinetics is a main barrier for the improvement of the overall efficiency of fuel cell devices. Currently commercial catalysts for the ORR are Pt group metals. These metals demonstrated high catalytic activity towards the ORR; nevertheless they are scarce and easy to degrade especially in an acidic electrolyte. Precious metal free nanocarbon with a heteroatom dopant are considered as promising electrocatalysts to replace the current commercial Pt group metals. The heteroatom dopants include but are not limited to non-metal atoms such as N, P, S, B, and transition metals such as Fe, Co, Ni, *etc.*[233,234] These heteroatom dopants within the carbon matrix induce heteroatom–carbon bonds and the polarization of these bonds generates active sites on the adjacent carbon matrix and results in a reduced energy barrier towards electrocatalysis, while simultaneously increasing the electrical conductivity due to the higher concentration of delocalised electrons within the π-system.[136,159,235–237]

Heteroatom doped carbon materials can be obtained from direct hydrothermal carbonisation of carbon and heteroatom precursors. A template can also be involved during the HTC process to help tune the morphology of the as-obtained products. It is worth noting that due to the limited electric conductivity of the HTC carbon, a follow-up carbonisation process is usually applied at high temperature under an inert atmosphere (usually under nitrogen or argon at above 700 °C) to further improve the electric conductivity of the carbon matrix and facilitate the assembly of heteroatom-derived active sites.[237,238] For example, nitrogen-doped carbon materials were produced using natural halloysite as a template and urea as the nitrogen source.[235] A flaky morphology was obtained with glucose as a precursor, whereas using furfural resulted in rod-like structures (Fig. 25a and b). The metal-free electrocatalysts were tested for the ORR in alkaline aqueous electrolytes, and the rod-like catalyst demonstrated a better performance than the flaky material. Considering similar amounts of N species and graphitization degrees in the as-produced samples, the superior performance of the rod-like catalysts was attributed to the higher surface area and larger pore volume which provided more active sites, a greater complexity in pore size distribution, and a rod-like morphology which facilitated electron transport. Compared to a commercial Pt/C (20 wt%) catalyst, the carbon catalysts demonstrated higher retention in diffusion limiting current density (after 3000) cycles and enhanced methanol tolerances (Fig. 25c). When tested as cathodes in a single cell H_2/O_2 anion exchange membrane fuel cell, the rod-like catalyst delivered a peak power density as high as 703 mW cm^{-2} (*vs.* 1106 mW cm^{-2} with the commercial Pt/C cathode catalyst) (Fig. 25d). Efforts have also been made to investigate doping with other heteroatoms such as boron, sulfur and phosphorus.[121,136,239] Carbogels derived from glucose and ovalbumin were produced to study the synergistic effect of boron and nitrogen and were proved to generate higher electron transfer numbers and lower hydrogen peroxide yields

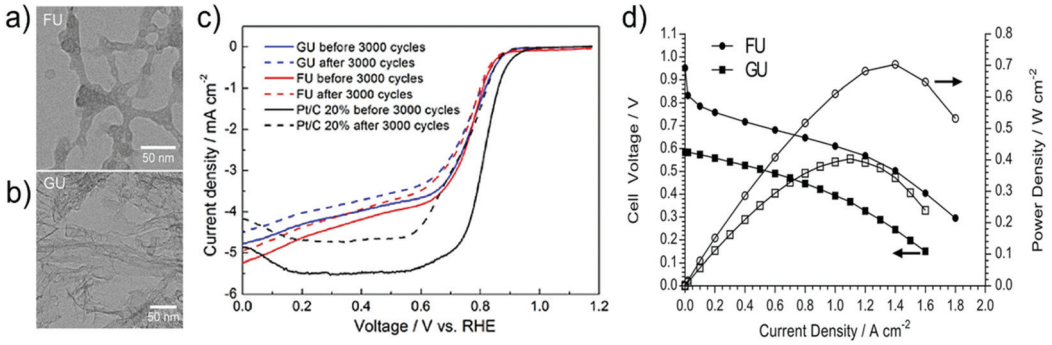

Fig. 25 STEM images of (a) FU and (b) GU in transmission electron mode. (c) The LSV curves of GU, FU and the benchmark Pt/C (20 wt%) catalysts (scan rate = 10 mV s^{-1}, rotation rate = 1600 rpm) obtained in O_2 saturated aqueous 0.1 M KOH recorded both before and after 3000 potential cycles (between 0.6 and 1.2 V). (d) Beginning-of-life H_2/O_2 anion-exchange membrane fuel cell (AEMFC) performance curves recorded at 60 °C for the GU and FU cathode catalysts (along with PtRu/C anodes): inlet gas flows were supplied with flow rates of 1 SLPM (83% relative humidity and without gas back-pressurization); reproduced with permission from ref. 235.

than those observed in purely N-doped systems. The presence of sulfur decreased the surface area and nitrogen content resulting in diminished ORR performance.[136] In contrast, a sulfur doping of 5.5 wt% in SiO_2-templated mesoporous ordered carbons was found to enhance the electrocatalytic activity in the ORR in alkaline solution, likely due to the fact that the mesoporous structure was retained from the templating method.[121] Further study on the N/B/S/P doped carbon matrix from the same research group.

SBA-15 templated carbon was doped with different heteroatom precursors at low and high concentrations (Fig. 26a), as well as a combination of nitrogen/boron, nitrogen/sulfur and nitrogen/phosphorus (Fig. 26b).[240] The correlation of material properties (surface area and surface chemistry) with the electrocatalytic activity in an alkaline electrolyte showed that the doping of N *via* the HTC method is easier than that of B or P (when comparing the yield of the dopant). N doping into the carbon matrix resulted in improved catalytic activity and electron transfer numbers, whilst the other dopants resulted in similar slightly improved performance possibly by creating defects in the carbon matrix. Despite tremendous efforts in this area, most metal-free electrocatalysts demonstrate limited catalytic activity. It is also proved that the influence of trace amounts of metal impurities on the high performance "metal-free" electrocatalysts cannot be ignored.[238] Non-precious metal dopants such as Fe, Co, and Ni, in co-existence with non-metal dopants, was demonstrated to boost the catalytic activity of the carbon electrocatalyst. These metal–N–C electrocatalysts have shown comparable catalytic activity, higher stability and tolerance toward MeOH when compared to commercial Pt–C.[241] Bifunctional nanocarbon composites can also be obtained *via* HTC by careful design of the nanocarbon matrix and active sites and tested for the ORR. 2D crystalline carbons were obtained from the HTC of glucose, fructose or cellulose with guanine, which played an important role in producing the 2D-morphology of the resultant carbon materials.[242] The porous N-doped carbons were not only found to be highly active towards the ORR but they also showed efficiency for the HER with a very low overpotential of 0.35 V to achieve 10 mA cm^{-2} in alkaline medium. In the other half of the water splitting reaction, suitable catalysts are also required for the oxygen evolution reaction; in the past, the development of fuel cells was held back due to the slow kinetics of the OER. Non-noble metal alternatives for the OER are often based on transition metal oxides, while carbon-based materials have generally been underexplored due to their relatively poor performance. Nonetheless, hydrothermally prepared transition metal dichalcogenides have also been prepared for the HER, for instance, the *in situ* hydrothermal synthesis of MoS_2/guar gum carbon hybrid nanoflowers possessed an extremely low onset potential of approximately 20 mV, a low overpotential of 125 mV at 10 mA cm^{-2} and a small Tafel slope of 34 mV dec^{-1}, nearly identical to those of the bulk platinum standard.[243] The performance was ascribed to the nanoflower architecture which provided ample active sites; furthermore, strong interactions between the MoS_2 nanoflakes and guar gum enabled long-term stability and microstructural integrity, with nearly 100% activity retention after 2000 cycles. In another study, combining $MoSe_2$ with $NiSe_2$ in composite nanowires on a carbon fibre paper skeleton resulted in better performance than either $MoSe_2$ or $NiSe_2$ alone;[244] this observation was explained by the abundance of active sites resulting from the suppression of restacking of $MoSe_2$ nanosheets, and the high conductivity of $NiSe_2$ which facilitated the transfer of electrons from the electrode to the active sites. In addition to the heteroatom dopant in the carbon matrix, the HTC approach also activates carbon cloths by creating oxygen-containing functional groups on its surface using peroxovanadium complexes, which results in a higher specific surface area and faster electron transfer rate, when compared to pristine carbon cloths.[245] The overpotential (310 mV) at 10 mA cm^{-2} of the activated carbon cloth is much lower than that of the pristine material and comparable to that of RuO_2/C (280 mV), making the carbon cloth a competitive non-metal catalyst for the OER. The HTC process is also a powerful strategy in the assembly of carbon nanostructures of various dimensions (D), with 0D, 1D and 2D nanostructures

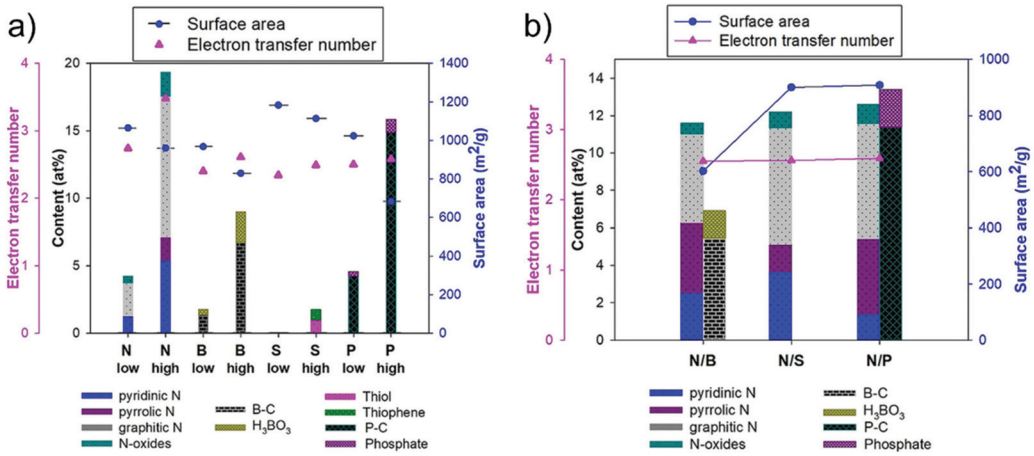

Fig. 26 Combination graph correlating the materials surface area and dopant species with the electrocatalytic activity (alkaline media) for SBA-15 templated carbons (a) doped with different heteroatom precursors in low and high concentrations. (b) Doped with nitrogen/boron, nitrogen/sulfur and nitrogen/phosphorus. Reproduced with permission from ref. 240.

being able to be assembled into higher 3D structures which possess a well developed hierarchical morphology to both facilitate mass transfer and accommodate the active sites to provide superior electrocatalytic conductivity. Highly porous and granular Ni–Co nanowires were grown hydrothermally on a woven carbon fibre fabric and then coated with a conductive shell by glucose carbonisation.[246] The structure of the nanowires greatly increased the catalytic surface area delivering an overpotential of 302 mV at a current density of 10 mA cm^{-2}. The conductive carbon layer not only facilitated electron transport throughout the entire electrode but also prevented fragmentation of the nanowires during the reaction, which translated to an overall increase of the structural integrity and hence a more reliable performance. HTC was also used to prepare 3D hierarchical structures of mesoporous SnO_2 nanosheets supported on a flexible carbon cloth, which could efficiently and selectively electrochemically reduce CO_2 to formate under aqueous conditions.[247] The electrode exhibited a partial current density of 45 mA cm^{-2} at a moderate overpotential (0.88 V) with high faradaic efficiency (87%), even larger than those of most gas diffusion electrodes. The presence of the SnO_2 particles is thought to be the reason why high performances are achieved due to the fact that they show high selectivity in the reduction of CO_2, they present a highly porous structure which provides a large surface area increasing the contact surface between the electrode and electrolyte and facilitating mass and charge transfer, and the robustness of their structure allows them to maintain the high stability of the electrocatalyst during long-term operation. Our group reported a series of graphene–HTC carbon hybrids, in which we applied graphene oxide as an electrically conductive substrate, and N-containing biomass derived HTC carbon was used to provide active sites (Fig. 27).

The sandwich structure managed to decouple the influence of electroactivity and active sites by changing the ratio of GO and HTC carbon. It has been reported that a low electrical activity limited the performance of active sites. However, when the electrical activity reached a certain level, active sites play an important role.[237] Based on this hybrid structure, we further reported a FeNC electrocatalyst using carbon nanotubes to provide electrical conductivity. The Fe residues in the carbon nanotubes coordinate with N in the hybridized HTC carbon layer to form highly efficient Fe-N based active sites while the HTC carbon layer protects the Fe–N active sites from being poisoned by the by-product and therefore highly improve the long-term stability.[158] HTC is an environmentally benign and highly efficient synthesis strategy for electrocatalyst production. However, due to the complicated mechanism during the process, the structural regulation of the well-defined active site configuration remains to be explored. Meanwhile, the HTC synthesis of single-atom catalysts would also be an interesting research direction to further improve the catalytic performance of the catalyst.

4.3. Heterogeneous catalysis

HTC derived carbon materials have been used in catalysis in many ways. On their own, they can be used as catalysts, mostly as solid acid catalysts. This is done by introducing strong Brønsted acidity mainly by the presence of sulfonated groups on the surfaces of the materials. Another widespread use of these materials is as a catalyst support. The tunability of their surface polarity and area facilitates the anchoring of metal nanoparticles, which can then be used in different reactions. Hydrothermal carbon is particularly interesting in this respect because its properties lead to a decrease in leaching of the active species when compared to classic ACs. A last and least studied use of these materials is as templates. Since hydrothermal carbon can be eliminated by combustion in air at temperatures that are not too drastic, they can be used as structure directing agents.

4.3.1. Sulfonated hydrothermal carbon catalysts. Addition of sulfonated groups to HTC synthesised carbon materials give

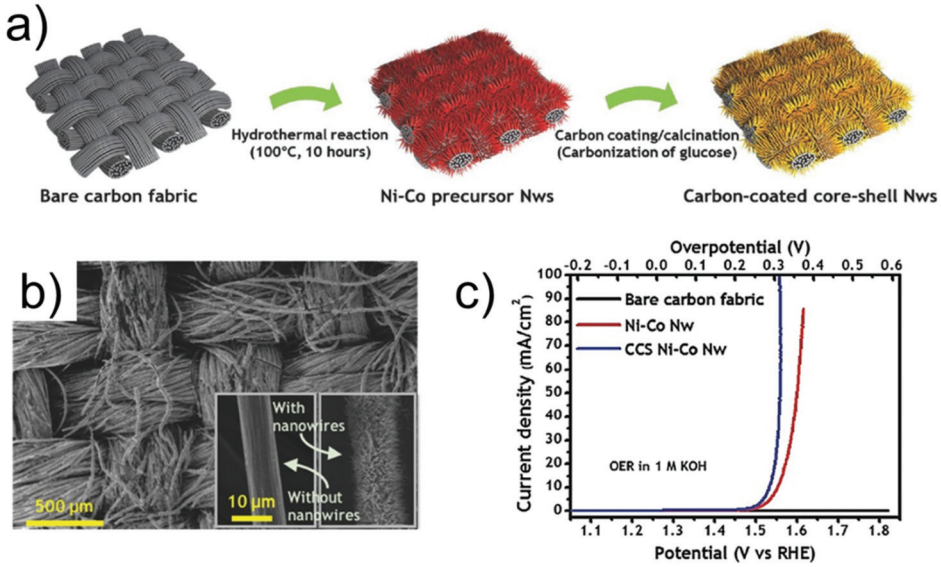

Fig. 27 (a) Schematic illustration of the fabrication procedure of 3D catalytic electrodes. (b) SEM images of CCS Ni-Co Nws on carbon fibre fabric. (c) Polarisation curves of different 3D catalytic electrodes for the OER in 1 m KOH solution; reproduced with permission from ref. 248.

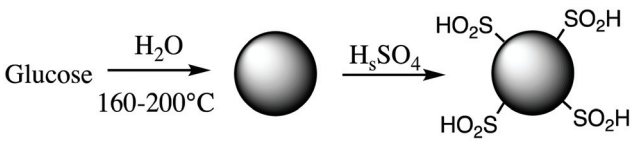

Fig. 28 Schematic view of sulfonation of porous carbon.

rise to introduction of sulfonic acid groups (Fig. 28) leading to the formation of a solid acid catalyst that can be used in catalytic reactions. These materials can be filtered and easily recovered. Such materials are generally made by treatment of porous carbon with concentrated sulphuric acid at high temperatures. Many sulfonated hydrothermal carbon catalysts have been applied in esterification reactions,[249–251] mainly in the synthesis of biodiesel.

One such case is the one prepared by Roldán *et al.*[249] After the catalyst was tested in the esterification reaction of palmitic acid with methanol, a difference in the deactivation of the catalyst was observed and this depended on the activation temperature employed for each catalyst. When temperatures lower than 500 °C were used, the deactivation of the catalyst was attributed to the formation of sulfonate esters on the surface while for those treated at higher temperatures it is speculated that accumulation of reactants and products in the pores is the main cause of deactivation. Similar catalysts were employed for the esterification of other molecules such as glycerol.[252] Glucose was used as a carbon source and the glucose solution was treated for 19 h at 195 °C leading to the preparation of a carbonaceous material which contained 67.9% C and 27.5% of oxygen. It was observed that after sulfonation (150 °C, 15 h) the carbon content decreased to 55.8% and the oxygen content increased to 40.5%. From this change in values, and taking into account the amount of sulphur added, the obvious conclusion is that additional oxygen other than that of the sulfonated groups was added during the treatment with sulphuric acid. This may occur by water addition to double bonds, hydrolysis of furan groups, or addition of ether functionalities. The sulfonated material was tested in the esterification of glycerol with acetic, butyric, and caprylic acids and the catalytic performance was compared to those of commercial sulfonated resins.[252] Turnover numbers of glycerol and acetic acid were in the same range for both the commercial and hydrothermal carbon materials. Regeneration of these acid catalysts usually involves the treatment of spent catalysts with acid, cleaving esterified sulphonic groups.[253] Pileidis *et al.*[254] also prepared such materials (HTC conditions: 230 °C, 24 h) and used them as catalysts for the esterification of levulinic acid. In this case, not only glucose but also cellulose and rice straw were used as carbon sources. These sources led to the formation of materials with 80, 76, and 70% of carbon (for glucose, cellulose and rice straw, respectively) and were then sulfonated (80 °C, 4 h) introducing 5–6% of sulphur. Esterification was carried out at 60 °C and after 3 h almost full conversion was achieved with the glucose-derived material with a 97% selectivity toward the ester. The second best performance was recorded for the material prepared from rice straw with 92% of both conversion and selectivity. With carbonised and sulfonated cellulose, 89% conversion and selectivity were observed. It is worth noting that it has been reported that sulfonation at high temperature (150 °C) induces changes in the structure of hydrothermal carbon. This is due to a decrease in the abundance of furanic groups and an increase in the presence of benzenic rings.[255] Alternative methods of sulfonation have been shown such as the direct HTC in the presence of sulfonic precursors (mainly hydroxyethylsulfonic acid).[256]

The materials prepared using this method presented very high stability and reusability, enabling future applications.

4.3.2. Pristine hydrothermal carbon as catalysts. Sulfonation is a simple method to introduce strongly acidic sites into hydrothermal carbon. However, also pristine surfaces possess catalytic properties due to the high amount of hydroxyl and carboxylic groups. This has been demonstrated in the application of such catalysts for the 5-HMF production from fructose in ionic liquids.[257] Hydrothermal carbon is produced from glucose at 180 °C in 10 h and employed after oven-drying without any further treatment. The results show that fructose was converted into 5-HMF with a maximum yield of 89% after a 90 min reaction time. The stability of these catalysts was not properly evaluated, and hence clarification would be needed; however this shows that even sulphur-free surfaces of carbon present catalytic activity in some reactions such as the dehydration of fructose. Hydrothermal carbon also permits alkaline functionalisation of surfaces and their use in catalysis.[258] As such, carbon spheres were synthesized from glucose at 160 °C maintaining the temperature for 12 h. Thereafter, acidic functionalities such as carboxylic and hydroxyl groups were neutralized with sodium hydroxide at room temperature. The sodium-hydroxide-treated hydrochar was active for the base-catalysed aldol condensation.[258] Benzaldehyde was reacted with acetaldehyde to form cinnamaldehyde. High selectivity (94%) was achieved at 34% conversion based on benzaldehyde. At this conversion, the cinnamaldehyde also started to react with acetaldehyde to produce a higher weight homolog. In comparison with sodium hydroxide solutions, the modified hydrothermal carbon is less active but more selective and can be used in three catalytic runs with the same activity. As a summary, it can be stated that hydrothermal carbon has promising potential as a metal-free catalyst for industrial applications. Introduction of strong Brønsted acid sites is achieved in a straightforward manner by sulfonation, for example, by treatment with sulphuric acid. However, the oxygen functionalities of pristine hydrothermal carbon can also be used for catalytic transformation.

4.3.3. Hydrothermal carbon as a catalyst support. ACs are classical supports for numerous catalysts found in commercial processes. This is due to their high stability and surface area. In general, activated carbons possess a high surface area of 1000–1500 $m^2\ g^{-1}$, and they are highly apolar and hydrophobic due to a low oxygen content. They, however, present a problem when used as a support for metals such as palladium and that is leaching, which greatly decreases the activity and reusability of the catalyst. In contrast, hydrothermal carbon has a polar surface and a much lower surface area. By reduction of the oxygen content and increasing that of carbon, the properties of hydrothermal carbon can become closer to those of AC.[249] By tuning these parameters (surface area and polarity), the deposition of metal precursors can be enhanced, indicating that not only can the textural properties be similar to those of ACs but they have also been reported to enhance the reuseability of the catalysts, most probably by diminishing the aggregation and leaching of the metals.[259] Hydrothermal carbons with or without further modification have been employed as carbon supports for metals.[259–263] The process in most cases is the same: a carbon source is HTC yielding a material that is activated (thermally or chemically) and is then used to support the metal precursor which is then reduced by the addition of a reducing agent ($NaBH_4$ for example), as elaborated in section 2.2.2. In some cases, the reduction step can be skipped when using pristine carbon surfaces.[264,265] Glucose-derived hydrothermal carbon supports and stabilizes the metal nanoparticles and keeps them active for prolonged time under reaction conditions. Palladium nanoparticles supported onto hydrothermal carbon were employed for the Suzuki–Miyaura coupling.[259] The material demonstrated high catalytic activity for the reaction of many aryl halides and boronic acids. It could be recycled for up to five times through simple centrifugation. In liquid state reactions, leaching of the supported metal is usually a problem but the properties of hydrothermal carbon favour the redeposition of leached particles during cooling down of the reaction. More elaborate supports can be designed by combining HTC with a porous polymer as the template as done by Cheng *at al.*[266] In this case, a polymer was introduced during the HTC process serving as a template which was then removed at 700 °C under a reducing atmosphere. This thermal treatment increased the BET surface area significantly. This material was then loaded with gold nanoparticles and tested for the hydrogenation of 4-nitrophenol to 4-aminophenol with sodium borohydride, resulting in high catalytic activity. As mentioned before, hydrochar can be treated under basic conditions neutralising any acid surface functionality. This can be interesting when using them as supports such as when loading palladium NPs and using them in oxidation reactions.[258] The absence of acid sites lowers the number of side reactions that can occur augmenting selectivity and the high dispersion of the metal allows high activities to be achieved. This high dispersion is aided by this basic pretreatment of the material as evidenced by the smaller palladium NPs observed for those samples treated with a higher concentration of basic solution (2.7 nm *versus* 7.5 nm). HTC can also be performed in the presence of metal oxide particles.[267–269] Hence, by utilising magnetic metal oxide cores a magnetically active material can be obtained. In this way, active catalysts for the Suzuki–Miyaura cross-coupling reaction have been prepared with palladium and platinum nanoparticles as active sites.[267] In this work, Fe_3O_4 particles (magnetite) were introduced during the carbonisation of glucose at 180 °C for 4 h. After this, palladium or platinum nanoparticles were deposited on the carbon shell and the whole material was protected by a further layer of approx. 35 nm thickness of mesoporous silica. Silica was added to prevent sintering of the metal nanoparticles while its porosity allowed the organic molecules tested to pass through it. The magnetite particles had a uniform diameter of approx. 180 nm composed of nanocrystals of approx. 8 nm size. The carbon shell thickness was found to be approx. 15 nm. The size of the supported palladium and platinum particles was determined by HRTEM and mean diameters of 14 and 25 nm were obtained, respectively.

The hydrophilic surface of the hydrothermal carbon facilitated dispersion of the particles in water during the mesoporous silica synthesis and allowed a regular coverage of the particles.

4.3.4. Hydrothermal carbon as a sacrificial component. The defined structure and geometry of the spheres synthesised from HTC can be used as a template since it can be easily removed with thermal treatment in air at about 500 °C.[270–272] With this in mind, very effective catalysts for the low temperature oxidation of CO were produced.[270] In his work, Zhao *et al.*[270] produced gold nanoparticles by bringing in contact the gold precursor and glucose in water (Fig. 29). Glucose plays two main roles in this synthesis: it acts as a reducing agent and it is also a carbon source for generating the hydrothermal carbon. Once the gold nanoparticles were formed, the cerium precursor was added, and the mixture was heated to 180 °C for different periods of time (1, 6, 10, and 20 h). Afterwards, the solid was collected and calcined at different temperatures in a range of 300–600 °C for 6 h, eliminating all hydrothermal carbon.

TEM images (of the calcined samples) showed gold nanoparticles of an average size of 11 nm after 1 h of HTC and the whole diameter of the core–shell structure was about 40 nm. When the HTC was prolonged to 10 h, the gold nanoparticles grew to 16 nm and the shells to 103 nm. The best catalytic performance in carbon monoxide oxidation was shown by the material that was subjected to HTC for 10 h and was calcined subsequently at 600 °C. This catalyst allowed the reduction of the reaction temperature from 300 to 155 °C for full conversion and it was tested on stream for 70 h without any deactivation being evident. In a similar way, cobalt nanoparticles protected within hollow mesoporous silica spheres were synthesized[271] starting from hydrothermal carbon spheres with an approximate diameter of 100–150 nm synthesised from glucose carbonised at 180 °C for 4.5 h. After impregnation with cobalt nitrate providing nanoparticles of approx. 4 nm and the synthesis of a mesoporous silica shell (thickness: approx. 20 nm) with CTAB as a soft template, all the organic material was removed by calcination at 430 °C. This synthesis procedure provided a catalytic material with interesting performance in the epoxidation of alkenes. When the cobalt/silica hollow spheres were employed in the epoxidation of styrene with oxygen, a 94% selectivity toward the epoxide was achieved at almost complete conversion (Table 5).

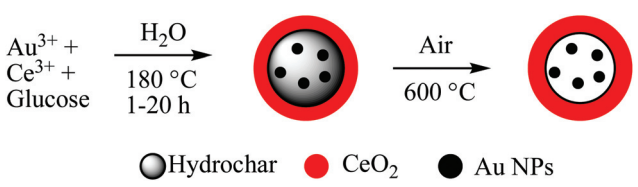

Fig. 29 Schematic representation of the synthesis of core–shell distribution of gold particles and cerium oxide.

4.4. Gas storage

The porous carbon materials, obtained *via* HTC combined with templating/activation techniques, have been intensively used for gas capture and separation. Different gases such as CO_2,[83,98,273–275] H_2,[135] SO_2,[82] H_2S and CH_4,[276,277] have a good affinity for the carbon structure, which make the ACs an obvious choice, over the classical gas separation methodologies.[278]

4.4.1. CO_2 adsorption. CO_2 is commonly discussed as a greenhouse gas and the main cause of global warming. As such, many research studies have been focused on the synthesis of porous carbon materials for CO_2 adsorption. In a recent work, Rao *et al.*[279] reported high CO_2 uptake for carbon adsorbents derived from glucose and decorated with nitrogen. The authors described different variations of the adsorption capacity depending on several parameters. In this way, they observed that the CO_2 uptake increases on raising the carbonisation temperature from 600 °C to 650 °C, but a further increase affects negatively the adsorption process. During the study, they reported the maximum CO_2 adsorption capability of 4.26 mmol g^{-1} and 6.70 mmol g^{-1} at 25 °C and 1 bar (RTP), and in contrast to other studies which correlate the adsorption properties with the volume of narrow micropores, the authors reported that the best performing samples in their own work possessed medium values of the narrow micropore volume, and their good performance is mainly correlated with the synthesis procedure. Zhu *et al.*[126] synthesised porous carbon adsorbents *via* the HTC of pineapple waste. The resulting hydrothermal carbon was further activated, with $Li_2C_2O_4$, $Na_2C_2O_4$ and $K_2C_2O_4$, in order to develop the porosity and enhance the CO_2 uptake. The maximum CO_2 adsorption capacity values were 5.32 mmol g^{-1} at 0 °C and 1 bar (STP) and 4.25 mmol g^{-1} in RTP, and it was observed for the carbon activated with $K_2C_2O_4$, being correlated with the high volume of narrow micropores, about 0.92 cm^3 g^{-1}. Sevilla *et al.*[135] reported important adsorption capacities for CO_2 using porous carbon materials derived from three different biomass sources: starch, cellulose and sawdust, by means of HTC and chemical activation. The high surface areas (2690–3540 m^2 g^{-1}) combined with bimodal porosity in the micromesopore range led to high CO_2 adsorption capacities, such as 20–21 mmol g^{-1}, at 20 bar and 25 °C. By extending the pressure range, up to 40 bars, the CO_2 uptake was increased to 30–31 mmol g^{-1}. Xiao *et al.*[96] reported adsorption capacities for CO_2 of about 4.7 mmol g^{-1} in STP, using nitrogen-doped carbon materials obtained from glucosamine *via* the HTC–soft templating approach. CO_2 adsorption was performed also by Boyjoo *et al.*,[98] who reported an adsorption capacity of about 5.22 mmol g^{-1} in RTP, using activated hydrothermal carbon produced from Coca-Cola waste as adsorbents. The value was even higher in STP, reaching 6.27 mmol g^{-1}. In their study, they prepared three activated carbons, starting from the same biomass precursor and changing either the mass ratio between the activator and hydrothermal carbon or the activation agent (activation with $ZnCl_2$, denoted as CMC_1 and CMC_2; mass ratio of $ZnCl_2$/HTC carbon = 1 and 3, respectively, and KOH,

Table 5 Catalytic materials prepared through HTC compiled from the literature

Sample name	Carbon precursor	Carbonisation conditions	Role of carbon material	Reaction tested	Reaction conditions	Product obtained	Conversion (%)	Selectivity (%)	Ref.
HTC_673_SO_3H	Glucose	673 K, N_2 atmosphere, H_2SO_4, 473 K, Ar atmosphere	Heterogeneous catalyst	Esterification of palmitic acid with methanol	Reflux, 85 °C, 4 h	Methyl palmitate	90	—	249
SHTC	Glucose	HTC 195 °C, 19 h, H_2SO_4, 150 °C, 15 h	Heterogeneous catalyst	Esterification of glycerol with acetic acid	115 °C, 10 h, 9 : 1 AcOH/gly	Monoacetin Diacetin Triacetin	98	5 38 57	252
SHTC	Glucose	HTC 195 °C, 19 h, H_2SO_4, 150 °C, 15 h	Heterogeneous catalyst	Esterification of glycerol with butyric acid	115 °C, 10 h, 9 : 1 Butyric OH/gly	Monoacetin Diacetin Triacetin	99	1 24 75	252
SHTC	Glucose	HTC 195 °C, 19 h, H_2SO_4, 150 °C, 15 h	Heterogeneous catalyst	Esterification of glycerol with caprylic acid	115 °C, 10 h, 9 : 1 Caprylic OH/gly	Monoacetin Diacetin Triacetin	98	2 42 56	252
HTC_Glu_S	Glucose	HTC 240 °C, 24 h, H_2SO_4, 80 °C, 4 h	Heterogeneous catalyst	Esterification of levulinic acid with ethanol	60 °C, 3 h	Ethyl levulinate	97	97	254
HTC_Cell_S	Cellulose	HTC 240 °C, 24 h, H_2SO_4, 80 °C, 4 h	Heterogeneous catalyst	Esterification of levulinic acid with ethanol	60 °C, 3 h	Ethyl levulinate	89	88.9	254
HTC_RS_S	Rye straw	HTC 240 °C, 24 h, H_2SO_4, 80 °C, 4 h	Heterogeneous catalyst	Esterification of levulinic acid with ethanol	60 °C, 3 h	Ethyl levulinate	92.2	92.2	254
Carbon microspheres	Glucose	HTC 180 °C, 10 h	Heterogeneous catalyst	Dehydration of fructose	100 °C, 90 min, [BMIM][Cl] ionic liquid,	5-HMF	89	100	257
CNS_3OH	Glucose	160 °C, 12 h, 3 M NaOH solution, RT, 1h	Heterogeneous catalyst	Aldol condensation of benzaldehyde and acetaldehyde	40 °C, 5h	*Cis*- and *trans*-cinnamaldehyde *Cis*- and *trans*-5-phenyl-2,4-pentadienal *Cis*- and *trans*-7-phenyl-2,4, 6-heptatrienal	33.9	94 6 0	258
Pd@UCS	Sucrose	180 °C, 8 h, kayexalate, activated in air, 800 °C, 1h	Catalyst support for Pd NPs	Suzuki coupling reaction	50 °C, 1 h	Coupling product of bromobenzene and phenylboronic acid	99	—	259
Au-5/C	Glucose	180 °C, 24 h, modified polymer template, carbonised in 5% H_2 with a heat ramp to 700 °C for 5 h	Catalyst support for Au NPs	Hydrogenation of 4-nitrophenol	RT, 180s	4-Aminophenol	100	—	266
$Fe3O_4$@C-Pd@$mSiO_2$	Glucose	180 °C, 4 h	Layer over Fe_3O_4 and support for Pd NPs	Suzuki–Miyaura crosscoupling reaction	70 °C, 6 h	Coupling product of phenylboronic acid and *p*-iodoacetophenone	99	—	267
20 h-600 °C-Au@CeO_2	Glucose	180 °C, 20 h, $HAuCl_4$, $CeCl_3$ and $CO(NH_2)_2$, calcined at 600 °C, 6 h	Sacrificial component	Low temperature CO oxidation	From RT to 300 °C at 1 °C min^{-1}	—	100	—	270
Co/HSM	Glucose	180 °C, 4.5 h, calcined at 400 °C in air for 7 h	Sacrificial component	Epoxidation of styrene with molecular oxygen	100 °C, 3 h, bubbling with O_2 at atmospheric pressure in DMF	Styrene oxide	98	94	271
Co/HSM	Glucose	180 °C, 4.5 h, calcined at 400 °C in air for 7 h	Sacrificial component	Epoxidation of dec-1-en with molecular oxygen	110 °C, 3 h, bubbling with O_2 at atmospheric pressure in DMF	Dec-1-en oxide	93	93	271

denoted as CMC_3 KOH/HTC carbon = 4). The adsorption capacities were approximately 4.8 mmol g^{-1} for $ZnCl_2$ activated samples and 6.27 mmol g^{-1} for the KOH activated sample, with values reported in STP. More examples of carbonaceous materials derived from biomass resources and used in CO_2 adsorption applications are listed in Table 6.

4.4.2. H_2, CH_4 and H_2S adsorption. Correa *et al.*[133] conducted a comparative study of the adsorption properties of activated carbons produced from giant bamboo *via* HTC and pyrolysis, followed by chemical activation with KOH. The materials were tested for H_2 adsorption at −196 °C and 1 bar. The results showed that the best H_2 uptake was registered for the carbon material synthesised *via* HTC, followed by KOH activation, with 3.2 wt% corresponding to 16 mmol g^{-1}. Sevilla *et al.*[135] reported high adsorption capacities for H_2. At −196 °C and 20 bar the total H_2 uptake of biomass derived carbons was in between 6.4 and 6.8 wt%, equivalent to 32–34 mmol g^{-1}. H_2 adsorption has been studied by Xiao *et al.*[96] using soft templating-HTC carbon adsorbents. The maximum H_2 uptake was 9 mmol g^{-1} under the same adsorption conditions as those used by Correa *et al.*[133] The difference may be assigned to the textural properties, as the materials synthesised by Correa[133] present a higher surface area, pore volume and micropore volume (S_{BET} = 2117 m^2 g^{-1}; V_{total} = 1.14 cm^3 g^{-1}; and V_n = 0.49 cm^3 g^{-1}) when compared to the carbons reported by Xiao[96] (S_{BET} = 980 m^2 g^{-1}; V_{total} = 0.78 cm^3 g^{-1}; and V_n = 0.46 cm^3 g^{-1}). It is worth noting that the synthesis methods are different; while Correa[133] used HTC and chemical activation, Xiao[96] reported HTC-soft templating. CH_4 adsorption, at high pressure and ambient temperature, for activated nanocarbon produced by microwave-assisted HTC, was measured by Cruz *et al.*[131] They found that CH_4 uptake increases with pressure, up to a maximum of 8 wt% at 40 bars. Shang *et al.*[280] studied the adsorption of H_2S on biochars derived from agricultural and forestry waste, such as camphor tree, rice hull and bamboo. The maximum H_2S uptake was about 11.25 mmol g^{-1} for the biochar derived from rice hull having the highest specific surface area (115 m^2 g^{-1}) and the highest carbon content. Sethupathi *et al.*[276] used biochars as potential absorbents of methane, carbon dioxide and hydrogen sulphide. They investigated four types of optimized biochars derived from perilla leaf, soybean Stover, Korean oak and Japanese oak. When adsorbed in tandem, CO_2 and H_2S compete for the adsorption sites, resulting in low adsorption capacity of the material. To confirm the competition phenomenon, the authors conducted a single-gas study of CO_2, H_2S and CH_4. During the measurement it was observed that all the biochars showed a longer H_2S adsorption breakthrough time when compared to a simultaneous study, and a single-gas adsorption measurement for CO_2 revealed about 6.6 mmol g^{-1} adsorption capacity, significantly higher than the adsorption capacity obtained during the simultaneous tests. It was also observed that all biochars showed a higher preference for H_2S over CO_2. This is because CO_2 is generally captured *via* physisorption, while H_2S adsorption depends on both physisorption and local pH within the pores.

4.5. Water treatment

Water contamination with organic pollutants or heavy metals attracted significant attention because of their high toxicity and non-degradability.[281] Among their applications, porous carbon materials derived from sustainable resources represent a green and effective method to adsorb water pollutants. Several studies reported their ability to take up both organic[85,168,282–284] and inorganic molecules.[285–290]

4.5.1. Removal of organic pollutants. Roldán *et al.*[168] used mesoporous carbon doped with N and S, prepared *via* a one-pot HTC, for water treatment, for the adsorption of two dyes: methylene blue (1.43 nm × 0.61 nm × 0.4 nm) and Rhodamine B (1.59 nm × 1.18 nm × 0.56 nm). They observed that as a general trend the adsorption capacity was larger for methylene blue, in contrast to the other dye, which may be mainly due to size-based reasons, the second one being slightly larger. Both molecules are cationic; so the interaction with the support does not significantly vary. Also, both materials perform better before pyrolysis, explained by the higher oxygen functional group content and lower graphitization degree which offer a more hydrophilic surface enhancing the electrostatic interactions with the dyes. In this case, the presence of the dopant greatly enhances the adsorption properties by creating different pore sizes in the material. The adsorption capacities were about 106 mg g^{-1} for rhodamine B and 123 mg g^{-1} for methylene blue, on S-doped porous carbon activated with $ZnCl_2$, with a surface area of 288 m^2 g^{-1} and a pore volume of 0.56 cm^3 g^{-1}. Alatalo *et al.*[169] proposed methylene blue removal from aqueous media using meso-microporous soft templated carbons prepared *via* a HTC–salt templating method. The materials were derived from fructose and activated with mixtures of $LiCl/ZnCl_2$ in a one-pot HTC at 180 °C. Two types of materials were prepared, one from pure fructose (FruLi) containing surface polar oxygenated functionalities and a second one from fructose and 2-thiophenecarboxyaldehyde (TCA), resulting in thiophenic sulphur doped within the final carbon network (FruLi+TCA). The adsorption experiments of methylene blue for both carbon materials were performed in the pH range of 3–8, but a minor effect was observed. The influence of temperature was also studied, in the range 20–60 °C. During these measurements it was observed that the adsorption efficiency increased slightly when the temperature was increased from 20 to 40 °C, maybe due to decreased solution viscosity leading to an enhanced diffusion rate of adsorptive molecules across the external boundary layer and in the internal pores.[282] At equilibrium (pH 6 at 20 °C with a 24 h contact time) the maximum adsorption capacity was approximately 96 mg g^{-1} for FruLi and 64 mg g^{-1} for FruLi+TCA. In a recent study, Correa *et al.*[133] reported very high adsorption capacity for methylene blue, about 735 mg g^{-1} using activated carbon prepared from different chars. Xiong *et al.*[284] used a carbon-silicate composite, synthesised by HTC, for methylene blue removal. The maximum adsorption capacity was 418 mg g^{-1}, considerably higher than that obtained for the unmodified hydrothermal carbon.

Table 6 CO_2 uptake on porous carbons obtained *via* HTC

Sample name	Carbon precursor	Carbonisation conditions	Activation method	S_{BET} ($m^2\ g^{-1}$)	V_{total} ($cm^3\ g^{-1}$)	V_{micro} ($cm^3\ g^{-1}$)	$V_{narrow\ micro}$[b] ($cm^3\ g^{-1}$)	CO_2 uptake (mmol g^{-1}) 0 °C, 1 bar	CO_2 uptake (mmol g^{-1}) 25 °C, 1 bar	Ref.
GN-600-1	Glucose and urea	600 °C, N_2 atmosphere	KOH	821	0.42	0.29[a]	0.46	5.33	3.99	279
GN-650-1	Glucose and urea	650 °C, N_2 atmosphere	KOH	1734	0.78	0.62[a]	0.77	6.70	4.26	279
GN-700-1	Glucose and urea	700 °C, N_2 atmosphere	KOH	2394	1.13	0.93[a]	0.87	6.46	3.92	279
C-K-500	Pineapple waste	500 °C, N_2 atmosphere	$K_2C_2O_4$	422	0.04	—	0.82	2.71	2.22	126
C-K-600	Pineapple waste	600 °C, N_2 atmosphere	$K_2C_2O_4$	644	0.05	—	0.91	3.82	3.16	126
C-K-700	Pineapple waste	700 °C, N_2 atmosphere	$K_2C_2O_4$	1076	0.08	—	0.92	5.32	4.25	126
AA-0	Potato starch	800 °C, N_2 atmosphere	KOH	3000	1.41	1.09[c]	—	—	2.80	135
AA-3M	Potato starch	800 °C, N_2 atmosphere	KOH and melamine	3220	2.37	1.07[c]	—	—	2.50	135
AC-0	Cellulose	800 °C, N_2 atmosphere	KOH	3100	1.46	1.05[c]	—	—	2.80	135
AC-2M	Cellulose	800 °C, N_2 atmosphere	KOH and melamine	3540	2.22	1.28[c]	—	—	2.30	135
AS-2M	Sawdust	800 °C, N_2 atmosphere	KOH and melamine	3420	2.30	1.16[c]	—	—	2.20	135
CMC-3	Coca Cola waste	High T°C, inert atmosphere	KOH	1405	0.80	0.05[d]	0.45[e]	6.27	5.20	98
CMC-2	Coca Cola waste	High T°C, inert atmosphere	$ZnCl_2$	1994	0.87	0.51[d]	0.26[e]	4.84	3.00	98
HPNC-3	Glucosamine	600 °C, N_2 atmosphere	Pluronic P123 templated	710	0.54	0.37[d]	0.32[e]	4.20	—	96
HPNC-4	Glucosamine	600 °C, N_2 atmosphere	Pluronic P123 templated	980	0.78	0.46[d]	0.40[e]	4.70	—	96

[a] Calculated from the t-plot method. [b] Pore volume of narrow micropores (<1 nm) obtained from CO_2 adsorption in STP. [c] Micropore volume determined by the DR method. [d] Micropore volume calculated from the pores <2 nm based on the NLDFT method. [e] Ultramicropore volume calculated for the pores <0.7 nm based on the NLDFT method.

4.5.2. Metal recycling. Porous carbon materials prepared *via* HTC received recognition also for their ability to adsorb and recycle heavy metals from aqueous solutions.[281,285,286,291] Sun *et al.*[286] reported the synthesis of KOH ACs, starting from different feedstocks (sawdust, wheat straw, and corn stalk), for the removal of Cd(II) and multiple metals (Pb(II), Cu(II) and Zn (II)) from water. The materials have been prepared *via* HTC at 200 °C for 20 h and have been denoted as H_SD (sawdust), H_WS (wheat straw) and H_CS (corn stalk). After HTC, a part of the obtained amount was modified with KOH, being denoted as mH_SD, mH_WS and mH_CS. The characterisation results showed that the hydrothermal carbon had a high content of C, together with N, O and H. In terms of porosity, the powders possessed surface areas between 4.4 and 9 $m^2\ g^{-1}$. Both hydrothermal carbon samples, KOH modified and unmodified, were tested for Cd(II) adsorption. The samples needed about 2 h to reach the apparent equilibrium. Cd(II) was more readily removed by the KOH ACs, about 80%, compared to less than 10% for the pure hydrothermal carbons. When used to separate multiple heavy metals, hydrothermal carbons and ACs adsorb the metals in the following order: Pb(II) > Cu (II) > Cd(II) > Zn(II), which coincides with the reverse order of their hydrated ionic radius. Overall, the KOH ACs were much better adsorbents for the heavy metals, compared to the pure ones, probably due to the increased binding sites associated with oxygen-containing functional groups. When tested in the multi-metal experiment, Cd(II) sorption capacities on mHCs were only 4.12–4.73 mg g^{-1}, much lower than that in a single-metal system (30.40–40.78 mg g^{-1}), which is a clear indication of the competition for surface adsorption. Han *et al.*[288] investigated the properties of hydrothermal carbon as sorbents for Cd(II), as well. The adsorbents have been prepared *via* HTC from swine solids and poultry litter, characterized and used for Cd(II) and Sb(III). The maximum adsorption capacities for Cd(II) were 19.80 mg g^{-1} for the poultry litter hydrothermal carbon and 27.18 mg g^{-1} for the swine solids. The uptake for Sb(III) was considerably lower, with a maximum of 3.98 mg g^{-1} for the swine solid derived hydrothermal carbon. A recent study regarding Cd(II) removal from aqueous solutions was conducted by Xiong *et al.*[284] Here, the authors proposed the HTC synthesis of a silicate-carbon composite as an efficient adsorbent for Cd(II) and methylene blue. The maximum Cd(II) uptake, after a 60 minute equilibration time was 108 mg g^{-1} for the composite materials, which was higher than that

obtained for pure hydrothermal carbon (34.62 mg g^{-1}) or for magnesium silicate (70.42 mg g^{-1}), the precursor used during the synthesis. Cai *et al.*[287] reported the removal of uranium(VI) from aqueous solutions using carbonaceous spheres derived from glucose *via* HTC. In a typical adsorption experiment 10 mg of carbon powder was dispersed in 20 mL of different concentrations of U(VI) solutions (20–140 mg L^{-1}), and the mixtures were stirred at room temperature at different pH values and different times. The U(VI) uptake was determined by the difference in the solution concentrations obtained from UV-VIS measurements. During the study, it was observed that the pH plays a crucial role in U(VI) adsorption. In this way, the amount of uranium adsorbed on the carbon spheres registered a sharp increase from pH 1.5 to 3.5, then becoming constant at this value. The maximum uranium uptake was 163 mg g^{-1}, obtained at pH 4.5. The process is influenced by the pH because at low pH values the functional groups from the microsphere's surface were protonated, creating positive charges, followed by electrostatic repulsion between the positive charge existing on the surface and the uranyl ions, decreasing the adsorption capacity. Also, the competition between H^+ and uranyl ions for the active sites at low pH results in poor U(VI) uptake. The contact time was tested as well. In the first 9 h, the uranium uptake increased rapidly, followed by a small variation reaching the maximum adsorption capacity of 163 mg g^{-1} at a contact time of 22 h. When the uranium concentration increases from 20 to 80 mg L^{-1}, the adsorption capacity registers a sharp increase, followed by a slow increment beyond 80 mg L^{-1}, due to the saturation of active sites onto the surface of the HTC microspheres. A similar study has been reported by Zheng *et al.*[291] who used glucose HTC carbon spheres functionalized with 4-aminoacetophenone oxime groups for the adsorption of uranyl ions. Following a similar strategy, they obtained the maximum adsorption capacity at pH 6, followed by a decrease, due to the formation of hydroxide products of UO_2^{2+}, such as $UO_2(OH)^{3-}$ and $(UO_2)_3(OH)_7^-$, which generate electrostatic repulsion between these anions and the adsorbents. Also, at an optimum pH = 6, the amount of uranium adsorbed was significantly improved from 55.7 ± 1.5 to 366.8 ± 16.0 mg g^{-1}, after functionalization with 4-aminoacetophenone oxime groups. The maximum adsorption capacity obtained in this study for uranyl ions was 588.2 mg g^{-1} at pH 6 and 60-minute contact time, for the functionalized carbon spheres. Other studies dealing with the adsorptive removal of uranium using hydrothermal carbon have been reported by Yu *et al.*,[285] Deng *et al.*,[292] and Han *et al.*[290]

4.6 Bioenergy source–bioenergy potential in hydrothermal carbon

The solid (hydrothermal carbon) and liquid products resulting from the carbonisation of biomass have significant bioenergy potential, which has resulted in numerous studies investigating the use of hydrothermal carbon and/or the process water as fuel sources.[72,293,294] Hydrothermal carbons generated from biomass have been reported to have high energy densities (up to 35 MJ kg^{-1} dry hydrothermal carbon) and structures similar to coal, making them candidates for replacing and/or supplementing fossil fuel-derived energy.[37,295–297] Several studies have reported that hydrothermal carbonisation improves the fuel characteristics (*e.g.*, aromaticity) of biowaste, making them more comparable to lignite and bituminous coals.[298] Hydrothermal carbon energy content data collected from the literature are summarized in Fig. 30. The results indicate that, on average, hydrothermal carbons generated from the carbonisation of food waste and animal feeds result in the largest energy contents, while the hydrothermal carbon generated from the carbonisation of sludge results in the lowest energy content. Several studies reported that the hydrothermal carbon energy content increases with increasing reaction severity.[18,71,76,299–301] It is possible that the high average energy content data associated with hydrothermal carbon generated from animal feed is skewed by process conditions, since the conditions associated with the carbonisation of this feedstock resulted in the highest average severity factor. However, no defined trends associated with the severity factor appear to be present in these data.

It is important to note that both the hydrothermal carbon energy content and hydrothermal carbon yield (*e.g.*, hydrothermal carbon mass) are important when determining the total energy that can be recovered from hydrothermal carbon. Results from previously conducted studies detailed in the literature indicate that the hydrothermal carbon energy content

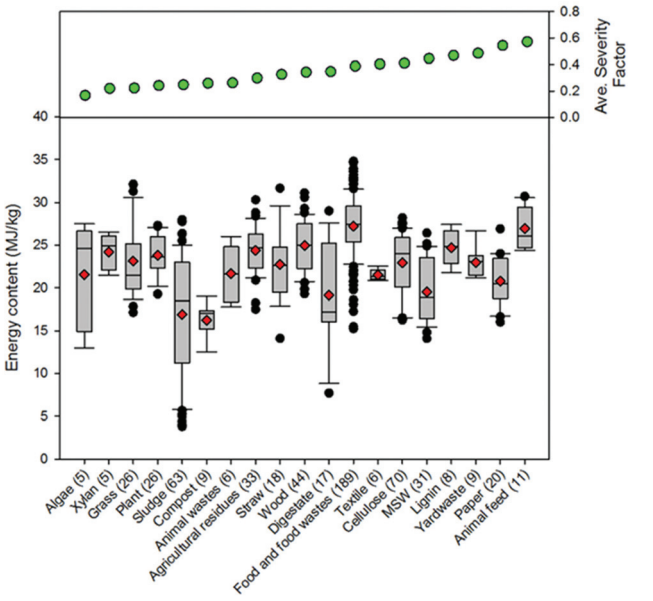

Fig. 30 Distributions associated with the hydrothermal carbon energy content of different feedstocks based on literature-collected data. The line in each box represents the median value. The ends of each box represent the 25th and 75th percentiles associated with the data. The red diamonds represent the average values. The lines and data points represent the scatter of data beyond the 10th and 90th percentiles. The numbers in parentheses following each feedstock category represent the number of data points represented on the plot.

generally increases with increasing reaction temperature and, in a way, reaction time.[17,61,69,71,302–305] Conversely, an increase in temperature and to some degree time generally result in a reduction in hydrothermal carbon generation.[8,68,69,71,76,306,307] Therefore, understanding the combined effect of these hydrothermal carbon properties is needed when determining the value of using hydrothermal carbon as a bioenergy source. Combining statistical models for predicting hydrothermal carbon yields and energy contents based on literature-collected data,[308] the total energy that may be recovered from different organic waste materials (at a constant reaction temperature, time, and initial solid concentration) can be calculated. Results from this analysis are shown in Fig. 31. In this plot, the feedstocks are listed in order of the lowest carbon content to the greatest carbon content, indicating that there is a relationship between the feedstock carbon content and the total energy that is available for use in the generated hydrothermal carbon. Blending of hydrothermal carbon with coal has been reported to improve the combustion efficiency of low rank coals for energy generation.[309–312] Gao *et al.*[313] reported that the presence of a secondary char deposited on the hydrothermal carbon surface is responsible for the high oxidative reactivity of the hydrothermal carbon. The generation of this secondary char (tar-like deposits on the hydrothermal carbon surface) has been reported to increase with the reaction severity (*e.g.*, increase in reaction time and temperature). Gao *et al.*[313] indicate that blending of hydrothermal carbons up to 10% with bituminous coal is possible and does not lead to fuel segregation (*e.g.*, uneven burning) during combustion.

4.7. Catalytic conversions of hydrothermal carbon

Hydrothermal carbons are inevitable byproducts from acid-catalyzed conversions of C5 and C6 sugars to important bio-based chemicals such as furfural, 5-hydroxymethylfurfural and levulinic acid. Valorisation of these highly condensed polymeric hydrothermal carbons[48,314,315] by catalytic conversions is of high interest but has received limited attention to date. This chapter gives an overview of the research carried out on the catalytic conversion of hydrothermal carbons to liquid products to be used as biofuels or, after fractionation, as a source of valuable biobased chemicals such as alkylphenolics and aromatics. The emphasis will be on four technologies, *viz*. (i) catalytic hydrotreatments with molecular hydrogen or hydrogen donors such as isoporopanol or formic acid, (ii) catalytic pyrolysis, (iii) aqueous phase reforming and (iv) gasification.

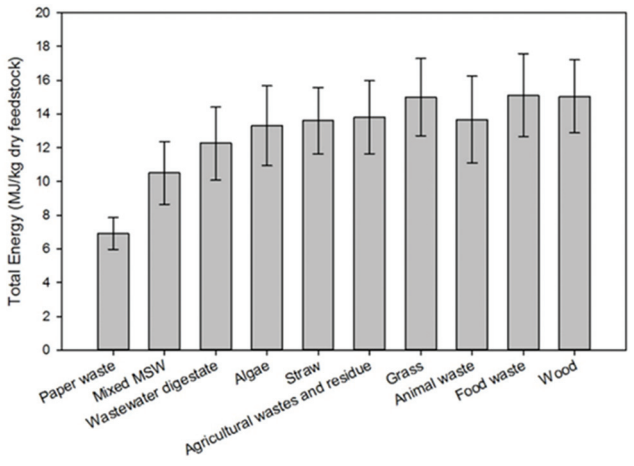

Fig. 31 Calculated total energy recoverable from different organic waste materials. Note that the waste materials are listed in order of their carbon content, ranging from the lowest value (left) to the greatest value (right). Each value represents the average value obtained from different model combinations. The error bars represent the standard deviations associated with these data.

4.7.1. Catalytic hydrotreatment. Catalytic hydrotreatment involves bringing in contact the hydrothermal carbons with molecular hydrogen (or a hydrogen donor such as formic acid (FA)) in the presence of a catalyst. This methodology has been explored in detail for the depolymerisation of lignin to low molecular weight chemicals.[316] Typical catalysts for lignin conversions are heterogeneous metal supported catalysts such as NiMo and CoMo on various supports.[317,318] Relatively harsh conditions (temperatures up to 450 °C, pressures up to 200 bar) are required for substantial depolymerisation activity. The use of hydrogen donor solvents in both the presence and absence of metal catalysts has been reported. A well-known hydrogen donor is FA, which is *in situ*, either thermally or catalytically, converted to hydrogen and CO/CO_2. Other solvents, either for dilution or to act as a hydrogen donor, are alcohols (ethanol, methanol, and isopropanol (IPA)), and water. Temperatures between 300 °C and 450 °C have been explored for lignin, with reaction times ranging from 2 to 17 h. However, in contrast to lignin, only a limited number of liquefaction studies on hydrothermal carbon using a catalytic hydrotreatment strategy have been reported. Trautmann *et al.*[319] performed research on a catalytic treatment of hydrothermal carbon, referred to as biocoals in their research, obtained by HTC of various biomass sources (green waste, straw, bark, pine wood meal and wood) and horse or swine manure with the objective to obtain a liquid product with potential to be used as a biofuel. Various biocoals were tested using Ni on titania as the catalyst at a temperature of 400 °C using molecular hydrogen (100 bar) and tetralin as the hydrogen donors (batch, 2 h reaction time). Oil yields of about 32–36 wt% have been reported, the major by-product being gas-phase components (45–58 wt%). The product oils were shown to contain limited amounts of bound oxygen (<5 wt%), and a H/C molar ratio of about 1.3. The higher heating value (HHV) of the oils was > 40 MJ kg^{-1} oil. Subsequent studies[320] were aimed at minimizing the formation of gas-phase components by lowering the liquefaction temperature from 400 to 350 °C and reducing the batch time from 2 to 1 h. Indeed, the gas yield dramatically decreased from 45–58 wt% to 14 wt%, while the product-oil yield was nearly similar. These findings suggest that liquefaction of hydrothermal carbon to oils by a catalytic hydrotreatment is feasible. Wang *et al.*[321] reported an extensive catalyst screening study using various (noble) metals (Pt, Ru, Ni, and Rh) on a range of supports (C, Al_2O_3, TiO_2,

ZrO_2, and CeO_2) for the reactive liquefaction of hydrothermal carbon in isopropanol (IPA) in the absence of hydrogen gas. Experiments were carried out in a batch reactor using an artificial model hydrothermal carbon derived from glucose with isopropanol as the solvent at 400 °C for a 3 h batch time. Initial studies using noble metal catalysts (Rh, Pt, Pd, and Ru) on a carbon support revealed that Pt was the best catalyst in terms of hydrothermal carbon conversion (77%) and amounts of alkylphenolics and aromatics in the product oil (GC × GC-FID). Subsequent support screening studies (TiO_2, ZrO_2, and CeO_2) were performed using Pt as the active metal and the results were compared with those of Pt/C. The best results were obtained with Pt/C when considering hydrothermal carbon conversion. However, Pt/CeO_2 was shown to be more attractive when considering the amounts of alkylphenolics in the product oils (20.4 wt% based on hydrothermal carbon intake). Detailed liquid product analysis (GPC, GC-MS, and GC × GC) including blank reactions in the absence of hydrothermal carbons revealed that the hydrochars are mainly converted to monomeric and oligomeric alkylphenolics and aromatics (GPC and GC). IPA is not inert and is converted to acetone and hydrogen, and the latter is the hydrogen source for the various metal catalysed hydrogenolysis and hydro(deoxy)genation reactions. In addition, acetone is converted to aldol condensation products (such as methylisobutylketone, MIBK) and hydrogenation products derived thereof. An overview of the various reactions occurring during the reactive liquefaction process is given in Fig. 32. Though a complex reaction mixture is obtained with products from both hydrothermal carbon and the solvent, efficient separation technology may allow the separation of the aldol condensation products (such as MIBK) and alkylphenolics from the mixture. Both components are commercially available bulk chemicals with a high application range. For instance, MIBK is used as a solvent, whereas mixtures of alkylphenolics may be used as a replacement of phenol in phenol based adhesive formulations.[322] In addition, mixtures of alkylphenolics may also be used as biofuel blending agents to improve diesel engine performance.[323]

Further systematic studies to obtain high amounts of alkylphenolics were performed using a Pt/C catalyst in IPA.[321] The highest hydrothermal carbon conversion achieved in this study was 72%. The main hydrothermal carbon derived products were aromatics, alkylphenolics and aliphatic hydrocarbons, which was confirmed by performing blank reactions with IPA and Pt/C in the absence of hydrothermal carbon. The highest amount of alkylphenolics was 14% based on GC detectable products in the liquid phase after the reaction. The catalytic hydrotreatment of hydrothermal carbon in the presence of mixtures of FA and IPA using supported Ru catalysts has also been investigated.[324] Best results were obtained using Ru/C and hydrothermal carbon conversions up to 69% were achieved using a combination of FA/IPA as the hydrogen donor. Elemental analysis showed that the oils have a considerably reduced oxygen content compared to the hydrothermal carbon feed, with HHVs up to 38 MJ kg^{-1}. The product oils were shown to consist of both monomeric and oligomeric compounds (GPC). Main GC detectable species arising from the hydrochar were substituted alkylphenolics, naphthalenes and cyclic alkanes (GC-MS-FID, GC × GC). Recently Saha and co-workers[325] reported the catalytic hydrotreatment of hydrothermal carbons in methanol with additional molecular H_2 as the hydrogen source using various noble metals supported on carbon. Experiments were performed in a batch autoclave at 350 °C under 30 bar H_2 with a 3 h batch time. The highest yield of the product oil was 43 wt% at 55% conversion of the hydrothermal carbon using Pt/C. All other catalysts were less effective (Ru, Pd and Rh). However, the amounts of GC detectable in the oil (10%) were relatively low. Reaction parameters, including the reaction time, temperature, H_2 pressure and catalyst-to-hydrothermal carbon mass ratio were optimized. Higher reaction temperatures were shown to have a positive effect on the hydrothermal carbon conversion. However, the product oil yield does not progressively increase with temperature and shows a maximum at about 400 °C due to excessive gasification at high temperatures. Isotopic-labelling experiments were conducted using ^{13}C-labeled methanol to investigate whether methanol only serves as a hydrogen source or also reacts with the intermediates or products of the liquefaction reaction. The results imply that methanol is incorporated as an –OCH_3 group in the products, formed by for instance esterification reactions of hydrothermal carbon-derived fragments and as methyl groups on aromatic units, likely by alkylation reactions.

4.7.2. (Catalytic) pyrolysis. Liquefaction of hydrothermal carbon obtained from the HTC of glucose and fructose using pyrolysis technology with the objective to obtain high liquid yields was investigated by Rasrendra *et al.*[326] Pyrolysis GC-MS (300–600 °C, 10 s, He atmosphere) showed the presence of furanics and organic acids in the vapour phase, though the individual components were present in only minor amounts (<1 wt%). Micro-pyrolysis (500 °C, 12 s, N_2 atmosphere) yielded 30 wt% of gaseous and liquid products, the remainder being a solid char. Liquid yields were by far lower than that obtained for a typical lignin sample (Kraft lignin) under similar conditions. As such the authors concluded that pyrolysis of hydrothermal carbon is cumbersome and gives relatively low liquid yields. The catalytic pyrolysis of hydrothermal carbons, including those from the HTC of model sugars and industrial hydrothermal carbons, for BTXNE synthesis (benzene, toluene, xylenes, naphthalene, and ethylbenzene) has been reported by Agarwal *et al.*[327] Initially, the catalytic pyrolysis of a synthetic hydrothermal carbon from glucose using various zeolite catalysts was investigated in a small-scale catalytic pyrolysis set-up (PTV-GC/MS) at 550 °C to identify the best catalyst for liquid products enriched in valuable bulk chemicals such as BTXNE. Remarkable differences in the yields of aromatics (BTXNE) were observed for the various catalysts. Lowest BTXNE yields were found for neutral and basic zeolites, indicating that acidic zeolites are desirable for the aromatization of the pyrolytic vapours from hydrothermal carbon. For such acidic zeolites, the BTXNE yield increased in the order: ferrierite 20 < HY–80 < HY 5.1 < H-mordenite 20 < H-ZSM-5. The catalytic

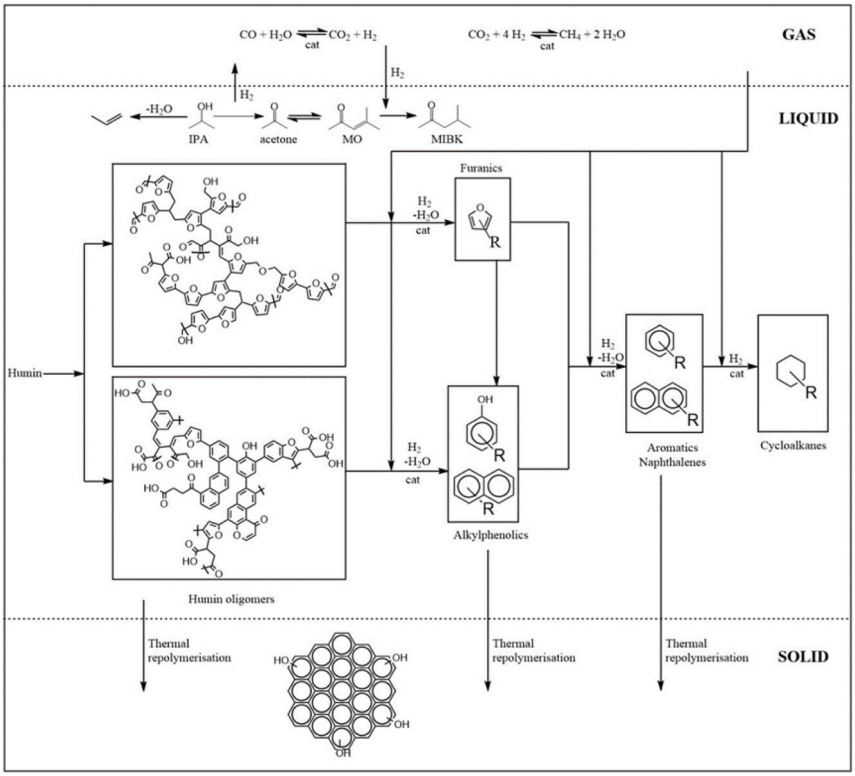

Fig. 32 Overview of reaction pathways occurring during the catalytic hydrotreatment of hydrothermal carbon in IPA; reproduced with permission from ref. 324.

pyrolysis of synthetic and industrial hydrothermal carbons using HZSM-5 with different SiO_2/Al_2O_3 ratios (23, 50 and 80) and as such with different acidity levels (highest for 23) was investigated. The results revealed that HZSM-5 with a SiO_2/Al_2O_3 ratio of 50 gives the highest yield of aromatics for both types of hydrothermal carbons. The BTXNE yield is significantly higher for the industrial hydrothermal carbon (10 wt%) than that of the synthetic one (1.5 wt%). In addition, catalytic pyrolysis experiments were performed with an industrial and synthetic hydrothermal carbon at an in house-built reactor setup consisting of two reactors (the first reactor for the pyrolysis of the hydrothermal carbon and the second for the zeolite catalyst) to obtain a liquid product and to determine the mass balance. The total amount of detectable aromatic species in the product oil for industrial and synthetic hydrothermal carbons were at max. 9 and 2 wt% on hydrothermal carbon intake, respectively, which confirms the results from the PTV-GC/MS experiments. These studies reveal that a thermochemical pyrolysis approach to depolymerise hydrothermal carbon suffers from low liquid yields and the formation of substantial amounts of solid char. Catalytic pyrolysis approaches aiming for aromatics such as BTXNE seem more promising.

4.7.3. Hydrothermal carbon liquefaction using catalysts and conditions typical for aqueous phase reforming. van Zandvoort *et al.*[314] recently reported liquefaction studies using solubilised glucose hydrothermal carbons. Obtained by an alkali treatment, under typical aqueous phase reforming (APR) conditions (225–250 °C, pH 9–11, 20 h, batch) using various supported Pt-based catalysts. Best results were obtained using Pt–Re on a ZrO_2 support giving up to 8 wt% of a product-oil which was shown to mainly contain phenolics and aromatic ketones (GC-MS). Insoluble hydrothermal carbons, without a prior alkaline pre-treatment, were also investigated. In this case, only 3 wt% of a product oil was formed together with comparable gas yields as for the alkali-treated hydrothermal carbon. The product oil was shown to contain more furanic structures and less phenolics. This difference in product distribution is related to the difference in structures between the soluble, alkali treated hydrothermal carbon and the original hydrothermal carbon. The latter was shown to be rich in furanics, whereas the solubilisation in an alkaline medium resulted in the formation of a structure with more (polycyclic) aromatics present. As such, this study shows catalytic conversions of (solubilised) hydrothermal carbon under APR conditions resulting in the formation of a gas phase with some H_2, CH_4 and CO_2 and a liquid product with phenolics and/or furanics.

4.7.4. Gasification. Gasification and particularly steam reforming of hydrothermal carbon (900–1200 °C) with the objective to obtain syngas (mixture of CO_x and hydrogen) was studied by Hoang *et al.*[328] Various alkali–metal-based catalysts (Na_2CO_3, K_2CO_3, Cs_2CO_3 and $CaCO_3$) were screened for the reactions and Na_2CO_3 showed the highest activity. Gas phase analyses showed that the syngas typically has a H_2/CO ratio of

Table 7 Products of decomposition of lignocellulosic biomass under hydrothermal conditions[335–338]

Aldehydes, ketones and monosaccharides	Furan derivatives	Carboxylic acids	Phenols
Glucose	Furfural	Pyruvic acid	Guaiacol
Fructose	5-HMF	Glycolic acid	Catechol
Xylose	Furfuryl alcohol	Acetic acid	Cresol
Erythrose	2-Methylbenzofuran	Lactic acid	
Dihydroxyacetone	Soluble polymers	Formic acid	
Levoglucosan		Levulinic acid	
Pyruvaldehyde		Propionic acid	
Glyceraldehyde			
Formaldehyde			
Acetaldehyde			
2,5-Dioxo-6-hydroxyhexanal			

2. However, substantial loss of carbon to vapours was observed during the heating up stage in the gasifier (up to 45 wt% on intake). To improve carbon yields, a second catalytic reactor was proposed to gasify the volatiles formed during the heating phase to increase the solid to gas carbon efficiency. Dry/CO_2 reforming of hydrothermal carbons with Na_2CO_3 was also studied.[329] Without a catalyst, only 7 wt% of the hydrothermal carbon was converted at 750 °C, which increased to 20 wt% at 900 °C. The addition of Na_2CO_3 substantially increased the hydrothermal carbon conversion rate, and a near quantitative conversion was achieved at 725 °C.

4.7.5. Conclusions. Considerable progress has been made in the liquefaction of hydrothermal carbons obtained by HTC using a number of catalytic approaches. All findings reveal that the oligomeric/polymeric and recalcitrant structures of hydrothermal carbons may be (partly) depolymerised to liquid and gas phase products, though the product yields are generally rather low due to the formation of substantial amounts of solid residues. The liquid phase obtained by a catalytic hydrotreatment has potential to be used as a source for interesting bulk chemicals after fractionation. This opens new avenues for the development of added-value product outlets for hydrothermal carbons beyond the use as a solid fuel. As such, this will have a positive effect on the techno-economic viability of biorefinery schemes involving the conversion of C5 and C6 sugars to biobased chemicals such as levulinic acid and HMF with the inevitable formation of hydrothermal carbons.

5. Soluble carbonisation products

The complexity of transformations and reaction pathways occurring during hydrothermal carbonisation of lignocellulosic biomass is reflected in the large number of soluble products found in the aqueous phase. However, all chemicals can be grouped into four classes: aldehydes/ketones (including saccharides), furan derivatives, carboxylic acids and phenols.[76,303,330–334] First three classes of compounds can always be found in a relatively high amount or in traces after hydrothermal carbonisation of mono- and polysaccharides, whereas phenols are only found in real biomass HTC, as they arise from hydrolysis of lignin. Xylose, furfural and furfuryl alcohol are derived from the hemicellulosic fraction of biomass.[331–334] Table 7 shows an extended list of the main carbonisation products grouped in the four above-mentioned classes.

5-Hydroxy-methylfurfural (5-HMF) is probably the most renowned and sought-after of all hydrothermal carbonisation products. It is derived from dehydration of C6 monosaccharides. The huge interest around this compound arises from the reactivity of its two functional groups, methoxy- and aldehydic, and the possibilities of derivatisation that they offer. In fact, 5-HMF has been recognized as a valuable bio-based chemical building block[16] which can play a key role not only as an intermediate for the production of the biofuel dimethylfuran (DMF), but also for other biomass-derived intermediates, such as 2,5-furan-dicarboxylic acid,[339] 2,5-dimethylfuran,[340,341] adipic acid and levulinic acid (LA).[342] As a consequence, a few processes for industrial scale synthesis of 5-HMF from monosaccharides have already been patented. AVA Biochem, a Swiss based company, has been involved in the industrial scale production of 5-HMF derived from biomass since 2013, with an annual production of 20 tonnes. AVA Biochem's approach is based on carbonisation of fructose in water at high pressure. Fructose is in turn obtained from previous treatment of biomass waste. The traditional disadvantage of the production of a remarkable amount of hydrothermal carbon as a byproduct of condensation and polymerization of 5-HMF is avoided by extracting 5-HMF from the system before the condensation and polymerization steps take place. The final product is either a 99.9% pure crystalline solid or is available in solution for further processing. Moreover, as the conversion of fructose in a single step is not complete, the process has been designed to incorporate a recycling step of the unreacted sugar, to enhance overall conversion. These series of improvements have allowed the process to be scaled to the industrial level.[343]

Levulinic acid (LA) is considered as one of the most promising platform chemicals produced from lignocellulosic biomass for fuels and chemicals.[344,345] It is regarded as a speciality chemical that finds applications for several purposes, such as a source of polymer resins, animal feed and food as well as components of the flavouring and fragrance industry, textile dyes, additives, extenders for fuels, antimicrobial agents, her-

bicides and plasticizers.[346,347] The biorefinery process employs cellulosic biomass for the synthesis of levulinic acid and formic acid. The conversion takes place in two steps: the ground biomass is injected into the first reactor, where it is then mixed with dilute sulfuric acid at a temperature of 210–220 °C and a pressure of 25 bar. A residence time of 12 seconds is sufficient for the hydrolysis and dehydration reaction to occur, leading to the synthesis of a 5-HMF intermediate. Subsequently, the mixture is moved to a second, larger reactor. Here the acidic catalyst concentration is the same, while temperature and pressure are milder. A longer residence time of 20 minutes is necessary to complete the reaction of rehydration of 5-HMF to levulinic acid and formic acid. Furfural and other by-products are removed at this stage. Water is subsequently boiled off, along with the remaining volatiles, and levulinic acid is extracted from the resulting mixture by distillation. In this process, approximately 50% of the initial mass of 6-carbon sugars is converted to LA, 20% to formic acid and 30% to tar.[348]

Furfural is largely produced by dehydration of pentose sugars rich in hemicellulose. In fact, currently, commercial production of furfural exclusively relies on dehydration of lignocellulosic biomass. The typical process involves the breaking down of the hemicellulose fraction of a lignocellulosic biomass in a 3% sulfuric acid solution for 3 hours, in a range of temperatures between 170 and 185 °C. Under these conditions, 40–50% of the potential furfural is obtained. The undissolved residual solid, composed of lignin and cellulose, is recovered and employed for energy recovery, while the acid catalyst is recycled.[349] Several mechanisms have been speculated to explain pentose dehydration to furfural including both acyclic and cyclic intermediates. However, it is reasonable to think that the most plausible mechanism under acidic conditions involves acyclic xylose isomerization to xylulose followed by further dehydration and cyclization to furfural.[43] The interest in bio-derived furfural arises from the many possibilities that this molecule offers in terms of catalytic upgrading to fuel additives.[350]

The abovementioned compounds have received a great deal of attention because of their primary role in the transition to sustainable, bio-based fuels and materials. However, among the numerous other chemical compounds, some organic acids such as lactic acid, formic acid and acetic acid are worth mentioning. Despite their limited strategic relevance, they still have commercial value due to their abundance as by-products in the hydrothermal conversion of biomass and levulinic acid synthesis. Lactic acid (LacA) is a promising platform chemical for the synthesis of solvents (ethyl lactate), biodegradable plastics (polylactic acid, PLA) and other polymer precursors (acrylic acid).[16,351] Formic acid can serve as a starting compound for the synthesis of green solvents,[348] whereas acetic acid could replace inorganic acids for the synthesis of roadway deicer salts.[352]

5.1. Element distribution in the liquid and gas-phases

Significantly less composition data have been reported for the gas and liquid carbonisation products. Fig. 33 provides a summary of the fraction of initially present carbon transferred to the gas and liquid-phases following carbonisation. As shown, a small fraction of initially present carbon is transferred to the gas-phase, which is consistent with that reported in the literature. Generally, as the reaction severity increases, the fraction of carbon in the gas-phase increases.[71,76,303,353] The carbonisation of paper results in the greatest transfer of carbon to the gas, which is not surprising because the conditions associated with the carbonisation of paper also represent the largest average severity factor. Conversely, a significant fraction of carbon is transferred to the liquid-phase as a result of carbonisation, which may have significant implications associated with using the liquid-phase as an energy source *via* anaerobic digestion.[354,355] The distribution of data describing this fraction of carbon is quite large, likely because of the significant influence process conditions have on liquid-phase carbon contents.[68,71,72,76,353,356] Unlike that associated with other carbonisation products, there is a trend associated with the severity factor, which is consistent with that reported in the literature. At low average severity factors, large fractions of carbon are transferred to the liquid-phase. As average severity factors increase, the transfer of carbon to the liquid-phase decreases. These trends are consistent with those reported in the literature.[71,76]

5.2. Influence of feedwater and catalysts on soluble carbonisation products

HTC of biomass is usually performed under acidic conditions, because hydrolysis and dehydration reactions are catalyzed by hydronium ions. As mentioned before, 5-HMf is the pivotal compound in the whole process of transformation, as it is the starting point for both conversions to dissolved products (levulinic acid) and solid products (hydrothermal carbon). Therefore, any consideration of the influence of reaction parameters on the final products of hydrothermal carbonisation must take into account the reactivity of 5-HMF. The rate-limiting step in the dehydration of glucose to 5-HMF in acidic medium is the isomerization of glucose to fructose.[44,357] This explains the reluctance of glucose, compared to fructose, in dehydrating to 5-HMF: in fact, isomerization of glucose to fructose is base catalyzed and therefore it is slower under typical acidic conditions for the synthesis of 5-HMF.[44]

The nature of the acid used to catalyse the dehydration of saccharides plays a major role in the final yield and distribution of products. Lu *et al.* noted faster kinetics in HCl catalysed hydrolysis of cellulose compared to that of H_2SO_4 in the same concentration.[356] Reiche *et al.* described a different behaviour in HTC of 20 wt% glucose solutions treated with HCl or HNO_3 with the same synthesis pH. Nitric acid, in fact, due to the oxidizing properties of NO_3^-, drives the conversion towards higher yields of hydrothermal carbon in spite of the formation of 5-HMF, levulinic acid and formic acid. Hydrochloric acid, conversely, catalyses more efficient conversion of glucose to HMF and levulinic acid subsequently, with much lower HTC carbon yields. It is also worth pointing out a strong imbalance between levulinic acid and formic acid, in

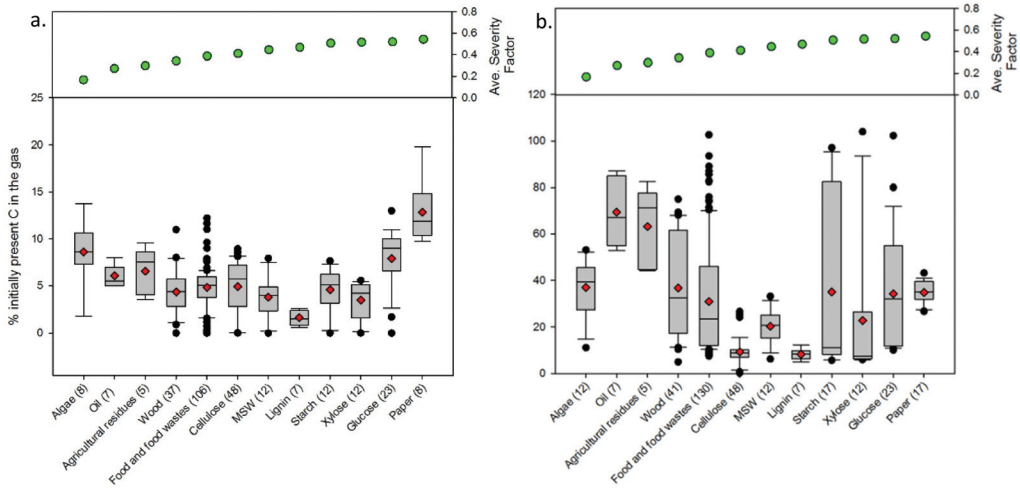

Fig. 33 Distributions associated with the percentage of initially present carbon in the (a) gas and (b) liquid-phases following the carbonisation of different feedstocks. The line in each box represents the median value. The ends of each box represent the 25th and 75th percentiles associated with the data. The red diamonds represent the average values. The lines and data points represent the scatter of data beyond the 10th and 90th percentiles. The numbers in parentheses following each feedstock category represent the number of data points represented on the plot.

favour of the former, for both HCl and HNO_3 acidified samples, despite a theoretical ratio of 1 : 1. This effect is particularly strong at a synthesis pH of 0. Under these conditions, the strong acidity makes formic acid and other carboxylic acids break down into gaseous species (CO and CO_2), also causing a slight rise in the final pH.[358]

Hydrothermal treatment of poly- and monosaccharides under basic conditions leads to a quite significant change in the scenario. In fact, although bases such as NaOH, KOH and $Ca(OH)_2$ are all able to accelerate the hydrolysis of cellulose to glucose, they somehow change the pathway of carbonisation, slowing down its dehydration to 5-HMF, with a consequent buildup of the glucose concentration and lower yields of levulinic acid.[338,356] On the other hand, a rise in formic acid and lactic acid concentrations is observed with higher synthesis pH,[338] pointing out the preferred pathway of degradation of the hexoses, involving retro aldol condensation, as shown in Fig. 6.

Salt anions too can affect the conversion of sugars under hydrothermal conditions. In fact, anions with good leaving group qualities can strongly accelerate the rate of dehydration of fructose to 5-HMF, provided that they are also small and good nucleophiles. This is due to their intervention in the first step of dehydration of fructose, which involves substitution and elimination reactions on the C2 carbon.[359] Lewis acids are also of interest in the homogeneous catalysis of dehydration reaction as substitutes of traditional Brønsted acids, due to their lower corrosivity. Various Lewis acids have been studied for carbohydrate conversion. Dehydration of glucose has been achieved using $CrCl_2$ in an ionic liquid with 70% yield of HMF;[360] $CrCl_3$ and HCl with 59% yield of HMF in water (NaCl)/THF biphasic medium;[361] and $SnCl_4$ in an ionic liquid to afford a 64% yield of HMF.[362] More recently, Jiang *et al.*[363] have achieved a yield of levulinic acid of 88% in biphasic medium (water : MeTHF) at 200 °C in 60 min (pH 1) with $FeCl_3$ and a yield of 56% for 5-HMF in a biphasic solution at higher pH (pH = 2) in 180 min with $FeSO_4$. Weiqi *et al.*[364] have studied the synergistic effect of coupling $CrCl_3$ and H_3PO_4 on glucose conversion to LA compared to a single use of $CrCl_3$ or H_3PO_4. The highest LA yield of 54.24% was obtained from 100% glucose conversion at 170 °C for 240 min. CO_2 in hydrothermal applications can be considered as both a Lewis acid in gaseous form or Brønsted acid in its hydrated form. In any case, it has been proved to be effective at catalysing carbohydrates to 5-HMF. Lin *et al.*[365] have obtained a 5-HMF yield of 60.33% from fructose conversion at 190 °C for 20 min with a CO_2 pressure of 2 MPa. There is proof that compressed CO_2 is also effective at hindering the formation of undesired 5-HMF oligomers, thus improving the conversion yield of sugar to 5-HMF.[366] Using heterogeneous catalysis has the significant advantage of avoiding tedious recovery steps that are necessary for homogeneous catalysts. The most recent heterogeneous catalysts proposed include transition metal oxides,[367] phosphates,[368,369] zeolites,[370] organic polymers,[371] and carbon sulfates.[372–374]

5.3. Influence of reaction time and temperature on soluble carbonisation products

Several studies have investigated the effect of reaction time and temperature on product yields in the liquid phase after hydrothermal carbonisation of carbohydrates and lignocellulosic feedstock. Table 8 provides a summary of the reaction conditions used in the papers taken into account. Seen from the perspective of reaction time, in the early stages of polysaccharide conversion, the HTC liquid phase is characterised by a relatively high concentration of sugars (glucose) and aromatics (5-HMF). As a general trend, it appears that hydro-

Table 8 Summary of carbon precursors and reaction conditions used to study the impact of reaction parameters on product yields in the HTC liquid phase

Carbon precursor	Biomass/water ratio (wt%)	Reaction temperature (°C)	Reaction time	Ref.
Starch	10%	180, 200, 220, 240	2 to 40 min	330
Biomass (Jeffrey pine and white fir)	12.5%	215, 235, 255 275, 295	30 min	303
		255	5 to 60 min	
Cellulose	20%	225, 250, 275	0 to 96 h	76
Cellulose, wheat straw, poplar	12.5%	200, 230, 260 (fixed)	0 to 8 h	331
		160–260 (dynamic)	—	
Coconut husk, rice husk	10%	140, 160, 180, 200	4 h	332
		200	1, 2, 3 h	
Cassava rhizome	20%, 10%, 6.6%	160, 180, 200	1, 2, 3 h	333
Corncomb	20%, 10%, 6.6%	160, 180, 200	1, 2, 3 h	334
Sucrose, glucose, fructose	2% (sucrose) 1.05% (glu., fru.)	180	2 to 24 min	357
		200, 220	2 to 18 min	

lysis of polysaccharides to simple sugars consistently increases with temperature, with the maximum yield shifting to shorter reaction time as temperature increases.[303,330] The highest sugar yields are generally found between 180 °C and 230 °C and between 1 hour and 2 hours.[331,333,334] Fructose yields are generally lower than glucose yields[330,331] and this may serve as proof that the reaction of fructose dehydration to 5-HMF is kinetically faster than the isomerization of glucose to fructose. Therefore, in the early stages of hydrolysis of cellulose, the concentration of glucose builds up, whereas fructose is readily consumed. 5-HMF yield is very dependent on both the reaction time and temperature and its production is strictly connected to the sugar content in the liquid phase. Although the time scale of the 5-HMF concentration peak may vary from a few minutes to hours, depending on the type and size of the reactor,[330,331,333,334] it always follows the maximum in monosaccharide concentration. 5-HMF prefers moderate temperature for optimal yields (180–220 °C),[331,333,334] while higher temperatures cause faster conversion but lower yields, due to the increase of secondary reactions. Experiments on the conversion of simple sugar monomers (glucose and fructose) and dimers (sucrose), although being conducted in the presence of an acid catalyst and therefore being kinetically faster, lead to a similar conclusion.[357] Xylose and furfural are only minor products in the hydrothermal carbonisation of hexoses.[357] In contrast, furfural becomes much more relevant in hemicellulose-rich biomass and its decline throughout the process is slower compared to that of 5-HMF, which indicates a slightly higher stability.[331] Finally, organic acids tend to prevail as the reaction time proceeds and higher temperatures are used, with acetic acid being particularly high in concentration in HTC of lignin-rich biomass.[303,331–334]

5.4. Chemical isolation

HTC typically occurs in water or aqueous medium, where the chemical products of interest are found at the end of the reaction. Typical compounds found in the water phase are carboxylic acids, aldehydes, ketones and furfural derivatives. Although the yields of conversion may vary, the concentrations of these products are quite diluted, making separation by direct distillation unfavourable. Therefore, every process designed to convert cellulosic biomass into platform chemicals must deal with a liquid–liquid extraction step. A good solvent for liquid–liquid extraction must fulfil some basic requirements: it must extract effectively and selectively the compound of interest; it must be recoverable by distillation, in order to be recycled, thus lowering the production costs; it must be poorly soluble in water, in order to minimize losses during extraction; it must have a fairly different density from water, to allow quick separation. In addition to these fundamental features, from the perspective of a greener process, it should also be inexpensive and non-toxic.[375] Several organic solvents have been evaluated for the liquid–liquid extraction of 5-HMF, levulinic acid and furfural. Methyl isobutyl ketone (MIBK),[376,377] 2-butanol,[340,376] THF,[378] and 2-MTHF[378] are most frequently used for the extraction of HMF, although some other alternative solvents such as dimethylcarbonate,[369] o-propylphenol[379] or hexafluoroisopropanol[380] have been proposed due to their remarkably high partitioning coefficients. MIBK in particular has been proven to be the best solvent for the extraction of 5-HMF in a counter current, due to the combined effect of its high partition coefficient and its lower solubility in water, compared to other solvents. Addition of sodium chloride further improves the partition coefficient.[381] Exploiting the salting-out effect of some common salts is an effective method to maximize the liquid–liquid extraction. Salting-out efficiency has been demonstrated to be roughly independent of the nature of the cations; in fact, it only depends on the anion used. Moreover, the partitioning behaviour of the salt is roughly independent of the extraction solvent used.[382] Pentasodium phytate, a green and cheap salting-out agent derived from cereals and currently considered waste, has also been considered as an alternative to inorganic salts. In a comparative study with other inorganic salts in a water/1-butanol/HMF system, the most pronounced separation of HMF than the other tested sulfates has been shown.[383] Salts can also increase the separation efficiency when a system of two mixed solvents is used instead of one single pure solvent. However, subsequent recovery of the solvents can be reduced upon addition of salts due to the for-

mation of complexes.[384] When ionic liquids are used as reaction media for dehydration of sugars to HMF and levulinic acid, extraction with the aforementioned solvent leads to very poor yields. This has been explained with the strong H-bond interaction between the hydroxyl group of HMF and the anion of the IL.[385] In fact, it has been observed that the addition of small chain alcohols, by interfering with the aforementioned H-bond, results in a significant improvement of the extraction efficiency of HMF by MIBK.[386] Compressed CO_2 as the extraction solvent of HMF from ILs has also been considered, proving to be a promising approach due to the combination of both the extraction efficiency and enhanced solubility of glucose in the IL medium.[387] Brouwer *et al.*[388] have recently proposed a method to separate furfural, levulinic and formic acid in different stages from the same acidic aqueous stream. Furfural is extracted in the first stage with toluene. Subsequently, levulinic acid and formic acid are extracted with a mixture of 30% TOPO (trioctylphosphine oxide) in MIBK, with a high partition coefficient and selectivity over sulfuric acid. A double temperature swing back extraction has been performed to concentrate LA and FA, therefore lowering the energy required for the final distillation step to obtain levulinic acid.

6. Carbon dots

Apart from the formation of new chemical compounds in the liquid phase, there is an interface grown between the solid carbon microsphere and liquid chemicals, which is considered as a third product. This is where the nucleation process takes place as a new phase is formed, leading to thermodynamic instability. The small nuclei formed at this interface represent the fluorescent carbon dots (CDs) with a size generally below 10 nm, which were previously reported *via* the HTC process.[389] Because of some unique properties, such as low toxicity, high photoluminescence (PL) quantum yield, facile modification and excellent electron donating/accepting abilities, CDs have found applications in many fields, ranging from bioimaging to sensors, LEDs, photocatalysis, solar cells and more.[24,390,391]

The electronic states and optical properties that make CDs suitable for the above-mentioned applications are strictly connected to their structural features, which can be controlled during synthesis. On that note, a detailed mechanism for the formation of CDs from molecular precursors is of vital importance to better understand the unique properties of these materials and also facilitate control of their key characteristics.

6.1. Formation mechanism

So far, two different mechanisms have been proposed in the literature. One suggests a growth according to the classical La Mer model,[392] where the resulting nuclei grow uniformly and isotropically by diffusion of solutes towards the particle surface until the final size is attained.[392] It is usually divided into several stages, which depending on the classification can be summarized as decomposition, condensation, polymerisation, nucleation (aromatization) and growth. Wang *et al.* reported a simple model of the different stages in 2012.[393] Some people also infer the final step as surface passivation by the residue precursor.[394,395] Liu and co-workers prepared nitrogen and sulfur co-doped CDs *via* hydrothermal treatment of L-cys and $NH_3{\cdot}H_2O$.[394] They have claimed that L-cys molecules went through a few steps from decomposition to passivation, as shown in Fig. 34A. The HRTEM images of CDs being impeccable gradually support the possible formation mechanism. In one of the earlier reports, Sahu *et al.* have proposed a simplified 3-step explanation for the formation mechanism of hydrothermally synthesized CDs.[20] The authors have concluded that the dehydration and decomposition of fructose/glucose gave rise to different soluble chemical compounds, as mentioned before in the liquid phase. Hydronium ions formed from these acids acted as a catalyst in subsequent decomposition reaction stages. The polymerisation and condensation of these soluble chemicals gave rise to soluble polymers where aromatization took place *via* aldol condensation, cycloaddition and hydroxymethyl-mediated furan resin condensation.[50] When the concentration of aromatic clusters reached a critical supersaturation point, burst nucleation took place, and carbon dots were grown. Similarly, the particle formation of CDs reported from banana juice[396] and sweet potato[397] also follows the three steps of carbonisation of carbohydrates. Later Qu *et al.* synthesized N-doped graphene quantum dots (GQDs) with a hydrothermal method with citric acid and urea.[398] They concluded that the formation of N-doped GQDs involved two steps. In the first step, citric acid molecules self-assembled into sheet structures and dehydrolyzed to form a graphene framework, and the reaction between citric acid and amines occurred. Through the second step of intramolecular dehydrolysis, amides reacted with carboxylic groups and formed pyrrolic N. Similar methods have also been reported by Bai *et al.* for N-doped CDs produced from citric acid and ethylenediamine,[407] and Atchudan *et al.* with *Chionanthus retusus* fruit extract.[400] Our group has been pioneering in the field of HTC for the last decade and based on the structural investigation of CDs, we propose an evolutional mechanism, which involves the influence of the gas phase during the reaction.[401,402] We believe that some of the polymeric nuclei formed initially during the hydrothermal process act as hot spots (due to temperature gradients existing in the autoclave during the HTC process). At the same time, CO/CO_2 gas along with H_2 are formed *in situ* in the autoclave from partial gasification of glucose under subcritical conditions. These gases deposit onto the hot spot nuclei in a CVD-like process *via* CO_2 reduction under autogenic pressures (30 bars) leading to the formation of crystalline carbons. With the observation from the HRTEM images in Fig. 34B, we hypothesize that the first crystalline form of CDs is sp^3-bonded carbon obtained from an amorphous/carbon black type which then can further convert into carbon anions which subsequently form graphitic structures.[403] During the incipient stage of glucose transformation *via* the "hot spot CVD" mechanism mentioned above, a mixture of sp^2/sp^3 carbon nanostructures are initially formed

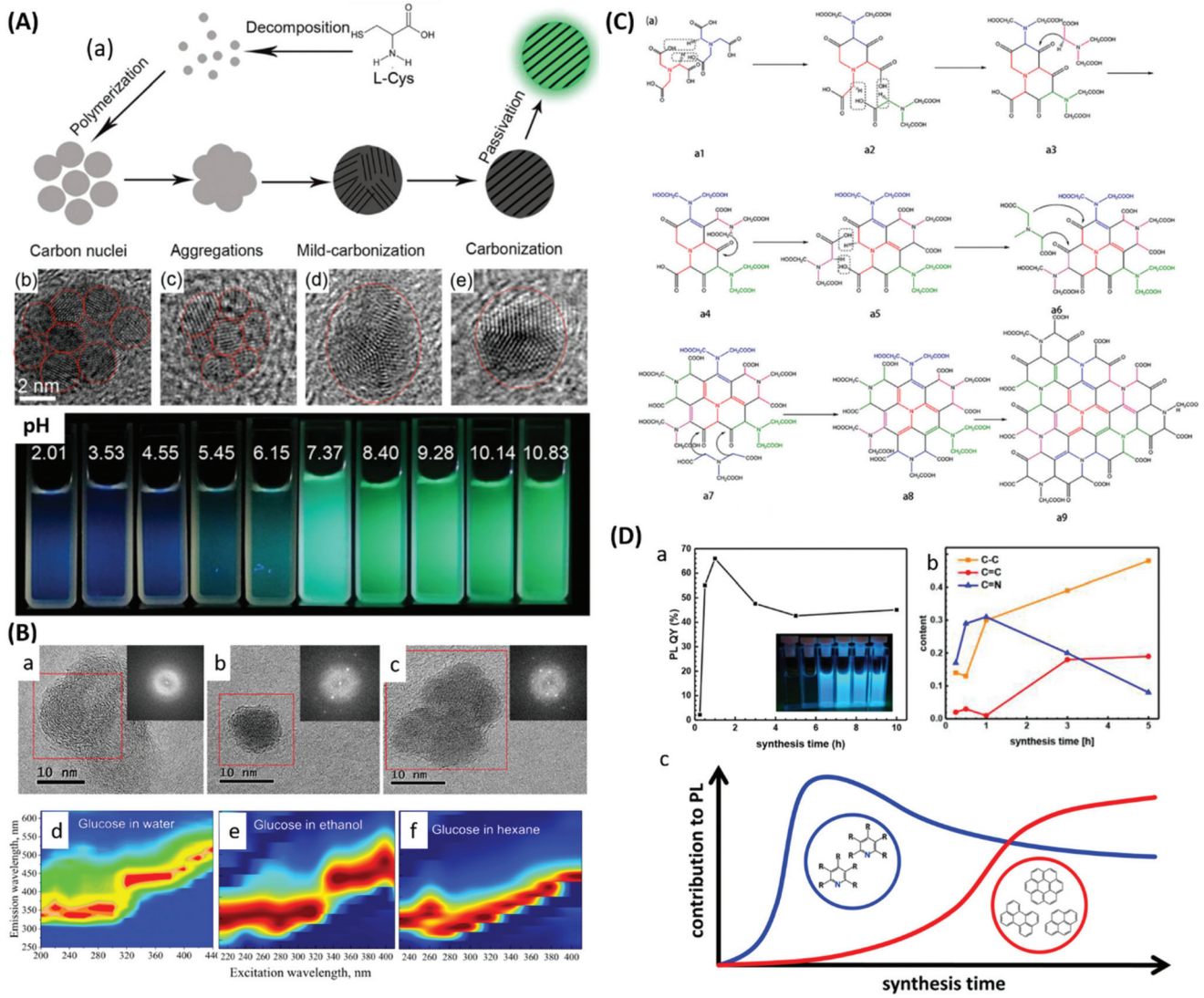

Fig. 34 (A) Schematic illustration of the possible mechanism for the formation of N,S-CDs using L-cys as the carbon source, HR-TEM of CDs at different formation stages, and the PL behaviour under different pH values; reproduced with permission from ref. 394. (B) HR-TEM images showing the evolution of glucose derived CDs and the influence of solvent polarity on the excitation-dependent PL properties; reproduced with permission from ref. 401. (C) Mechanism of the reaction from NTA to N-doped GQDs; reproduced with permission from ref. 404. (D) (a) PL QY of CDs as a function of reaction time, (b) evolution of the relative amount of C–C, C=C, and C=N bonded C atoms inside the CDs during the synthesis, and (c) the scheme of different structures contributing to PL with respect to time; reproduced with permission from ref. 405.

which are later converted into predominately sp^2 carbon nanostructures.[403]

Jiang and co-workers modelled the polymerization process of nitrilotriacetic acid (NTA) to form N-doped GQDs under hydrothermal conditions (250 °C, 4 h), and concluded that the mechanism involved dehydration and nucleophilic addition between different NTA molecules to form a conjugated system, as shown in Fig. 34C, which grows into larger CQDs as the reaction continues.[404] The other formation mechanism involves local nucleation on some high energy areas. Dai *et al.* synthesized hydrothermal CDs and proposed a formation mechanism based on the temperature increase.[406] At first, formation of large-sized polymeric nanoparticles through intermolecular dehydration occurred upon high temperature and pressure exposure of the precursor. As the reaction proceeded, nucleation started as the aforementioned polymeric nanoparticles partitioned, resulting in the coexistence of polymers and CDs. Upon further increase in heating time, CDs constantly surpassed the polymer nanoparticles until the latter disappeared. Similar processes have also been reported by Yang *et al.* with amino acid with respect to the time increase.[407] Unfortunately, in all the above cases, the formation mechanism appears as a hypothetical suggestion and there is no clear evidence *via in situ* characterisation to

support it. Therefore, an in-depth insight involving *in situ* techniques is crucial for the survival of these systems initially and later to accomplish their commercialization.

6.2. Reaction parameters

At this stage, it is crucial to explore the parameters affecting the properties of the resulting CDs during their synthesis. It is well-known that surface groups in particular are highly dependent on the conditions of the synthesis, such as the solvent, temperature and pH. The solvents can affect the excitation dependent PL properties, as shown in the maps in Fig. 34B, and this is generally attributed to the presence or absence of oxygen-containing functional groups. Such groups are formed easily in solvents with stronger hydrophilicity and higher polarity (such as water and ethanol), enhancing blue emission. In contrast, low polarity solvents such as cyclohexane and toluene show a negligible amount of oxygen-related groups, decreasing blue emission, while increasing the red one.[408,409] Temperature is another key factor in the preparation of CDs. Several physical, chemical and optical properties of the resulting products can be affected by the reaction temperature such as the particle size, crystallization and surface functionality and as a consequence the PL intensity and peak position.[410,411] The different pH environment during HTC can largely affect the PL properties of CDs by affecting the reversible protonation and deprotonation of the abundant functional groups.[412] Each functional group contributes to the overall emission in a different way in different pH ranges, therefore leading to intensity variation or even shifting the peak position. Compared to the other parameters, the reaction time can influence the CD formation stage, which changes the structural and optical properties accordingly. Bai and co-workers changed the reaction time of metronidazole derived CDs and found that the formation of CDs starts after 3 h. They monitored the surface functional group changes using FTIR techniques and learned that the surface groups of CDs changed gradually, with $-NO_2$ reduced to N–H, while C–OH and C–H oxidized to C–O–C and COOH. The abundant surface groups enabled further carbonisation of the CDs, as well as granted good solubility in water. After 8 h reaction, the PL intensity became much stronger than that at 3 h, while the chemical groups changed a little.[399] The effect of reaction time on the QY is also investigated, which showed a volcano-shaped trend with the highest QY obtained at a 6 h reaction time.[413] Jiang and co-workers combined experimental and theoretical calculations on nitrogen-doped GQDs to study the formation mechanism. As the reaction proceeded, the size of the planar structure increased and a size change occurred from non-uniform to uniform. This phenomenon was explained by the stability of the different products: the less stable intermediate small fractions would decompose into the original precursor while the relatively stable N-doped graphene layers would grow at high temperature and pressure.[404] A different formation behaviour of CDs has been reported by Feldmann and co-workers using citric acid and ethylenediamine as the precursors. They have found that the CDs grew rapidly during the first 30 min and the size remained constant for the rest of the synthesis. Instead of growing in size, they undergo a substantial transformation of the internal structure, with larger aromatic domains and a higher level of graphitization, as seen in Fig. 34D. The PL QY decreases accordingly, with a shorter PL lifetime, which implies an increase in the nonradiative recombination process.[405]

6.3. Photo-related applications

By understanding the formation mechanism and controlling the reaction parameters to manipulate the optical properties of CDs, researchers have been pushing forward to utilize this material for practical applications. Due to their easy and cheap synthesis, low toxicity, high (aqueous) solubility, good optical properties with high fluorescence quantum yield, facile modification and stability against photobleaching, CDs made from HTC are superior to the traditional semiconductor quantum dots. Interesting facts about this material have been discovered from research over the past few years, which makes it a good candidate for various applications, such as bio-imaging, optronics, photocatalysis and photovoltaics. Our group has been working on applying CDs as sustainable alternatives for some hazardous materials in solar cells and photocatalysis. In an early report, biomass derived CDs have been used to sensitize ZnO nanorods to visible light, allowing their use in solid-state nanostructured solar cells.[389] The performance of the devices depended on the functional groups on the CD surface, and it is likely that the functionalisation determines the binding of CDs to the ZnO surface and the nature of the charge transportation and recombination. Later we further investigated the influence of functionalisation on solar cell performance.[415] Six types of CDs were produced from different precursors and used as sensitizers for TiO_2-based solar cells. By investigating the structural and optical properties of different CDs we have shown that the combination of amine and carboxylic acid groups is more beneficial for enhancing the solar cell performance. In a more recent work, chitosan derived CDs with nitrogen doping were studied as potential photocatalysts.[414] The CDs were covalently bonded on a conductive substrate and tested as a photoanode. As shown in Fig. 35, the CD electrode is capable of producing a photocurrent under visible light, owing to the visible light absorption, easily accessed energy states and good charge transfer ability, which can be used to sensitize other semiconductor photocatalysts or it can act as a photocatalyst itself to drive chemical reactions.

7. Summary and perspective

HTC represents a useful strategy for a variety of present-day applications. The high flexibility in reaction parameters, including the reaction time and temperature, plus the easiness in combining the feedstock with different catalysts, on the one hand, in order to enhance the valuable chemicals that can be found in the liquid phase and/or the hydrothermal carbon yield, or various templates, activators and/or heteroatom

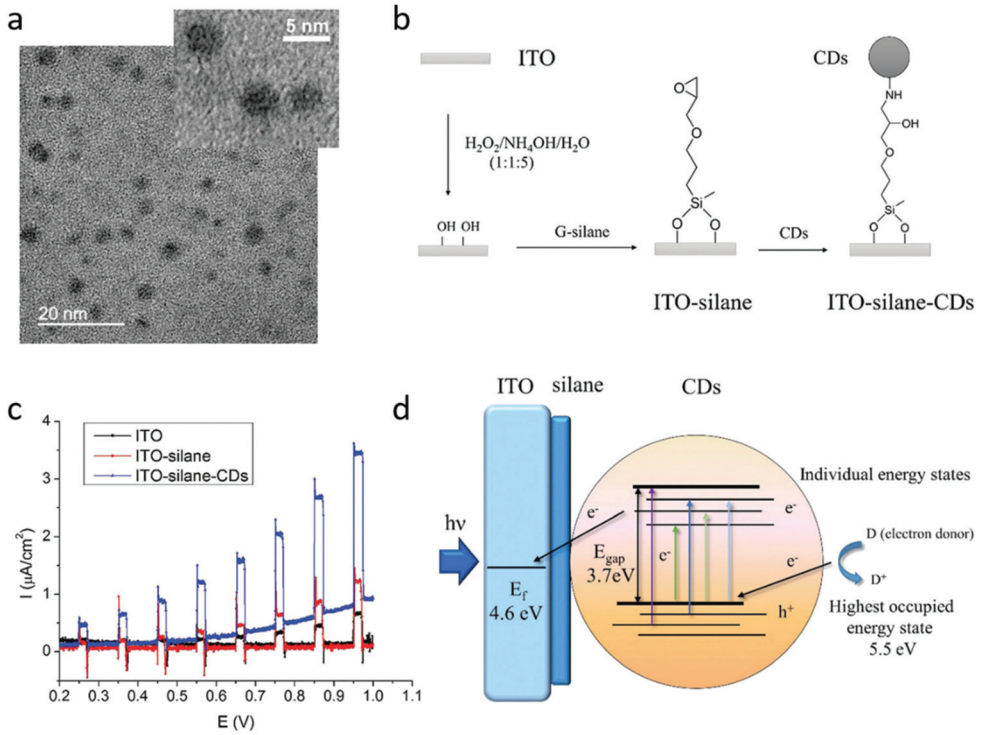

Fig. 35 (a) TEM images of as-prepared CDs; (b) fabrication of the CD electrode; (c) chopped photocurrent generation under visible light illumination and (d) the proposed reaction mechanism of CDs as the photocatalyst; reproduced with permission from ref. 414.

doping, on the other hand, in order to produce porous carbon structures decorated with functionalities, make the HTC one of the most used approaches, around the research world, when it comes to transforming waste into valuable products *via* a sustainable route.

As is summarised here, HTC can be used in degradation of biomass and biomass derivatives in three different products, such as liquid phase containing chemicals (5-HMF, levulinic acid, formic acid, and acetic acid), solid carbon materials and fluorescent carbons. Regarding the biomass decomposition and hydrothermal carbon formation, several mechanisms have been proposed and the main steps are hydrolysis, dehydration, polymerization, aromatization and nucleation. Many studies have been focused on the influence of the feedstock, reaction time and temperature on the materials properties and carbon yield, summarizing that as the reaction severity increases, compound solubilisation and volatilisation increase, decreasing the solid yields. Also, when the trends of many feedstocks were collectively investigated, it was observed that feedstock properties have a significant influence on the hydrothermal carbon yield. When it comes to the solid composition, it was observed that regardless of the biomass precursor, the resulting hydrothermal carbons contain between 4 and 6% hydrogen; meanwhile the oxygen content seems to be highly dependent on the precursor. Regarding their structural properties, the resulting powders consist mainly of nonporous spherical particles, with variation in sizes and shape depending on the starting material. The advantage of combining HTC with side strategies, such as templating methods (soft or hard templating) or chemical activation, results in the production of highly porous carbon structures characterised by their large specific surface area and large pore volume, as detailed in section 2. This is a great achievement for further involvement of these materials in environmental applications such as air depollution and water treatment or in energy storage applications, including Li-ion batteries and supercapacitors, as electrode materials. Carbon-based materials have superior cycling stability and rate capability, and so can be operated at higher charge and discharge rates and have much longer lifetimes. Moreover, the hierarchical pore structures enable ion mass transport, and therefore porous carbon is an important material for supercapacitor electrodes. Other applications of the HTC carbon include their usage as electrocatalysts in the ORR. Due to the easiness of combining the carbon precursor (biomass) with different chemicals, a wide range of heteroatom doped carbons can be synthesised *via* HTC, as discussed in section 3. The heteroatoms doped within the carbon matrix induce heteroatom–carbon bonds, and the polarisation of these bonds generates active sites on the adjacent carbon matrix resulting in a reduced energy barrier towards electrocatalysis. Simultaneously, the electrical conductivity is increased due to the higher concentration of delocalised electrons within the π-system. In addition, the HTC carbon powders can be successfully employed as a catalyst support as the tunability of

their surface polarity and area facilitates the anchoring of metal nanoparticles, which can then be used in different reactions.

Chemicals in the liquid phase such as 5-HMF, levulinic acid, formic acid, lactic acid and acetic acid, represent a huge opportunity as a source of bio-based materials and fuel additives. Their synthesis is strictly connected to that of hydrothermal carbons and therefore their joint production represents an added value. Of course, this opportunity comes with several challenges. Yields of conversion are still relatively poor, separation from reaction medium is difficult and corrosion risk due to highly acidic process water is high. All of these issues must be addressed to allow the successful transit of these processes to industrial scale production.

The newly discovered third product, carbon dots, holds great potential in many applications, especially in photocatalysis and photovoltaics. In section 6, the formation mechanism and the reaction parameters were discussed, giving guidance to future investigations on this intriguing material. Given the fact that HTC is an easy and low-cost process, and the CDs formed from this method show excellent bio-compatible and optical properties, producing high quality CDs with HTC to replace the traditional hazardous semiconductor quantum dots could be one of the future directions towards sustainability.

Overall, publications from the past few years show that HTC has been intensively researched and upgraded to be used in novel and up-to-date applications. Despite the fact that the process has been known since 100 years ago, this review reveals that the research community has high interest in HTC, and there are still gaps to be fulfilled and debates to be solved, in terms of the mechanism of carbon sphere formation and carbon quantum dot formation. Moreover, considerable attention should be devoted to upscaling the HTC process, especially related to the advanced materials production requiring advanced reactor design and process engineering. This includes also the energetic and techno-economic analysis along with their environmental impact at each life stage.

A great deal of fundamentals in HTC have already been understood but there is still a lack of details. For example, the mechanism of nucleation, the rate-limiting step, the kinetics of the reaction, and the mechanism of the reaction still remain ambiguous. Something that is not well understood so far is the role and influence of pressure during the HTC process and how the reaction mechanism/nucleation change in the presence of external gases, *i.e.* when the HTC process is run under an inert gas or CO_2. In addition, it is still not clear what dictates the formation of the amorphous HTC spheres and what dictates the formation of the carbon dots in solution. We assume that a gas phase reaction is involved in the formation of the carbon dots which is yet to be proved. To understand the missing fundamentals, *in situ*/*operando* characterisation using synchrotron facilities (Small Angle X-Ray/Neutron Diffraction and Pair Distribution Function) is crucial. In addition, on-line monitoring using NMR or HPLC-MS of the reaction products will be able to shed light on the formation mechanism of these challenging materials. Understanding the fundamentals will allow better control over the synthesis and upscaling of these materials. This is valid not only for the carbon dots, but also for the HTC materials, where still certain fundamental aspects such as nucleation, growth, aggregation, and the role of water remain to be elucidated and where *in operando* characterisation techniques during the HTC materials formation will play an important role in overcoming these major challenges.

Of crucial importance in the future, an area where not many scientific breakthroughs have been seen, is processing HTC materials. This could involve techniques such as electrospinning, electrowriting or 3D printing to create 3D architectures with tunable properties for a wide range of applications from energy storage to wearable electronics. Finally, new applications of these materials must be explored along with already emerging applications, with focus on energy and the environment.

New applications will emerge especially in the case of carbon dots, in particular in photocatalysis, biosensors and optoelectronic applications. Emerging applications of HTC in batteries and electrocatalysis will continue to rise. In particular, the development of multi-ion batteries based on dual carbon electrodes designed with the right configuration for both alkali metals and anion storage as well as other hybrid supercapacitor-battery systems will be crucial in the near future. These batteries could become compostable, whereby after the end of life, a battery containing no current collector but only carbon electrodes could be mixed with soil using the concept of Terra Pretta. In terms of electrocatalysis using HTC supports to anchor single atom sites or dimer sites to control the selectivity to various products, especially for oxygen, CO_2 and nitrogen, reaction will be crucial. Particularly promising will be the use of the resulting modified HTC materials as electrocatalysts to further convert the liquid chemicals from the aqueous phase into high end products and/or fuels. If we could create a circular process where the HTC products could be tailor made with the right electrochemical properties to be able to further catalyze under the application of an external bias the conversion of liquid phase chemicals such as HMF and LA into other valuable components, the economic value of the HTC process would increase.

Other applications of increasing importance will be based on using HTC adsorbents for critical metal recovery to recover metals of crucial economic importance from batteries, fuel cells, electrolysers, solar panels or wind turbines and facilitate the movement towards a circular economy.

Finally, clearer correlations, especially when using real biomass, must be made between the (bio)chemistry of the biomass precursor and the resulting carbon materials given that biomass is variable. For the production of advanced materials, it is desired that raw biomass is separated into pure components before being transformed by means of hydrothermal processes. For bioenergy, the biomass-final product characteristics must be understood and optimised to ensure reproducibility.

Life cycle assessment and life cycle costing along with a careful estimation of energy balances must become an integral part of future studies reporting either advanced materials production or biomass to bioenergy processes. Only then, we can ensure truly sustainable, environmentally benign and economically viable processes. So far almost none of the reports on HTC and products are accompanied by LCA; however this must change and become the new norm.

Conflicts of interest

There are no conflicts to declare.

References

1 F. Bergius and H. Specht, *Verlag Wilhelm Knapp, Halle der Saale, Ger*, 1913, p. 58.
2 E. Berl and A. Schmidt, *Justus Liebigs Ann. Chem.*, 1932, **493**, 97–123.
3 E. Berl and A. Schmidt, *Justus Liebigs Ann. Chem.*, 1932, **493**, 124–135.
4 E. Berl and A. Schmidt, *Justus Liebigs Ann. Chem.*, 1932, **493**, 135–152.
5 E. Berl and A. Schmidt, *Justus Liebigs Ann. Chem.*, 1932, **496**, 283–303.
6 Q. Wang, H. Li, L. Chen and X. Huang, *Carbon*, 2001, **39**, 2211–2214.
7 C. Falco, F. Perez Caballero, F. Babonneau, C. Gervais, G. Laurent, M.-M. Titirici and N. Baccile, *Langmuir*, 2011, **27**, 14460–14471.
8 C. Falco, N. Baccile and M.-M. Titirici, *Green Chem.*, 2011, **13**, 3273–3281.
9 C. Falco, J. P. Marco-Lozar, D. Salinas-Torres, E. Morallon, D. Cazorla-Amorós, M.-M. Titirici and D. Lozano-Castelló, *Carbon*, 2013, **62**, 346–355.
10 C. Falco, J. M. Sieben, N. Brun, M. Sevilla, T. der Mauelen, E. Morallón, D. Cazorla-Amorós and M.-M. Titirici, *ChemSusChem*, 2013, **6**, 374–382.
11 M.-M. Titirici, A. Thomas and M. Antonietti, *New J. Chem.*, 2007, **31**, 787–789.
12 M.-M. Titirici, A. Thomas and M. Antonietti, *J. Mater. Chem.*, 2007, **17**, 3412–3418.
13 M. Sevilla and A. B. Fuertes, *Chem. – Eur. J.*, 2009, **15**, 4195–4203.
14 L. Wang, Y. Chang and A. Li, *Renewable Sustainable Energy Rev.*, 2019, **108**, 423–440.
15 M.-M. M. Titirici and M. Antonietti, *Chem. Soc. Rev.*, 2010, **39**, 103–116.
16 T. Werpy and G. Petersen, Other Inf. PBD 1 Aug 2004, 2004, Medium: ED; Size: 76 pp.
17 S. Román, J. M. V. Nabais, C. Laginhas, B. Ledesma and J. F. González, *Fuel Process. Technol.*, 2012, **103**, 78–83.
18 A. Alvarez-Murillo, S. Roman, B. Ledesma and E. Sabio, *J. Anal. Appl. Pyrolysis*, 2015, **113**, 307–314.
19 J. A. Rice and P. MacCarthy, *Geoderma*, 1988, **43**, 65–73.
20 S. Sahu, B. Behera, T. K. Maiti and S. Mohapatra, *Chem. Commun.*, 2012, **48**, 8835.
21 Z. C. Yang, M. Wang, A. M. Yong, S. Y. Wong, X. H. Zhang, H. Tan, A. Y. Chang, X. Li and J. Wang, *Chem. Commun.*, 2011, **47**, 11615–11617.
22 X. T. Zheng, A. Ananthanarayanan, K. Q. Luo and P. Chen, *Small*, 2015, **11**, 1620–1636.
23 S. C. Ray, A. Saha, N. R. Jana and R. Sarkar, *J. Phys. Chem. C*, 2009, **113**, 18546–18551.
24 S. N. Baker and G. A. Baker, *Angew. Chem., Int. Ed.*, 2010, **49**, 6726–6744.
25 Y. Chen, Y. Wu, B. Weng, B. Wang and C. Li, *Sens. Actuators, B*, 2016, **223**, 689–696.
26 N. Wang, Y. Wang, T. Guo, T. Yang, M. Chen and J. Wang, *Biosens. Bioelectron.*, 2016, **85**, 68–75.
27 T. N. J. I. Edison, R. Atchudan, J. J. Shim, S. Kalimuthu, B. C. Ahn and Y. R. Lee, *J. Photochem. Photobiol., B*, 2016, **158**, 235–242.
28 J. Liao, Z. Cheng and L. Zhou, *ACS Sustainable Chem. Eng.*, 2016, **4**, 3053–3061.
29 M. Jahanbakhshi and B. Habibi, *Biosens. Bioelectron.*, 2016, **81**, 143–150.
30 J. Li, L. Zhang, P. Li, Y. Zhang and C. Dong, *Sens. Actuators, B*, 2018, **258**, 580–588.
31 Y. Guo, L. Yang, W. Li, X. Wang, Y. Shang and B. Li, *Microchim. Acta*, 2016, **183**, 1409–1416.
32 R. Atchudan, T. N. J. I. Edison, M. G. Sethuraman and Y. R. Lee, *Appl. Surf. Sci.*, 2016, **384**, 432–441.
33 H. Wikberg, T. Ohra-aho, F. Pileidis and M.-M. Titirici, *ACS Sustainable Chem. Eng.*, 2015, **3**, 2737–2745.
34 D. Kim, K. Lee and K. Y. Park, *J. Ind. Eng. Chem.*, 2016, **42**, 95–100.
35 E. Dinjus, A. Kruse and N. Tröger, *Chem. Eng. Technol.*, 2011, **34**, 2037–2043.
36 J. Lu, Z. Liu, Y. Zhang and P. E. Savage, *ACS Sustainable Chem. Eng.*, 2018, **6**, 14501–14509.
37 A. Funke and F. Ziegler, *Biofuels, Bioprod. Biorefin.*, 2010, **4**, 160–177.
38 F. Buendia-Kandia, G. Mauviel, E. Guedon, E. Rondags, D. Petitjean and A. Dufour, *Energy Fuels*, 2018, **32**(4), 4127–4138.
39 Y. Matsumura, M. Sasaki, K. Okuda, S. Takami, S. Ohara, M. Umetsu and T. Adschiri, *Combust. Sci. Technol.*, 2006, **178**, 509–536.
40 X. Yan, F. Jin, K. Tohji, T. Moriya and H. Enomoto, *J. Mater. Sci.*, 2007, **42**, 9995–9999.
41 X. Yan, F. Jin and K. Tohji, *AIChE J.*, 2010, **56**, 2727–2733.
42 F. Jin, Z. Zhou, H. Enomoto, T. Moriya and H. Higashijima, *Chem. Lett.*, 2004, **33**, 126–127.
43 B. Danon, G. Marcotullio and W. De Jong, *Green Chem.*, 2014, **16**, 39–54.
44 R. J. Van Putten, J. N. M. Soetedjo, E. A. Pidko, J. C. Van Der Waal, E. J. M. Hensen, E. De Jong and H. J. Heeres, *ChemSusChem*, 2013, **6**, 1681–1687.

45 N. Baccile, G. Laurent, F. Babonneau, F. Fayon, M.-M. Titirici and M. Antonietti, *J. Phys. Chem. C*, 2009, **113**, 9644–9654.
46 G. Yang, E. A. Pidko and E. J. M. Hensen, *J. Catal.*, 2012, **295**, 122–132.
47 D. Jung, M. Zimmermann and A. Kruse, *ACS Sustainable Chem. Eng.*, 2018, **6**, 13877–13887.
48 I. Van Zandvoort, E. J. Koers, M. Weingarth, P. C. A. Bruijnincx, M. Baldus and B. M. Weckhuysen, *Green Chem.*, 2015, **17**, 4383–4392.
49 A. B. Brown, B. J. McKeogh, G. A. Tompsett, R. Lewis, N. A. Deskins and M. T. Timko, *Carbon*, 2017, **125**, 614–629.
50 M. Sevilla and A. B. Fuertes, *Carbon*, 2009, **47**, 2281–2289.
51 G. Tsilomelekis, M. J. Orella, Z. Lin, Z. Cheng, W. Zheng, V. Nikolakis and D. G. Vlachos, *Green Chem.*, 2016, **18**, 1983–1993.
52 Y. Qi, B. Song and Y. Qi, *RSC Adv.*, 2016, **6**, 102428–102435.
53 Z. Cheng, J. Everhart, G. Tsilomelekis, V. Nikolakis, B. Saha and D. Vlachos, *Green Chem.*, 2018, **20**, 997–1006.
54 L. J. R. Higgins, A. P. Brown, J. P. Harrington, A. B. Ross, B. Kaulich and B. Mishra, *Carbon*, 2020, **161**, 423–431.
55 M. Titirici, M. Antonietti and N. Baccile, *Green Chem.*, 2008, **10**, 1204–1212.
56 A. J. Romero-Anaya, M. Ouzzine, M. A. Lillo-Ródenas and A. Linares-Solano, *Carbon*, 2014, **68**, 296–307.
57 Y. Yu and H. Wu, *Ind. Eng. Chem. Res.*, 2010, **49**, 3902–3909.
58 M. Li, W. Li and S. Liu, *Carbohydr. Res.*, 2011, **346**, 999–1004.
59 H. Simsir, N. Eltugral and S. Karagoz, *Bioresour. Technol.*, 2017, **246**, 82–87.
60 S.-M. Alatalo, E. Repo, E. Mäkilä, J. Salonen, E. Vakkilainen and M. Sillanpää, *Bioresour. Technol.*, 2013, **147**, 71–76.
61 L. Li, J. R. V. Flora, J. M. Caicedo and N. D. Berge, *Bioresour. Technol.*, 2015, **187**, 263–274.
62 S. Nizamuddin, H. A. Baloch, G. J. Griffin, N. M. Mubarak, A. W. Bhutto, R. Abro, S. A. Mazari and B. S. Ali, *Renewable Sustainable Energy Rev.*, 2017, **73**, 1289–1299.
63 I. Oliveira, D. Blöhse and H.-G. Ramke, *Bioresour. Technol.*, 2013, **142**, 138–146.
64 K. U. Suwelack, D. Wüst, P. Fleischmann and A. Kruse, *Biomass Convers. Biorefin.*, 2016, **6**, 151–160.
65 K. Suwelack, D. Wust, M. Zeller, A. Kruse and J. Krumpel, *Biomass Convers. Biorefin.*, 2016, **6**, 347–354.
66 H. P. Ruyter, *Fuel*, 1982, **61**, 1182–1187.
67 Y. Fu, J. Ye, J. Chang, H. Lou and X. Zheng, *Fuel*, 2016, **180**, 591–596.
68 D. Knežević, W. van Swaaij and S. Kersten, *Ind. Eng. Chem. Res.*, 2010, **49**, 104–112.
69 M. K. Akalın, K. Tekin and S. Karagoz, *Bioresour. Technol.*, 2012, **110**, 682–687.
70 D. Knežević, W. P. M. van Swaaij and S. R. A. Kersten, *Ind. Eng. Chem. Res.*, 2009, **48**, 4731–4743.
71 L. Li, R. Diederick, J. R. V. Flora and N. D. Berge, *Waste Manage.*, 2013, **33**, 2478–2492.
72 X. Lu and N. D. Berge, *Bioresour. Technol.*, 2014, **166**, 120–131.
73 K. Aydıncak, T. Yumak, A. Sınag and B. Esen, *Ind. Eng. Chem. Res.*, 2012, **51**, 9145–9152.
74 N. D. Berge, K. S. Ro, J. Mao and J. R. V. Flora, *Environ. Sci. Technol.*, 2011, **45**, 5696–5703.
75 S. Kang, X. Li, J. Fan and J. Chang, *Ind. Eng. Chem. Res.*, 2012, **51**, 9023–9031.
76 X. Lu, P. Pellechia, J. R. V. Flora and N. Berge, *Bioresour. Technol.*, 2013, **138**, 180–190.
77 S. S. Jamari and J. R. Howse, *Biomass Bioenergy*, 2012, **47**, 82–90.
78 X. Cao, K. S. Ro, M. Chappell, Y. Li and J. Mao, *Energy Fuels*, 2011, **25**, 388–397.
79 C. Areeprasert, P. Zhao, D. Ma, Y. Shen and K. Yoshikawa, *Energy Fuels*, 2014, **28**, 1198–1206.
80 M. Sevilla, G. A. Ferrero and A. B. Fuertes, *Carbon*, 2017, **114**, 50–58.
81 R. Azargohar, *Production of Activated Carbon and its Catalytic Application for Oxidation of Hydrogen Sulphide*, 2009.
82 E. Atanes, A. Nieto-Márquez, A. Cambra, M. C. Ruiz-Pérez and F. Fernández-Martínez, *Chem. Eng. J.*, 2012, **211–212**, 60–67.
83 K. V. Kumar, K. Preuss, L. Lu, Z. X. Guo and M. M. Titirici, *J. Phys. Chem. C*, 2015, **119**, 22310–22321.
84 M. A. Islam, A. Benhouria, M. Asif and B. H. Hameed, *J. Taiwan Inst. Chem. Eng.*, 2015, **52**, 57–64.
85 M. A. Islam, M. J. Ahmed, W. A. Khanday, M. Asif and B. H. Hameed, *J. Environ. Manage.*, 2017, **203**, 237–244.
86 P. P. Sharma, J. Wu, R. M. Yadav, M. Liu, C. J. Wright, C. S. Tiwary, B. I. Yakobson, J. Lou, P. M. Ajayan and X.-D. D. Zhou, *Angew. Chem., Int. Ed.*, 2015, **54**, 13701–13705.
87 H. Wang, J. Jia, P. Song, Q. Wang, D. Li, S. Min, C. Qian, L. Wang, Y. F. Li, C. Ma, T. Wu, J. Yuan, M. Antonietti and G. A. Ozin, *Angew. Chem., Int. Ed.*, 2017, **56**, 7847–7852.
88 G. W. Liu, T. Y. Chen, C. H. Chung, H. P. Lin and C. H. Hsu, *ACS Omega*, 2017, **2**, 2106–2113.
89 M.-M. M. Titirici, R. J. White, N. Brun, V. L. Budarin, D. S. Su, F. del Monte, J. H. Clark and M. J. MacLachlan, *Chem. Soc. Rev.*, 2015, **44**, 250–290.
90 S. Kubo, R. J. White, N. Yoshizawa, M. Antonietti and M. M. Titirici, *Chem. Mater.*, 2011, **23**, 4882–4885.
91 K. V. Kumar, S. Gadipelli, K. Preuss, H. Porwal, T. Zhao, Z. X. Guo and M. M. Titirici, *ChemSusChem*, 2017, **10**, 199–209.
92 M.-M. M. Titirici, R. J. White, C. Falco and M. Sevilla, *Energy Environ. Sci.*, 2012, **5**, 6796–6822.
93 Z. Zhang, M. Qin, B. Jia, H. Zhang, H. Wu and X. Qu, *Chem. Commun.*, 2017, **53**, 2922–2925.
94 P. W. Xiao, L. Zhao, Z. Y. Sui, M. Y. Xu and B. H. Han, *Microporous Mesoporous Mater.*, 2017, **253**, 215–222.
95 A. B. Fuertes and M. Sevilla, *Carbon*, 2015, **94**, 41–52.

96 P. W. Xiao, D. Guo, L. Zhao and B. H. Han, *Microporous Mesoporous Mater.*, 2016, **220**, 129–135.
97 L. Zhu, F. Shen, R. L. Smith and X. Qi, *Energy Technol.*, 2017, **5**, 452–460.
98 Y. Boyjoo, Y. Cheng, H. Zhong, H. Tian, J. Pan, V. K. Pareek, S. P. Jiang, J. F. Lamonier, M. Jaroniec and J. Liu, *Carbon*, 2017, **116**, 490–499.
99 Q.-P. Fabian, R.-R. Ramiro, M. Emilia and C.-A. Diego, *ChemPlusChem*, 2016, **81**, 1349–1359.
100 M. T. Gilbert, J. H. Knox and B. Kaur, *Chromatographia*, 1982, **16**, 138–146.
101 S. Kubo, R. Demir-Cakan, L. Zhao, R. J. White and M. M. Titirici, *ChemSusChem*, 2010, **3**, 188–194.
102 S. Z. Niu, S. Da Wu, W. Lu, Q. H. Yang and F. Y. Kang, *Xinxing Tan Cailiao/New Carbon Mater.*, 2017, **32**, 289–296.
103 C. Liang, K. Hong, G. A. Guiochon, J. W. Mays and S. Dai, *Angew. Chem., Int. Ed.*, 2004, **43**, 5785–5789.
104 Y. Zhang, L. Liu, B. Van Der Bruggen and F. Yang, *J. Mater. Chem. A*, 2017, **5**, 12673–12698.
105 T. Zhou, R. Ma, Y. Zhou, R. Xing, Q. Liu, Y. Zhu and J. Wang, *Microporous Mesoporous Mater.*, 2018, **261**, 88–97.
106 S. Wang, C. Han, J. Wang, J. Deng, M. Zhu, J. Yao, H. Li and Y. Wang, *Chem. Mater.*, 2014, **26**, 6872–6877.
107 S. A. Bagshaw, E. Prouzet, T. J. Pinnavaia, S. A. Bagshaw, E. Prouzet and T. J. Pinnavaia, *Science*, 1995, **269**, 1242–1244.
108 J. Texter, L. Zhao, P. W. Xiao, F. P. Caballero, B. H. Han and M. M. Titirici, *Carbon*, 2017, **112**, 117–129.
109 Suhas, V. K. Gupta, P. J. M. Carrott, R. Singh, M. Chaudhary and S. Kushwaha, *Bioresour. Technol.*, 2016, **216**, 1066–1076.
110 J. Deng, M. Li and Y. Wang, *Green Chem.*, 2016, **18**, 4824–4854.
111 Z. Liang, L. Zhang, H. Liu, J. Zeng, J. Zhou, H. Li and H. Xia, *Results Phys.*, 2019, **12**, 1984–1990.
112 J. Liu, L. Xie, Z. Wang, S. Mao, Y. Gong and Y. Wang, *Chem. Commun.*, 2019, **56**, 229–232.
113 L. Xie, Z. Wang, J. Liu, Y. Gong, S. Mao, G. Lü, X. Ma, L. Yu and Y. Wang, *Carbon*, 2019, **155**, 611–617.
114 C. Chen, H. Wang, C. Han, J. Deng, J. Wang, M. Li, M. Tang, H. Jin and Y. Wang, *J. Am. Chem. Soc.*, 2017, **139**, 2657–2663.
115 A. Chen, Y. Yu, Y. Zhang, W. Zang, Y. Yu, Y. Zhang, S. Shen and J. Zhang, *Carbon*, 2014, **80**, 19–27.
116 Q. Kong, L. Zhang, M. Wang, M. Li, H. Yao and J. Shi, *Sci. Bull.*, 2016, **61**, 1195–1201.
117 N. P. Stadie, S. Wang, K. V. Kravchyk and M. V. Kovalenko, *ACS Nano*, 2017, **11**, 1911–1919.
118 H. Nishihara and T. Kyotani, *Chem. Commun.*, 2018, **54**, 5648–5673.
119 B. Liu, H. Shioyama, T. Akita and Q. Xu, *J. Am. Chem. Soc.*, 2008, **130**, 5390–5391.
120 S. Dutta, A. Bhaumik and K. C.-W. Wu, *Energy Environ. Sci.*, 2014, **7**, 3574–3592.
121 L. P. Wang, W. S. Jia, X. F. Liu, J. Z. Li and M. M. Titirici, *J. Energy Chem.*, 2016, **25**, 566–570.
122 F. Rodríguez-Reinoso and M. Molina-Sabio, *Carbon*, 1992, **30**, 1111–1118.
123 J. Guo, Y. Luo, A. C. Lua, R.-A. Chi, Y.-L. Chen, X.-T. Bao and S.-X. Xiang, *Carbon*, 2007, **45**, 330–336.
124 J. Jin, S. Tanaka, Y. Egashira and N. Nishiyama, *Carbon*, 2010, **48**, 1985–1989.
125 X. Zhou, Z. Jia, A. Feng, X. Wang, J. Liu, M. Zhang, H. Cao and G. Wu, *Carbon*, 2019, **152**, 827–836.
126 M. Zhu, W. Cai, F. Verpoort and J. Zhou, *Chem. Eng. Res. Des.*, 2019, **146**, 130–140.
127 M. Sevilla, W. Gu, C. Falco, M. M. Titirici, A. B. Fuertes and G. Yushin, *J. Power Sources*, 2014, **267**, 26–32.
128 J. Li, H. Qi, Q. Wang, Z. Xu, Y. Liu, Q. Li, X. Kong and J. Huang, *Electrochim. Acta*, 2018, **271**, 92–102.
129 J. Shi, N. Yan, H. Cui, Y. Liu, Y. Weng, D. Li and X. Ji, *J. CO2 Util.*, 2017, **21**, 444–449.
130 F. Quesada-Plata, R. Ruiz-Rosas, E. Morallón and D. Cazorla-Amorós, *ChemPlusChem*, 2016, **81**, 1349–1359.
131 O. F. Cruz, J. Silvestre-albero, M. E. Casco, D. Hotza and C. R. Rambo, *Mater. Chem. Phys.*, 2018, **216**, 42–46.
132 X. Lu, C. Jiang, Y. Hu, H. Zhong, Y. Zhao, X. Xu and H. Liu, *J. Appl. Electrochem.*, 2018, **48**, 233–241.
133 C. Rodríguez Correa, C. Ngamying, D. Klank and A. Kruse, *Biomass Convers. Biorefin.*, 2018, **8**, 317–328.
134 X. Zhang, Y. Zhong, X. Xia, Y. Xia, D. Wang, C. Zhou, W. Tang, X. Wang, J. B. Wu and J. Tu, *ACS Appl. Mater. Interfaces*, 2018, **10**, 13598–13605.
135 M. Sevilla, W. Sangchoom, N. Balahmar, A. B. Fuertes and R. Mokaya, *ACS Sustainable Chem. Eng.*, 2016, **4**, 4710–4716.
136 K. Preuss, L. C. Tănase, C. M. Teodorescu, I. Abrahams and M. M. Titirici, *J. Mater. Chem. A*, 2017, **5**, 16336–16343.
137 L. S. Panchakarla, A. Govindaraj and C. N. R. Rao, *Inorg. Chim. Acta*, 2010, **363**, 4163–4174.
138 A. Kalijadis, J. DorCevidć, T. Trtić-Petrović, M. Vukčević, M. Popović, V. Maksimović, Z. Rakočević and Z. Laušević, *Carbon*, 2015, **95**, 42–50.
139 J. Wu, J. Hu, K. Song, J. Xu and H. Gao, *J. Alloys Compd.*, 2017, **704**, 1–6.
140 W. Ma, L. Xie, L. Dai, G. Sun, J. Chen, F. Su, Y. Cao, H. Lei, Q. Kong and C. M. Chen, *Electrochim. Acta*, 2018, **266**, 420–430.
141 B. Ashourirad, A. K. Sekizkardes, S. Altarawneh and H. M. El-Kaderi, *Chem. Mater.*, 2015, **27**, 1349–1358.
142 E. Antolini, *Renewable Sustainable Energy Rev.*, 2016, **58**, 34–51.
143 O. S. G. P. Soares, R. P. Rocha, A. G. Gonçalves, J. L. Figueiredo, J. J. M. Órfão and M. F. R. Pereira, *Appl. Catal., B*, 2016, **192**, 296–303.
144 L. Wang, Y. Wang, M. Wu, Z. Wei, C. Cui, M. Mao, J. Zhang, X. Han, Q. Liu and J. Ma, *Small*, 2018, **1800737**, 1800737.
145 K. Sharma, D. Hui, N. H. Kim and J. H. Lee, *Nanoscale*, 2019, **11**, 1205–1216.

146 A. Zhang, S. Cao, Y. Zhao, C. Zhang and A. Chen, *New J. Chem.*, 2018, **42**, 6903–6909.
147 A. Sarapuu, E. Kibena-Põldsepp, M. Borghei and K. Tammeveski, *J. Mater. Chem. A*, 2018, **6**, 776–804.
148 M. Borghei, N. Laocharoen, E. Kibena-Põldsepp, L. S. Johansson, J. Campbell, E. Kauppinen, K. Tammeveski and O. J. Rojas, *Appl. Catal., B*, 2017, **204**, 394–402.
149 Y. Song, G. Liu and Z.-Y. Y. Yuan, *RSC Adv.*, 2016, **6**, 94636–94642.
150 T. Berthold, C. R. Castro, M. Winter, G. Hoerpel, M. Kurttepeli, S. Bals, M. Antonietti and N. Fechler, *ChemNanoMat*, 2017, **3**, 311–318.
151 A. L. Yaumi, M. Z. A. Bakar and B. H. Hameed, *Energy*, 2018, **155**, 46–55.
152 W. He, P. Xue, H. Du, L. Xu, M. Pang, X. Gao, J. Yu, Z. Zhang and T. Huang, *Int. J. Hydrogen Energy*, 2017, **42**, 4123–4132.
153 F. Liu, Y. Gao, C. Zhang, H. Huang, C. Yan, X. Chu, Z. Xu, Z. Wang, H. Zhang, X. Xiao and W. Yang, *J. Colloid Interface Sci.*, 2019, **548**, 322–332.
154 Q. Wu, G. Zhang, M. Gao, L. Huang, L. Li, S. Liu, C. Xie, Y. Zhang and S. Yu, *J. Alloys Compd.*, 2019, **786**, 826–838.
155 F. Schipper, S. Kubo and T. P. Fellinger, *J. Sol-Gel Sci. Technol.*, 2019, **89**, 101–110.
156 W. Zhang, Z. Ren, Z. Ying, X. Liu and H. Wan, *J. Alloys Compd.*, 2018, **743**, 44–51.
157 M. Ren, Z. Jia, Z. Tian, D. Lopez, J. Cai, M. M. Titirici and A. B. Jorge, *ChemElectroChem*, 2018, **5**, 2686–2693.
158 M. Qiao, S. S. Meysami, G. A. Ferrero, F. Xie, H. Meng, N. Grobert and M. M. Titirici, *Adv. Funct. Mater.*, 2017, **1707284**, 1–7.
159 S. M. Alatalo, K. Qiu, K. Preuss, A. Marinovic, M. Sevilla, M. Sillanpää, X. Guo and M. M. Titirici, *Carbon*, 2016, **96**, 622–630.
160 R. Atchudan, T. N. J. I. Edison, S. Perumal and Y. R. Lee, *Appl. Surf. Sci.*, 2017, **393**, 276–286.
161 G. Huang, Y. Wang, T. Zhang, X. Wu and J. Cai, *J. Taiwan Inst. Chem. Eng.*, 2019, **96**, 672–680.
162 K. G. Latham, W. M. Dose, J. A. Allen and S. W. Donne, *Carbon*, 2018, **128**, 179–190.
163 L. Rao, R. Ma, S. Liu, L. Wang, Z. Wu, J. Yang and X. Hu, *Chem. Eng. J.*, 2019, **362**, 794–801.
164 F. C. de Oliveira, J. S. dos R. Coimbra, E. B. de Oliveira, A. D. G. Zuñiga and E. E. G. Rojas, *Crit. Rev. Food Sci. Nutr.*, 2016, **56**, 1108–1125.
165 X. Ma, G. Ning, Y. Wang, X. Song, Z. Xiao, L. Hou, W. Yang, J. Gao and Y. Li, *Electrochim. Acta*, 2018, **269**, 83–92.
166 A. Elmouwahidi, J. Castelo-Quibén, J. F. Vivo-Vilches, A. F. Pérez-Cadenas, F. J. Maldonado-Hódar and F. Carrasco-Marín, *Chem. Eng. J.*, 2018, **334**, 1835–1841.
167 K. Anoop Krishnan, K. G. Sreejalekshmi, V. Vimexen and V. V. Dev, *Ecotoxicol. Environ. Saf.*, 2016, **124**, 418–425.
168 L. Roldán, Y. Marco and E. García-Bordejé, *Microporous Mesoporous Mater.*, 2016, **222**, 55–62.
169 S. M. Alatalo, E. Mäkilä, E. Repo, M. Heinonen, J. Salonen, E. Kukk, M. Sillanpää and M. M. Titirici, *Green Chem.*, 2016, **18**, 1137–1146.
170 S. S. Zhang, *Inorg. Chem. Front.*, 2015, **2**, 1059–1069.
171 M. Y. Emran, M. A. Shenashen, A. A. Abdelwahab, M. Abdelmottaleb and S. A. El-Safty, *New J. Chem.*, 2018, **42**, 5037–5044.
172 L. Roldán, L. Truong-Phuoc, A. Ansón-Casaos, C. Pham-Huu and E. García-Bordejé, *Catal. Today*, 2018, **301**, 2–10.
173 M. H. Yeh, Y. S. Li, G. L. Chen, L. Y. Lin, T. J. Li, H. M. Chuang, C. Y. Hsieh, S. C. Lo, W. H. Chiang and K. C. Ho, *Electrochim. Acta*, 2015, **172**, 52–60.
174 M. H. Yeh, Y. A. Leu, W. H. Chiang, Y. S. Li, G. L. Chen, T. J. Li, L. Y. Chang, L. Y. Lin, J. J. Lin and K. C. Ho, *J. Power Sources*, 2018, **375**, 29–36.
175 J. Jiang, P. Nie, S. Fang, Y. Zhang, Y. An, R. Fu, H. Dou and X. Zhang, *Chin. Chem. Lett.*, 2018, **29**, 624–628.
176 L. Sun, Y. Fu, C. Tian, Y. Yang, L. Wang, J. Yin, J. Ma, R. Wang and H. Fu, *ChemSusChem*, 2014, **7**, 1637–1646.
177 Y. Li, Z. Wang, L. Li, S. Peng, L. Zhang, M. Srinivasan and S. Ramakrishna, *Carbon*, 2016, **99**, 556–563.
178 J. Wu, C. Jin, Z. Yang, J. Tian and R. Yang, *Carbon*, 2015, **82**, 562–571.
179 M. Q. Guo, J. Q. Huang, X. Y. Kong, H. J. Peng, H. Shui, F. Y. Qian, L. Zhu, W. C. Zhu and Q. Zhang, *Xinxing Tan Cailiao/New Carbon Mater.*, 2016, **31**, 352–362.
180 R. C. Bansai and M. Goyal, *Activated Carbon Adsorption*, CRC Press, Boca Raton, 2005.
181 F. Y. Chang, K. J. Chao, H. H. Cheng and C. S. Tan, *Sep. Purif. Technol.*, 2009, **70**, 87–95.
182 H. Marsh and F. Rodríguez-Reinoso, *Characterization of Activated Carbon*, 2006.
183 T. Gupta, *Carbon Black, Gray Transparent*, 2017, pp. 1–319.
184 C. Laginhas, J. M. V. Nabais and M. M. Titirici, *Microporous Mesoporous Mater.*, 2016, **226**, 125–132.
185 P. Zheng, T. Liu, X. Yuan, L. Zhang, Y. Liu, J. Huang and S. Guo, *Sci. Rep.*, 2016, **6**, 1–9.
186 E. Hao, W. Liu, S. Liu, Y. Zhang, H. Wang, S. Chen, F. Cheng, S. Zhao and H. Yang, *J. Mater. Chem. A*, 2017, **5**, 2204–2214.
187 M. Imtiaz, C. Zhu, Y. Li, M. S. Pak, I. Zada, S. W. Bokhari, Z. Chen, D. Zhang and S. Zhu, *J. Alloys Compd.*, 2017, **724**, 296–305.
188 P. Zheng, T. Liu, J. Zhang, L. Zhang, Y. Liu, J. Huang and S. Guo, *RSC Adv.*, 2015, **5**, 40737–40741.
189 W. Li, J. Huang, L. Feng, L. Cao, Y. Ren, R. Li, Z. Xu, J. Li and C. Yao, *J. Alloys Compd.*, 2017, **716**, 210–219.
190 H. Wang, W. Yu, J. Shi, N. Mao, S. Chen and W. Liu, *Electrochim. Acta*, 2016, **188**, 103–110.
191 E. Demir, M. Aydin, A. A. Arie and R. Demir-Cakan, *J. Alloys Compd.*, 2019, **788**, 1093–1102.
192 L. Ma, B. Zhao, X. Wang, J. Yang, X. Zhang, Y. Zhou and J. Chen, *ACS Appl. Mater. Interfaces*, 2018, **10**, 22067–22073.

193 J. Wang, L. Yan, Q. Ren, L. Fan, F. Zhang and Z. Shi, *Electrochim. Acta*, 2018, **291**, 188–196.
194 R. Väli, A. Jänes, T. Thomberg and E. Lust, *J. Electrochem. Soc.*, 2016, **163**, A1619–A1626.
195 H. Tang, M. Wang, T. Lu and L. Pan, *Ceram. Int.*, 2017, **43**, 4475–4482.
196 Z. Jian, S. Hwang, Z. Li, A. S. Hernandez, X. Wang, Z. Xing, D. Su and X. Ji, *Adv. Funct. Mater.*, 2017, **27**, 1–6.
197 Y. Li, S. Xu, X. Wu, J. Yu, Y. Wang, Y. S. Hu, H. Li, L. Chen and X. Huang, *J. Mater. Chem. A*, 2015, **3**, 71–77.
198 L. Yin, Y. Wang, C. Han, Y. M. Kang, X. Ma, H. Xie and M. Wu, *J. Power Sources*, 2016, **305**, 156–160.
199 R. Li, J. Huang, Z. Xu, H. Qi, L. Cao, Y. Liu, W. Li and J. Li, *Energy Technol.*, 2018, **6**, 1080–1087.
200 H.-L. Wang, Z.-Q. Shi, J. Jin, C.-B. Chong and C.-Y. Wang, *J. Electroanal. Chem.*, 2015, **755**, 87–91.
201 S. Jeong, X. Li, J. Zheng, P. Yan, R. Cao, H. J. Jung, C. Wang, J. Liu and J. G. Zhang, *J. Power Sources*, 2016, **329**, 323–329.
202 J.-S. Choi, H.-J. Lee, J.-K. Ha and K.-K. Cho, *J. Nanosci. Nanotechnol.*, 2018, **18**, 6459–6462.
203 S. Y. Son, S.-A. Hong, S. Y. Oh, Y.-C. Lee, G.-W. Lee, J. W. Kang, Y. S. Huh and I. T. Kim, *J. Nanosci. Nanotechnol.*, 2018, **18**, 6463–6468.
204 Q. Zhang, Q. Gao, W. Qian, H. Zhang, Y. Tan, W. Tian, Z. Li and H. Xiao, *J. Mater. Chem. A*, 2017, **5**, 19136–19142.
205 L. Wang, J. Yuan, Q. Zhao, Z. Wang, Y. Zhu, X. Ma and C. Cao, *Electrochim. Acta*, 2019, **308**, 174–184.
206 Z. Chen, D. Yin and M. Zhang, *Small*, 2018, **14**, 1–9.
207 Y. Guo, Y. Zhang, Y. Wang, D. Zhang, Y. Lu, R. Luo, Y. Wang, X. Liu, J. K. Kim and Y. Luo, *Electrochim. Acta*, 2019, **296**, 989–998.
208 X. Li, Y. Yang, J. Liu, L. Ouyang, J. Liu, R. Hu, L. Yang and M. Zhu, *Appl. Surf. Sci.*, 2017, **413**, 169–174.
209 S. Bao, S.-H. Luo, S.-X. Yan, Z.-Y. Wang, Q. Wang, J. Feng, Y.-L. Wang and T.-F. Yi, *Electrochim. Acta*, 2019, **307**, 293–301.
210 W. ur Rehman, Y. Xu, X. Du, X. Sun, I. Ullah, Y. Zhang, Y. Jin, B. Zhang and X. Li, *Appl. Surf. Sci.*, 2018, **445**, 359–367.
211 Z. Xiao, G. Ning, Z. Yu, C. Qi, L. Zhao, Y. Li, X. Ma and Y. Li, *Nanoscale*, 2019, **11**, 8270–8280.
212 C. Deng, S. Zhang and Y. Wu, *Nanoscale*, 2015, **7**, 487–491.
213 V. Palomares, M. Blas, P. Serras, A. Iturrondobeitia, A. Peña, A. Lopez-Urionabarrenechea, L. Lezama and T. Rojo, *ACS Sustainable Chem. Eng.*, 2018, **6**, 16386–16398.
214 J. Ding, H. Wang, Z. Li, K. Cui, D. Karpuzov, X. Tan, A. Kohandehghan and D. Mitlin, *Energy Environ. Sci.*, 2015, **8**, 941–955.
215 H. Lu and X. S. Zhao, *Sustainable Energy Fuels*, 2017, **1**, 1265–1281.
216 D. Salinas-Torres, D. Lozano-Castelló, M. M. Titirici, L. Zhao, L. Yu, E. Morallón and D. Cazorla-Amoros, *J. Mater. Chem. A*, 2015, **3**, 15558–15567.
217 Y. Wang, R. Yang, M. Li and Z. Zhao, *Ind. Crops Prod.*, 2015, **65**, 216–226.
218 Y. Liu, B. Huang, X. Lin and Z. Xie, *J. Mater. Chem. A*, 2017, **5**, 13009–13018.
219 T. Wei, X. Wei, Y. Gao and H. Li, *Electrochim. Acta*, 2015, **169**, 186–194.
220 L. Zhang, T. You, T. Zhou, X. Zhou and F. Xu, *ACS Appl. Mater. Interfaces*, 2016, **8**, 13918–13925.
221 C. Li, D. He, Z.-H. Huang and M.-X. Wang, *J. Electrochem. Soc.*, 2018, **165**, A3334–A3341.
222 K. K. Lee, W. Hao, M. Gustafsson, C. W. Tai, D. Morin, E. Björkman, M. Lilliestråle, F. Björefors, A. M. Andersson and N. Hedin, *RSC Adv.*, 2016, **6**, 110629–110641.
223 M. Härmas, T. Thomberg, T. Romann, A. Jänes and E. Lust, *J. Electrochem. Soc.*, 2017, **164**, A1866–A1872.
224 W. Du, X. Wang, J. Zhan, X. Sun, L. Kang, F. Jiang, X. Zhang, Q. Shao, M. Dong, H. Liu, V. Murugadoss and Z. Guo, *Electrochim. Acta*, 2019, **296**, 907–915.
225 Y. Zhao, X. He, R. Chen, Q. Liu, J. Liu, J. Yu, J. Li, H. Zhang, H. Dong, M. Zhang and J. Wang, *Chem. Eng. J.*, 2018, **352**, 29–38.
226 B. Kirubasankar, V. Murugadoss, J. Lin, T. Ding, M. Dong, H. Liu, J. Zhang, T. Li, N. Wang, Z. Guo and S. Angaiah, *Nanoscale*, 2018, **10**, 20414–20425.
227 Y. Q. Zhao, M. Lu, P. Y. Tao, Y. J. Zhang, X. T. Gong, Z. Yang, G. Q. Zhang and H. L. Li, *J. Power Sources*, 2016, **307**, 391–400.
228 W. Ye, X. Li, J. Luo, X. Wang and R. Sun, *Ind. Crops Prod.*, 2017, **109**, 410–419.
229 M. Enterría, F. J. Martín-Jimeno, F. Suárez-García, J. I. Paredes, M. F. R. Pereira, J. I. Martins, A. Martínez-Alonso, J. M. D. Tascón and J. L. Figueiredo, *Carbon*, 2016, **105**, 474–483.
230 F. Barzegar, A. Bello, O. O. Fashedemi, J. K. Dangbegnon, D. Y. Momodu, F. Taghizadeh and N. Manyala, *Electrochim. Acta*, 2015, **180**, 442–450.
231 Y. Wang and L. Jiang, *ACS Sustainable Chem. Eng.*, 2017, **5**, 5588–5597.
232 Z. W. She, J. Kibsgaard, C. F. Dickens, I. Chorkendorff, J. K. Nørskov and T. F. Jaramillo, *Science*, 2017, **355**(6321), eaad4998.
233 C. Tang, M. M. Titirici and Q. Zhang, *J. Energy Chem.*, 2017, **26**, 1077–1093.
234 F. Cao, M. Zhao, Y. Yu, B. Chen, Y. Huang, J. Yang, X. Cao, Q. Lu, X. Zhang, Z. Zhang, C. Tan and H. Zhang, *J. Am. Chem. Soc.*, 2016, **138**, 6924–6927.
235 Y. Lu, L. Wang, K. Preuß, M. Qiao, M. M. Titirici, J. Varcoe and Q. Cai, *J. Power Sources*, 2017, **372**, 82–90.
236 H. Yu, L. Shang, T. Bian, R. Shi, G. I. N. Waterhouse, Y. Zhao, C. Zhou, L.-Z. Wu, C.-H. Tung and T. Zhang, *Adv. Mater.*, 2016, **28**, 5140–5140.
237 M. Qiao, C. Tang, G. He, K. Qiu, R. Binions, I. P. Parkin, Q. Zhang, Z. Guo and M. M. Titirici, *J. Mater. Chem. A*, 2016, **4**, 12658–12666.
238 K. Preuss, M. Qiao and M. Titrici, Hydrothermal Carbon Materials for the Oxygen Reduction Reaction,

in *Carbon-Based Metal-Free Catalysts*, ed. L. Dai, Wiley, 2018, vol. 2, pp. 369–401.
239 W. Wan, Q. Wang, L. Zhang, H. W. Liang, P. Chen and S. H. Yu, *J. Mater. Chem. A*, 2016, **4**, 8602–8609.
240 K. Preuss, A. M. Siwoniku, C. I. Bucur and M.-M. Titirici, *ChemPlusChem*, 2019, **84**, 457–464.
241 G. He, M. Qiao, W. Li, Y. Lu, T. Zhao, R. Zou, B. Li, J. A. Darr, J. Hu, M. M. Titirici and I. P. Parkin, *Adv. Sci.*, 2017, **4**, 1600214.
242 B. Huang, Y. Liu and Z. Xie, *J. Mater. Chem. A*, 2017, **5**, 23481–23488.
243 Y. Cheng, K. Pang, X. Wu, Z. Zhang, X. Xu, J. Ren, W. Huang and R. Song, *ACS Sustainable Chem. Eng.*, 2018, **6**, 8688–8696.
244 L. Zhang, T. Wang, L. Sun, Y. Sun, T. Hu, K. Xu and F. Ma, *J. Mater. Chem. A*, 2017, **5**, 19752–19759.
245 D. Huang, S. Li, X. Zhang, Y. Luo, J. Xiao and H. Chen, *Carbon*, 2018, **129**, 468–475.
246 S. H. Bae, J. E. Kim, H. Randriamahazaka, S. Y. Moon, J. Y. Park and I. K. Oh, *Adv. Energy Mater.*, 2017, **7**, 1–11.
247 F. Li, L. Chen, G. P. Knowles, D. R. MacFarlane and J. Zhang, *Angew. Chem., Int. Ed.*, 2017, **56**, 505–509.
248 S.-H. H. Bae, J.-E. E. Kim, H. Randriamahazaka, S.-Y. Y. Moon, J.-Y. Y. Park and I.-K. K. Oh, *Adv. Energy Mater.*, 2017, **7**, 1601492.
249 L. Roldán, E. Pires, J. M. Fraile and E. García-Bordejé, *Catal. Today*, 2015, **249**, 153–160.
250 D. R. Lathiya, D. V. Bhatt and K. C. Maheria, *Bioresour. Technol. Rep.*, 2018, **2**, 69–76.
251 Z.-E. Tang, S. Lim, Y.-L. Pang, H.-C. Ong and K.-T. Lee, *Renewable Sustainable Energy Rev.*, 2018, **92**, 235–253.
252 C. De La Calle, J. M. Fraile, E. García-Bordejé, E. Pires and L. Roldán, *Catal. Sci. Technol.*, 2015, 1–7.
253 S. Kang and J. Yu, *Sugar Technol.*, 2018, **20**, 182–193.
254 F. D. Pileidis, M. Tabassum, S. Coutts, M. M. Ttitirici and M.-M. Titirici, *Cuihua Xuebao/Chin. J. Catal.*, 2014, **35**, 929–936.
255 J. M. Fraile, E. García-Bordejé, E. Pires and L. Roldán, *Carbon*, 2014, **77**, 1157–1167.
256 I. F. Nata, M. D. Putra, C. Irawan and C.-K. Lee, *J. Environ. Chem. Eng.*, 2017, **5**, 2171–2175.
257 X. Qi, N. Liu and Y. Lian, *RSC Adv.*, 2015, **5**, 17526–17531.
258 Y. Yan, Y. Dai, S. Wang, X. Jia, H. Yu and Y. Yang, *Appl. Catal., B*, 2016, **184**, 104–118.
259 J. Chen, J. Zhang, W. Sun, K. Song, D. Zhu and T. Li, *Appl. Organomet. Chem.*, 2017, **32**, 3.
260 A. Eiad-ua, B. Jomhataikool, W. Gunpum, N. Viriya-empikul and K. Faungnawakij, *Mater. Today: Proc.*, 2017, **4**, 6153–6158.
261 J. Liu, N. Wickramaratne, S. Qiao, *et al.*, *Nat. Mater.*, 2015, **14**, 763–774.
262 C. Gai, F. Zhang, T. Yang, Z. Liu, W. Jiao, N. Peng, T. Liu, Q. Lang and Y. Xia, *Green Chem.*, 2018, **20**, 2788–2800.
263 P. Wataniyakul, P. Boonnoun, A. T. Quitain, M. Sasaki, T. Kida, N. Laosiripojana and A. Shotipruk, *Catal. Commun.*, 2018, **104**, 41–47.
264 Y. M. Lu, H. Z. Zhu, W. G. Li, B. Hu and S. H. Yu, *J. Mater. Chem. A*, 2013, **1**, 3783–3788.
265 S. P. Dubey, A. D. Dwivedi, I.-C. Kim, M. Sillanpaa, Y.-N. Kwon and C. Lee, *Chem. Eng. J.*, 2014, **244**, 160–167.
266 J. Cheng, Y. Wang, C. Teng, Y. Shang, L. Ren and B. Jiang, *Chem. Eng. J.*, 2014, **242**, 285–293.
267 Z. Sun, J. Yang, J. Wang, W. Li, S. Kaliaguine, X. Hou, Y. Deng and D. Zhao, *J. Mater. Chem. A*, 2014, **2**, 6071–6074.
268 J. Yu, L. Yan, G. Tu, C. Xu, X. Ye, Y. Zhong, W. Zhu and Q. Xiao, *Catal. Lett.*, 2014, **144**, 2065–2070.
269 F. Zhang, H. Hu, H. Zhong, N. Yan and Q. Chen, *Dalton Trans.*, 2014, **43**, 6041.
270 B. He, Q. Zhao, Z. Zeng, X. Wang and S. Han, *J. Mater. Sci.*, 2015, **50**, 6339–6348.
271 Z. Q. Shi, L. X. Jiao, J. Sun, Z. B. Chen, Y. Z. Chen, X. H. Zhu, J. H. Zhou, X. C. Zhou, X. Z. Li and R. Li, *RSC Adv.*, 2014, **4**, 47–53.
272 K. Huang, J. Liu, L. Wang, G. Chang, R. Wang, M. Lei, Y. Wang and Y. He, *Appl. Surf. Sci.*, 2019, **487**, 1145–1151.
273 G. Singh, K. S. Lakhi, I. Y. Kim, S. Kim, P. Srivastava, R. Naidu and A. Vinu, *ACS Appl. Mater. Interfaces*, 2017, **9**, 29782–29793.
274 M. Liu, Y. Pang, B. Zhang, P. De Luna, O. Voznyy, J. Xu, X. Zheng, C. T. Dinh, F. Fan, C. Cao, F. P. G. De Arquer, T. S. Safaei, A. Mepham, A. Klinkova, E. Kumacheva, T. Filleter, D. Sinton, S. O. Kelley and E. H. Sargent, *Nature*, 2016, **537**, 382–386.
275 N. Querejeta, M. V. Gil, C. Pevida and T. A. Centeno, *J. CO2 Util.*, 2018, **26**, 1–7.
276 S. Sethupathi, M. Zhang, A. U. Rajapaksha, S. S. R. Lee, N. M. Nor, A. R. Mohamed, M. Al-Wabel, S. S. R. Lee and Y. S. Ok, *Sustainability*, 2017, **9**, 1–10.
277 M. C. Castrillon, K. O. Moura, C. A. Alves, M. Bastos-Neto, D. C. S. Azevedo, J. Hofmann, J. Möllmer, W. D. Einicke and R. Gläser, *Energy Fuels*, 2016, **30**, 9596–9604.
278 D. Y. C. Leung, G. Caramanna and M. M. Maroto-Valer, *Renewable Sustainable Energy Rev.*, 2014, **39**, 426–443.
279 L. Rao, R. Ma, S. Liu, L. Wang, Z. Wu, J. Yang and X. Hu, *Nitrogen enriched porous carbons from D-glucose with excellent CO 2 capture performance*, Elsevier B.V., 2019.
280 G. Shang, Q. Li, L. Liu, P. Chen and X. Huang, *J. Air Waste Manage. Assoc.*, 2016, **66**, 8–16.
281 M. I. Inyang, B. Gao, Y. Yao, Y. Xue, A. Zimmerman, A. Mosa, P. Pullammanappallil, Y. S. Ok and X. Cao, *Crit. Rev. Environ. Sci. Technol.*, 2016, **46**, 406–433.
282 X. He, K. B. Male, P. N. Nesterenko, D. Brabazon, B. Paull and J. H. T. Luong, *ACS Appl. Mater. Interfaces*, 2013, **5**, 8796–8804.
283 M. A. Islam, I. A. W. Tan, A. Benhouria, M. Asif and B. H. Hameed, *Chem. Eng. J.*, 2015, **270**, 187–195.
284 T. Xiong, X. Yuan, X. Chen, Z. Wu, H. Wang, L. Leng, H. Wang, L. Jiang and G. Zeng, *Appl. Surf. Sci.*, 2018, **427**, 1107–1117.

285 X. F. Yu, Y. H. Liu, Z. W. Zhou, G. X. Xiong, X. H. Cao, M. Li and Z.-B. Zhang, *J. Radioanal. Nucl. Chem.*, 2014, **300**, 1235–1244.
286 K. Sun, J. Tang, Y. Gong and H. Zhang, *Environ. Sci. Pollut. Res.*, 2015, **22**, 16640–16651.
287 H. Cai, X. Lin, L. Tian and X. Luo, *Ind. Eng. Chem. Res.*, 2016, **55**, 9648–9656.
288 L. Han, H. Sun, K. S. Ro, K. Sun, J. A. Libra and B. Xing, *Bioresour. Technol.*, 2017, **234**, 77–85.
289 J. Lu, F. Fu, Z. Ding, N. Li and B. Tang, *J. Hazard. Mater.*, 2017, **330**, 93–104.
290 B. Han, E. Zhang, G. Cheng, L. Zhang, D. Wang and X. Wang, *Chem. Eng. J.*, 2018, **338**, 734–744.
291 Z. Zheng, Y. Wang, W. Zhao, G. Xiong, X. Cao, Y. Dai, Z. Le, S. Yu, Z. Zhang and Y. Liu, *J. Radioanal. Nucl. Chem.*, 2017, **312**, 187–198.
292 G. Deng, Y. Zhang, X. Luo and J. Yang, *Appl. Organomet. Chem.*, 2018, e4473.
293 P. Biller and A. B. Ross, *Biofuels*, 2012, **3**, 603–623.
294 S. M. Heilmann, L. R. Jader, L. A. Harned, M. J. Sadowsky, F. J. Schendel, P. A. Lefebvre, M. G. von Keitz and K. J. Valentas, *Appl. Energy*, 2011, **88**, 3286–3290.
295 M. Escala, T. Zumbühl, C. Koller, R. Junge and R. Krebs, *Energy Fuels*, 2013, **27**, 454–460.
296 D. Kim, K. Yoshikawa and K. Park, *Energies*, 2015, **8**, 12412.
297 E. Steurer and G. Ardissone, *Energy Procedia*, 2015, **79**, 47–54.
298 X. Zhuang, H. Zhan, Y. Huang, Y. Song, X. Yin and C. Wu, *Bioresour. Technol.*, 2018, **267**, 17–29.
299 D. Basso, F. Patuzzi, D. Castello, M. Baratieri, E. C. Rada, E. Weiss-Hortala and L. Fiori, *Waste Manage.*, 2016, **47**, 114–121.
300 V. Benavente, E. Calabuig and A. Fullana, *J. Anal. Appl. Pyrolysis*, 2015, **113**, 89–98.
301 M. T. Reza, W. Yan, M. H. Uddin, J. G. Lynam, S. K. Hoekman, C. J. Coronella and V. R. Vásquez, *Bioresour. Technol.*, 2013, **139**, 161–169.
302 J. Chen, Z. Chen, C. Wang and X. Li, *Mater. Lett.*, 2012, **67**, 365–368.
303 S. K. Hoekman, A. Broch and C. Robbins, *Energy Fuels*, 2011, **25**, 1802–1810.
304 I. H. Hwang, H. Aoyama, T. Matsuto, T. Nakagishi and T. Matsuo, *Waste Manage.*, 2012, **32**, 410–416.
305 S. Kieseler, Y. Neubauer and N. Zobel, *Energy Fuels*, 2013, **27**, 908–918.
306 L. Garcia Alba, C. Torri, C. Samorì, J. Van Der Spek, D. Fabbri, S. R. A. Kersten and D. W. F. Brilman, *Energy Fuels*, 2012, **26**, 642–657.
307 S. M. Heilmann, H. T. Davis, L. R. Jader, P. A. Lefebvre, M. J. Sadowsky, F. J. Schendel, M. G. von Keitz and K. J. Valentas, *Biomass Bioenergy*, 2010, **34**, 875–882.
308 L. Li, Y. Wang, J. Xu, J. R. V. Flora, S. Hoque and N. D. Berge, *Bioresour. Technol.*, 2018, **262**, 284–293.
309 C. He, K. Wang, Y. Yang and J.-Y. Wang, *Energy Fuels*, 2014, **28**, 6140–6150.
310 C. Liu, J. Xu, J. Hu, H. Zhang and R. Xiao, *Chem. Eng. Technol.*, 2017, **40**, 1092–1100.
311 G. K. Parshetti, S. K. Hoekman and R. Balasubramanian, *Bioresour. Technol.*, 2013, **135**, 683–689.
312 A. M. Smith, S. Singh and A. B. Ross, *Fuel*, 2016, **169**, 135–145.
313 L. Gao, M. Volpe, M. Lucian, L. Fiori and J. L. Goldfarb, *Energy Convers. Manage.*, 2019, **181**, 93–104.
314 I. Van Zandvoort, E. R. H. Van Eck, P. De Peinder, H. J. Heeres, P. C. A. Bruijnincx and B. M. Weckhuysen, *ACS Sustainable Chem. Eng.*, 2015, **3**, 533–543.
315 I. Van Zandvoort, Y. Wang, C. B. Rasrendra, E. R. H. Van Eck, P. C. A. Bruijnincx, H. J. Heeres and B. M. Weckhuysen, *ChemSusChem*, 2013, **6**, 1745–1758.
316 M. Kleinert and T. Barth, *Energy Fuels*, 2008, **22**, 1371–1379.
317 A. Kloekhorst and H. J. Heeres, *ACS Sustainable Chem. Eng.*, 2015, **3**, 1905–1914.
318 A. L. Jongerius, R. Jastrzebski, P. C. A. Bruijnincx and B. M. Weckhuysen, *J. Catal.*, 2012, **285**, 315–323.
319 M. Trautmann, A. Löwe and Y. Traa, *Green Chem.*, 2014, **16**, 3710–3714.
320 M. Trautmann, S. Lang and Y. Traa, *Fuel*, 2015, **151**, 102–109.
321 Y. Wang, S. Agarwal, Z. Tang and H. J. Heeres, *RSC Adv.*, 2017, **7**, 5136–5147.
322 A. Effendi, H. Gerhauser and A. V. Bridgwater, *Renewable Sustainable Energy Rev.*, 2008, **12**, 2092–2116.
323 M. E. Boot-Handford, J. C. Abanades, E. J. Anthony, M. J. Blunt, S. Brandani, N. Mac Dowell, J. R. Fernández, M. C. Ferrari, R. Gross, J. P. Hallett, R. S. Haszeldine, P. Heptonstall, A. Lyngfelt, Z. Makuch, E. Mangano, R. T. J. Porter, M. Pourkashanian, G. T. Rochelle, N. Shah, J. G. Yao and P. S. Fennell, *Energy Environ. Sci.*, 2014, **7**, 130–189.
324 Y. Wang, S. Agarwal, A. Kloekhorst and H. J. Heeres, *ChemSusChem*, 2016, **9**, 951–961.
325 Z. Cheng, B. Saha and D. G. Vlachos, *ChemSusChem*, 2018, **11**, 3545.
326 C. B. Rasrendra, M. Windt, Y. Wang, S. Adisasmito, I. G. B. N. Makertihartha, E. R. H. Van Eck, D. Meier and H. J. Heeres, *J. Anal. Appl. Pyrolysis*, 2013, **104**, 299–307.
327 S. Agarwal, D. van Es and H. J. Heeres, *J. Anal. Appl. Pyrolysis*, 2017, **123**, 134–143.
328 T. M. C. Hoang, L. Lefferts and K. Seshan, *ChemSusChem*, 2013, **6**, 1651–1658.
329 T. M. C. Hoang, E. R. H. Van Eck, W. P. Bula, J. G. E. Gardeniers, L. Lefferts and K. Seshan, *Green Chem.*, 2015, **17**, 959–972.
330 M. Nagamori and T. Funazukuri, *J. Chem. Technol. Biotechnol.*, 2004, **79**, 229–233.
331 M. T. Reza, B. Wirth, U. Lüder and M. Werner, *Bioresour. Technol.*, 2014, **169**, 352–361.
332 K. Nakason, B. Panyapinyopol, V. Kanokkantapong, N. Viriya-empikul, W. Kraithong and P. Pavasant, *J. Energy Inst.*, 2017, 1–11.

333 K. Nakason, B. Panyapinyopol, V. Kanokkantapong, N. Viriya-empikul, W. Kraithong and P. Pavasant, *J. Energy Inst.*, 2018, **91**, 184–193.
334 K. Nakason, B. Panyapinyopol, V. Kanokkantapong, N. Viriya-empikul, W. Kraithong and P. Pavasant, *Biomass Convers. Biorefin.*, 2018, **8**, 199–210.
335 F. S. Asghari and H. Yoshida, *Ind. Eng. Chem. Res.*, 2006, **45**, 2163–2173.
336 S. K. R. Patil and C. R. F. Lund, *Energy Fuels*, 2011, **25**, 4745–4755.
337 R. Becker, U. Dorgerloh, E. Paulke, J. Mumme and I. Nehls, *Chem. Eng. Technol.*, 2014, **37**, 511–518.
338 M. T. Reza, E. Rottler, L. Herklotz and B. Wirth, *Bioresour. Technol.*, 2015, **182**, 336–344.
339 J. J. Pacheco and M. E. Davis, *Proc. Natl. Acad. Sci. U. S. A.*, 2014, **111**, 8363–8367.
340 Y. Román-Leshkov, C. J. Barrett, Z. Y. Liu and J. A. Dumesic, *Nature*, 2007, **447**, 982–985.
341 J. Jae, W. Zheng, R. F. Lobo and D. G. Vlachos, *ChemSusChem*, 2013, **6**, 1158–1162.
342 G. M. G. Maldonado, R. S. Assary, J. Dumesic and L. A. Curtiss, *Energy Environ. Sci.*, 2012, **5**, 6981–6989.
343 S. Krawielitzki and T. M. Kläusli, *Ind. Biotechnol.*, 2015, **11**, 6–8.
344 T. Werpy, G. Petersen, A. Aden, J. Bozell, J. Holladay, J. White, A. Manheim, D. Eliot, L. Lasure and S. Jones, *Top value added chemicals from biomass. Volume 1-Results of screening for potential candidates from sugars and synthesis gas*, 2004.
345 J. J. Bozell and G. R. Petersen, *Green Chem.*, 2010, **12**, 539–554.
346 Q. Fang and M. A. Hanna, *Bioresour. Technol.*, 2002, **81**, 187–192.
347 S. Suganuma, K. Nakajima, M. Kitano, D. Yamaguchi, H. Kato and S. Hayashi, *J. Am. Chem. Soc.*, 2008, **130**, 12787–12793.
348 D. J. Hayes, S. Fitzpatrick, M. H. B. Hayes and J. R. H. Ross, in *Biorefineries-Industrial Processes and Products: Status Quo and Future Directions*, ed. B. Kamm, P. R. Gruber and M. Kamm, Wiley, 2006, pp. 139–164.
349 A. S. Mamman, J. Lee, Y. Kim, I. T. Hwang, N. Park, Y. K. Hwang and J. Chang, *Biofuels, Bioprod. Biorefin.*, 2008, 438–454.
350 J. P. Lange, E. Van Der Heide, J. Van Buijtenen and R. Price, *ChemSusChem*, 2012, **5**, 150–166.
351 M. Dusselier, P. Van Wouwe, A. Dewaele, E. Makshina and B. F. Sels, *Energy Environ. Sci.*, 2013, **6**, 1415–1442.
352 F. Jin, Z. Zhou, A. Kishita and H. Enomoto, *J. Mater. Sci.*, 2006, **41**, 1495–1500.
353 S. K. Hoekman, A. Broch, C. Robbins, B. Zielinska and L. Felix, *Biomass Convers. Biorefin.*, 2013, **3**, 113–126.
354 B. Wirth and J. Mumme, *Appl. Bioenergy*, 2013, 1–10.
355 E. Erdogan, B. Atila, J. Mumme, M. T. Reza, A. Toptas, M. Elibol and J. Yanik, *Bioresour. Technol.*, 2015, **196**, 35–42.
356 X. Lu, J. R. V. Flora and N. D. Berge, *Bioresour. Technol.*, 2014, **154**, 229–239.
357 D. Steinbach, A. Kruse, J. Sauer and P. Vetter, *Energies*, 2018, **11**, 645.
358 S. Reiche, N. Kowalew and R. Schlögl, *ChemPhysChem*, 2014, **16**, 579–587.
359 P. Körner, S. Beil and A. Kruse, *React. Chem. Eng.*, 2019, **4**, 747–762.
360 H. Zhao, J. E. Holladay, H. Brown and Z. C. Zhang, *Science*, 2007, **316**, 1597 LP – 1600.
361 V. Choudhary, S. H. Mushrif, C. Ho, A. Anderko, V. Nikolakis, N. S. Marinkovic, A. I. Frenkel, S. I. Sandler and D. G. Vlachos, *J. Am. Chem. Soc.*, 2013, **135**, 3997–4006.
362 S. Hu, Z. Zhang, J. Song, Y. Zhou and B. Han, *Green Chem.*, 2009, **11**, 1746–1749.
363 Y. Jiang, L. Yang, C. M. Bohn, G. Li, D. Han, N. S. Mosier, J. T. Miller, H. I. Kenttämaa and M. M. Abu-Omar, *Org. Chem. Front.*, 2015, **2**, 1388–1396.
364 W. Weiqi and W. Shubin, *Chem. Eng. J.*, 2017, **307**, 389–398.
365 H. Lin, Q. Xiong, Y. Zhao, J. Chen and S. Wang, *AIChE J.*, 2016, **63**, 257–265.
366 X. Fu, J. Dai, X. Guo, J. Tang, L. Zhu and C. Hu, *Green Chem.*, 2017, **19**, 3334–3343.
367 L. Yang, J. Su, S. Carl, J. G. Lynam, X. Yang and H. Lin, *Appl. Catal., B*, 2015, **162**, 149–157.
368 Q. Hou, M. Zhen, L. Liu, Y. Chen, F. Huang, S. Zhang, W. Li and M. Ju, *Appl. Catal., B*, 2018, **224**, 183–193.
369 A. Dibenedetto, M. Aresta, L. Di Bitonto and C. Pastore, *ChemSusChem*, 2016, **9**, 118–125.
370 H. Li, S. Saravanamurugan, S. Yang and A. Riisager, *Green Chem.*, 2016, **18**, 726–734.
371 K. Dong, J. Zhang, W. Luo, L. Su and Z. Huang, *Chem. Eng. J.*, 2018, **334**, 1055–1064.
372 X. Qi, H. Guo, L. Li and R. L. Smith, *ChemSusChem*, 2012, **5**, 2215–2220.
373 J. Wang, L. Zhu, Y. Wang, H. Cui, Y. Y. Zhang and Y. Y. Zhang, *J. Chem. Technol. Biotechnol.*, 2017, **92**, 1454–1463.
374 J. Howard, D. W. Rackemann, J. P. Bartley, C. Samori and W. O. S. Doherty, *ACS Sustainable Chem. Eng.*, 2018, **6**, 4531–4538.
375 A. G. Demesa, A. Laari, E. Tirronen and I. Turunen, *Chem. Eng. Res. Des.*, 2015, **93**, 531–540.
376 Y. Román-Leshkov, J. N. Chheda and J. A. Dumesic, *Science*, 2006, **312**, 1933–1938.
377 T. Shimanouchi, Y. Kataoka, M. Yasukawa, T. Ono and Y. Kimura, *Solvent Extr. Res. Dev.*, 2013, **20**, 205–212.
378 J. M. R. Gallo, D. M. Alonso, M. A. Mellmer and J. A. Dumesic, *Green Chem.*, 2013, **15**, 85–90.

379 L. C. Blumenthal, C. M. Jens, J. Ulbrich, F. Schwering, V. Langrehr, T. Turek, U. Kunz, K. Leonhard and R. Palkovits, *ACS Sustainable Chem. Eng.*, 2016, **4**, 228–235.
380 E. Weingart, L. Teevs, R. Krieg and U. Prüße, *Energy Technol.*, 2018, **6**, 432–440.
381 E. C. Sindermann, A. Holbach, A. de Haan and N. Kockmann, *Chem. Eng. J.*, 2016, **283**, 251–259.
382 S. Mohammad, G. Grundl, R. Müller, W. Kunz, G. Sadowski and C. Held, *Fluid Phase Equilib.*, 2016, **428**, 102–111.
383 G. Grundl, M. Müller, D. Touraud and W. Kunz, *J. Mol. Liq.*, 2017, **236**, 368–375.
384 F. Liu, S. Sivoththaman and Z. Tan, *Sustainable Environ. Res.*, 2014, **24**, 149–157.
385 H. Wang, S. Liu, Y. Zhao, H. Zhang and J. Wang, *ACS Sustainable Chem. Eng.*, 2016, **4**, 6712–6721.
386 J. Zhou, T. Huang, Y. Zhao, Z. Xia, Z. Xu, S. Jia, J. Wang and Z. C. Zhang, *Ind. Eng. Chem. Res.*, 2015, **54**, 7977–7983.
387 X. Sun, Z. Liu, Z. Xue, Y. Zhang and T. Mu, *Green Chem.*, 2015, **17**, 2719–2722.
388 T. Brouwer, M. Blahusiak, K. Babic and B. Schuur, *Sep. Purif. Technol.*, 2017, **185**, 186–195.
389 J. Briscoe, A. Marinovic, M. Sevilla, S. Dunn and M. Titirici, *Angew. Chem., Int. Ed.*, 2015, **54**, 4463–4468.
390 R. Wang, K. Q. Lu, Z. R. Tang and Y. J. Xu, *J. Mater. Chem. A*, 2017, **5**, 3717–3734.
391 G. A. M. Hutton, B. C. M. Martindale and E. Reisner, *Chem. Soc. Rev.*, 2017, **46**, 6111–6123.
392 X. Sun and Y. Li, *Angew. Chem., Int. Ed.*, 2004, **43**, 597–601.
393 X. Jia, J. Li and E. Wang, *Nanoscale*, 2012, **4**, 5572–5575.
394 Z. Song, F. Quan, Y. Xu, M. Liu, L. Cui and J. Liu, *Carbon*, 2016, **104**, 169–178.
395 M. L. Liu, B. Bin Chen, C. M. Li and C. Z. Huang, *Green Chem.*, 2019, **21**, 449–471.
396 B. De and N. Karak, *RSC Adv.*, 2013, **3**, 8286–8290.
397 J. Shen, S. Shang, X. Chen, D. Wang and Y. Cai, *Mater. Sci. Eng., C*, 2017, **76**, 856–864.
398 D. Qu, M. Zheng, L. Zhang, H. Zhao, Z. Xie, X. Jing, R. E. Haddad, H. Fan and Z. Sun, *Sci. Rep.*, 2015, **4**, 5294.
399 J. Liu, S. Lu, Q. Tang, K. Zhang, W. Yu, H. Sun and B. Yang, *Nanoscale*, 2017, **9**, 7135–7142.
400 R. Atchudan, T. N. J. I. Edison, D. Chakradhar, S. Perumal, J. J. Shim and Y. R. Lee, *Sens. Actuators, B*, 2017, **246**, 497–509.
401 N. Papaioannou, A. Marinovic, N. Yoshizawa, A. E. Goode, M. Fay, A. Khlobystov, M. Titirici and A. Sapelkin, *Sci. Rep.*, 2018, **8**, 6559.
402 H. Luo, N. Papaioannou, E. Salvadori, M. M. Roessler, G. Ploenes, E. R. H. van Eck, L. C. Tanase, J. Feng, Y. Sun, Y. Yang, M. Danaie, A. Belen Jorge, A. Sapelkin, J. Durrant, S. D. Dimitrov and M. M. Titirici, *ChemSusChem*, 2019, **12**, 4432–4441.
403 H. Shengliang, T. Fei, B. Peikang, C. Shirui, S. Jing and Y. Jing, *Mater. Sci. Eng., B*, 2009, **157**(1–3), 11–14.
404 R. Tian, S. Zhong, J. Wu, Y. Geng, B. Zhou, Q. Wang and W. Jiang, *J. Mater. Chem. C*, 2017, **5**, 9174–9180.
405 F. Ehrat, S. Bhattacharyya, J. Schneider, A. Löf, R. Wyrwich, A. L. Rogach, J. K. Stolarczyk, A. S. Urban and J. Feldmann, *Nano Lett.*, 2017, **17**, 7710–7716.
406 B. Dai, C. Wu, Y. Lu, D. Deng and S. Xu, *J. Lumin.*, 2017, **190**, 108–114.
407 J. Yang, W. Chen, X. Liu, Y. Zhang and Y. Bai, *Mater. Res. Bull.*, 2017, **89**, 26–32.
408 Z. Tian, X. Zhang, D. Li, D. Zhou, P. Jing, D. Shen, S. Qu, R. Zboril and A. L. Rogach, *Adv. Opt. Mater.*, 2017, **5**, 1700416.
409 T. Zhang, J. Zhu, Y. Zhai, H. Wang, X. Bai, B. Dong, H. Wang and H. Song, *Nanoscale*, 2017, **9**, 13042–13051.
410 S. K. Bhunia, A. Saha, A. R. Maity, S. C. Ray and N. R. Jana, *Sci. Rep.*, 2013, **3**, 1473.
411 R. Purbia and S. Paria, *Biosens. Bioelectron.*, 2016, **79**, 467–475.
412 P. Yang, J. Zhao, L. Zhang, L. Li and Z. Zhu, *Chem. – Eur. J.*, 2015, **21**, 8561–8568.
413 Q. Xu, Y. Liu, C. Gao, J. Wei, H. Zhou, Y. Chen, C. Dong, T. S. Sreeprasad, N. Li and Z. Xia, *J. Mater. Chem. C*, 2015, **3**, 9885–9893.
414 D.-W. Zhang, N. Papaioannou, N. M. David, H. Luo, H. Gao, L. C. Tanase, T. Degousée, P. Samorì, A. Sapelkin, O. Fenwick, M.-M. Titirici and S. Krause, *Mater. Horiz.*, 2018, **5**, 423–428.
415 A. Marinovic, L. S. Kiat, S. Dunn, M. M. Titirici and J. Briscoe, *ChemSusChem*, 2017, **10**, 1004–1013.